

NSF Grant ATM-9912051
National Science Foundation

KINEMATIC AND MICROPHYSICAL EVOLUTION
OF THE 29 JUNE SUPERCELL OBSERVED DURING
STEPS

by Sarah A. Tessendorf and Steven A. Rutledge

Colorado
State
University

DEPARTMENT OF
ATMOSPHERIC SCIENCE

PAPER NO. 738

**KINEMATIC AND MICROPHYSICAL EVOLUTION OF THE 29 JUNE
SUPERCELL OBSERVED DURING STEPS**

by

Sarah A. Tessendorf

and

Steven A. Rutledge

Department of Atmospheric Science

Colorado State University

Fort Collins, CO 80523

**Research Supported by
National Science Foundation**
under Grant ATM-9912051

Spring 2003

Atmospheric Science Paper No. 738

COLORADO STATE UNIVERSITY

November 21, 2002

WE HEREBY RECOMMEND THAT THE THESIS PREPARED UNDER OUR SUPERVISION BY SARAH A. TESSENDORF ENTITLED KINEMATIC AND MICROPHYSICAL EVOLUTION OF THE 29 JUNE SUPERCELL OBSERVED DURING STEPS BE ACCEPTED AS FULFILLING IN PART REQUIREMENTS FOR THE DEGREE OF MASTER OF SCIENCE.

Committee on Graduate Work

William R. Cotton

Kristina D. Reiter

SA A. RA

Advisor

SA A. RA

Department Head

ABSTRACT

KINEMATIC AND MICROPHYSICAL EVOLUTION OF THE 29 JUNE SUPERCELL OBSERVED DURING STEPS

The focus of this thesis is to examine the kinematic and microphysical properties of a severe storm using polarimetric and Doppler radar data. The data were collected during the Severe Thunderstorm Electrification and Precipitation Study (STEPS) that took place between 17 May 2000 and 20 July 2000 in eastern Colorado and western Kansas. One goal of STEPS is to find a relationship between the microphysics and kinematics of severe storms on the High Plains and their unusual positive cloud-to-ground lightning production. The severe storm observed on 29 June 2000 produced large hail, frequent positive cloud-to-ground lightning, an F1 tornado, and displayed characteristic storm splitting evolution during the sampling period. Unprecedented measurements from three Doppler radars were used to describe the kinematics and microphysics of this storm. Radial components of the wind fields relative to the three Doppler radars were combined to produce the three-dimensional winds in the storm. Bulk precipitation types (e.g. rain, hail) were objectively determined using the multi-parameter variables available on two of the radars.

The Doppler-derived kinematic fields were compared with the microphysical classifications over a nearly three-hour period to examine trends during the lifecycle of the supercell. Results showed that the supercell intensified rapidly while storm splitting

occurred. Prior to splitting, there was little cloud-to-ground lightning and little evidence of hail aloft. After storm splitting, hail volume and cloud-to-ground lightning activity quickly intensified. The updraft of this storm pulsated, with maximum speeds to nearly 50 m s^{-1} . The peaks in hail production aloft, largely around -10° C , were well correlated with the updraft fluctuations as well as with peaks in the frequency of positive cloud-to-ground lightning flashes. These results are consistent with experimental work that shows positive charging in ice-ice collisions around -10° C . The dynamics of the storm-splitting process, in terms of radar-derived updraft and vorticity fields, were shown to be consistent with current conceptual models. The results of this thesis advance our knowledge of supercell evolution and will be used to help determine the electrification mechanisms of severe storms that produce predominantly positive cloud-to-ground lightning.

Sarah A. Tessendorf
Atmospheric Science Department
Colorado State University
Fort Collins, CO 80523
Spring 2003

ACKNOWLEDGEMENTS

I am grateful for the suggestions that committee members, Drs. William Cotton and Kristina Rinker, offered to this work. I want to extend my deepest appreciation to Jay Miller for his exceptional mentorship and support for this project. The Significant Opportunities in Atmospheric Research and Science (SOARS) program and staff deserve substantial credit for giving me the opportunity to conduct portions of this research at the National Center for Atmospheric Research (NCAR) facilities and with NCAR scientists, in addition to the support and encouragement they have given me for the past four years. I want to thank the CSU Radar Meteorology group, particularly Dr. Rob Cifelli, Margi Cech, Paul Hein, Andrea Williams, and Gustavo Pereira for their support and insights for this work. Kyle Wiens also has been an integral part of this research, as a collaborator on this case study and for creating the software used to generate many of the figures for this project. Enlightening discussions with Drs. Larry Carey, Walt Peterson, Charles Knight, and Morris Weisman were also invaluable to the progress of this research. This research was financially supported by SOARS, an American Meteorological Society Graduate Fellowship, and NSF grant number ATM-9912051.

TABLE OF CONTENTS

1	INTRODUCTION	1
2	BACKGROUND	7
2.1	Radar as an Observational Tool for Studying Severe Storms	7
2.2	A Review of Supercell Storms	8
2.3	Hypotheses for Positive Cloud-to-ground Lightning Production	13
3	DATA AND METHODS	24
3.1	Radar Variables	24
3.2	Polarimetric Variables	25
3.3	Multiple-Doppler Radar Analysis	28
3.4	Polarimetric Radar Analysis	29
4	ENVIRONMENTAL CONDITIONS	33
4.1	Synoptic Environment	33
4.2	Thermodynamic Structure	33
4.3	Surface Conditions	34
5	AIRFLOW AND MICROPHYSICAL STRUCTURE	40
5.1	Storm Overview	40
5.2	Time Series Analysis	41
5.2.1	Period A	42
5.2.2	Period B	43
5.2.3	Period C	44
5.2.4	Period D	44
5.2.5	Period E	46
5.2.6	Period F	47
5.2.7	Period G	47
5.2.8	Summary of findings	47

5.3	Detailed Analysis of Selected Intensification Periods	49
5.3.1	Period B	49
5.3.2	Period D	50
5.3.3	Period F	53
5.3.4	Period G	54
6	SUMMARY AND DISCUSSION	88
	APPENDIX	93
	REFERENCES	95

LIST OF TABLES

Table 1. Characteristics of the radars used in this study	4
Table 2. Hydrometeor classification criteria	32

LIST OF FIGURES

Figure 1. The triple-Doppler radar network (and associated dual/triple-Doppler lobes) for the STEPS field campaign	5
Figure 2. Illustration of a horizontally and vertically polarized electromagnetic wave	6
Figure 3. Schematic of a severe storm that travels to the right of the winds from Browning (1964)	16
Figure 4. Schematic of how a vortex tube (in a westerly environmental shear regime) interacts with a convective storm (from Klemp, 1987)	17
Figure 5. Schematic of hail trajectories in a supercell based on the model of Browning and Foote (1976)	18
Figure 6. Schematic of updraft evolution as depicted by Foote and Frank (1983)	19
Figure 7. Schematic diagram illustrating that the polarity of cloud-to-ground lightning as a function of location with respect to a surface equivalent potential temperature maximum (from Smith et al., 2000)	20
Figure 8. A schematic illustrating the charge structure of an ordinary thunderstorm (MacGorman and Rust, 1998)	21
Figure 9. Schematic of hypotheses for positive cloud-to-ground lightning production in severe storms (Williams, 2001)	22
Figure 10. Electrification of rime from Takahashi (1978)	23
Figure 11. Illustration of precipitation particle and associated differential reflectivity (Houze, 1993)	31
Figure 12. 250 mb RUC-2 wind analysis for 2100 UTC on 29 June 2000	36
Figure 13. 850 mb RUC-2 analysis for 2100 UTC on 29 June 2000	37
Figure 14. MGLASS soundings on 29 June 2000: (a) 2022 UTC at Goodland, Kansas and (b) 2338 UTC in northeastern Colorado near Sterling.	39
Figure 15. 2215 UTC base reflectivity from KGLD (0,0) indicating a surface boundary (thin line radar echo) behind (northwest) Storm I. Storm II is an earlier storm (see Section 5.1)	56
Figure 16. Time series of total flash rate (IC + CG) and total CG activity (top panel) and total CG activity with only positive CG activity overlaid (bottom panel)	57
Figure 17. Swath of base reflectivities from KGLD (0,0) for the period 2100-0251 UTC with NLDN lightning overlaid	58
Figure 18. 0004 UTC base reflectivities from KGLD (0,0) indicating a thin line echo is present	59
Figure 19. Updraft volume time series	60
Figure 20. Precipitation echo volumes below the melting level	61
Figure 21. Maximum updraft time series	62

Figure 22. Time-height cross section of the maximum updraft contoured at 10 m s ⁻¹ intervals	63
Figure 23. Graupel echo volume above the melting level at each time and height	64
Figure 24. 2239 UTC 8 km synthesis with storm relative streamlines overlaid on S-Pol reflectivity	65
Figure 25. Maximum vorticity (10 ⁻³ s ⁻¹) at each time and height	66
Figure 26. Hail echo volume above the melting level at each time and height	67
Figure 27. 2343 UTC 6 km synthesis with storm relative streamlines overlaid on S-Pol reflectivity	68
Figure 28. 0023 UTC 6 km synthesis with storm relative streamlines overlaid on S-Pol reflectivity	69
Figure 29. 0043 UTC 6 km synthesis with storm relative streamlines overlaid on S-Pol reflectivity	70
Figure 30. A height profile of cloud liquid water content from the MGLASS sounding at 2022 UTC at Goodland, Kansas	71
Figure 31. 2239 UTC synthesis at 7 km showing (a) S-Pol reflectivity, (b) vertical vorticity, (c) Hydrometeor type, and (d) vertical velocity	72
Figure 32. Same as Figure 31 except for 2246 UTC	73
Figure 33. Same as Figure 31 except for 2325 UTC	74
Figure 34. Same as Figure 31 except for 2331 UTC	75
Figure 35. 2331 UTC synthesis at 5.5 km showing (a) S-Pol reflectivity, (b) vertical vorticity, and a vertical cross section at y = 26.0 km with ground-relative wind vectors are overlaid in black in (c)	76
Figure 36. Vertical profile of the mean tilting (red) and stretching (green) terms of the local vorticity tendency (black) at 2331 UTC for the (x,y) domain illustrated in Figure 35 (a) and (b)	77
Figure 37. Same as Figure 31 except for 2338 UTC	78
Figure 38. Same as Figure 31 except for 2343 UTC	79
Figure 39. Same as Figure 35 except for 2343 UTC and the vertical cross section is x = 21.5 km	80
Figure 40. Vertical profile of the mean tilting (red) and stretching (green) terms of the local vorticity tendency (black) at 2343 UTC for the (x,y) domain illustrated in Figure 39 (a) and (b)	81
Figure 41. Same as Figure 31 except for 2351 UTC	82
Figure 42. Same as Figure 31 except for 0023 UTC	83
Figure 43. Same as Figure 31 except for 0030 UTC	84
Figure 44. Same as Figure 31 except for 0036 UTC	85
Figure 45. Same as Figure 31 except for 0043 UTC	86
Figure 46. Same as Figure 31 except for 0049 UTC	87

Chapter 1

INTRODUCTION

Summer convective storms can become severe and produce heavy rain, lightning, strong winds, hail, and occasionally tornadoes. These phenomena can be devastating to the public by inflicting loss of life and property damage. Though significant improvements have been made since the modernization of the National Weather Service (NWS), especially with the addition of the WSR-88D radars and more sophisticated numerical models, forecast uncertainties remain. To develop improved forecasting capabilities there must be advancements in our scientific understanding of these storms, hence the Severe Thunderstorm Electrification and Precipitation Study (STEPS) was established. The general goal of STEPS-related research is "to achieve a better understanding of the interactions between kinematics, precipitation production, and electrification in severe thunderstorms on the High Plains" (Weisman and Miller, 2000). The study also aimed to identify relationships between microphysical and dynamical processes in severe storms on the High Plains and why some storms produce predominantly positive cloud-to-ground lightning.

The STEPS campaign took place from 17 May 2000 to 20 July 2000 near Goodland, KS. This region was chosen because of its high frequency for severe storms that produced predominantly (>50%) positive cloud-to-ground lightning (PPCG; Carey et al., 2002a) and low-precipitation (LP) supercells (Carey et al., 2002a). To date, these

storms have not been well documented in the literature. PPCG-producing storms are unusual in the sense that they produce copious amounts of positive CG lightning, which lower positive charge to ground. More typical thunderstorms produce the bulk of their lightning in the form of negative CGs, with less than 10% of the ground flashes being positive (Orville and Huffines, 2001). Instrumentation and observing systems operated during STEPS included: three S-Band Doppler radars (two of which were multi-parameter research radars) for mapping the three-dimensional structure of precipitation and storm winds; a mobile mesonet for determining surface and sub-cloud conditions beneath the storms; balloon-borne in situ electric field mills to measure in-storm parameters including temperature, pressure, wind, and electric field (operated by NSSL, Rust and MacGorman, 2002); armored aircraft storm penetrations by the SDSMT T-28 for in situ wind, hydrometeor, and electric field observations (<http://www.ias.sdsmt.edu/institute/t28/index.htm>); a mobile sounding unit for environmental wind and thermodynamic profiles near the storm; the National Lightning Detection Network (NLDN) to display the cloud-to-ground lightning strike location and polarity in "real time" (Cummins et al., 1998); and a lightning mapping array to provide a detailed map of all lightning activity (Rison et al., 1999).

The CSU-CHILL polarimetric Doppler radar, the National Center for Atmospheric Research (NCAR) S-Pol polarimetric Doppler radar, and the Goodland, Kansas National Weather Service (NWS) WSR-88D radar comprised the triple-Doppler radar network used to take the radar measurements (Table 1). The three radars were arranged in a rough equilateral triangle with approximately 60-km sides providing radar coverage of eastern Colorado, northwestern Kansas, and southwestern Nebraska (Figure

1). All three radars are S-band Doppler radars; however, the CSU-CHILL and NCAR S-Pol radars are dual linearly polarized, and thus can transmit and receive horizontally and vertically polarized electromagnetic waves (Figure 2). This capability enables the radar to detect hydrometeor shape and size that, when combined with air temperature, can be used to infer hydrometeor types within storms (Herzogh and Jameson, 1992; Conway and Zrnich, 1993; Carey and Rutledge, 1996; Carey and Rutledge, 1998).

On 29 June 2000, a PPCG-producing severe thunderstorm propagated through the STEPS multiple-Doppler radar network between 2130 UTC (29 June) and 0115 UTC (30 June) near Bird City, KS. It produced large hail and an F1 tornado, in addition to copious lightning. In addition, the storm became a right mover at 2328 UTC, coincident with the onset of vigorous PPCG lightning and the touchdown of the tornado. It is important to understand the processes that induced the right turn, large hail production, and PPCG lightning in this storm, and how the kinematics and microphysics relate to those behaviors to improve forecasting and modeling capabilities. This study uses STEPS data to investigate the possible relationships between the kinematics and microphysics that characterize the 29 June 2000 storm.

Table 1. Characteristics of the radars used in this study

Radar Characteristic	CSU-CHILL	NCAR S-Pol	KGLD WSR-88D
Wavelength (cm)	11.01	10.71	10.0
Polarization	Linear, H & V	Linear, H & V	Linear, H
Peak Power (kW)	800-1000	>1000	475
Beamwidth (deg)	1.1	0.91	1.0

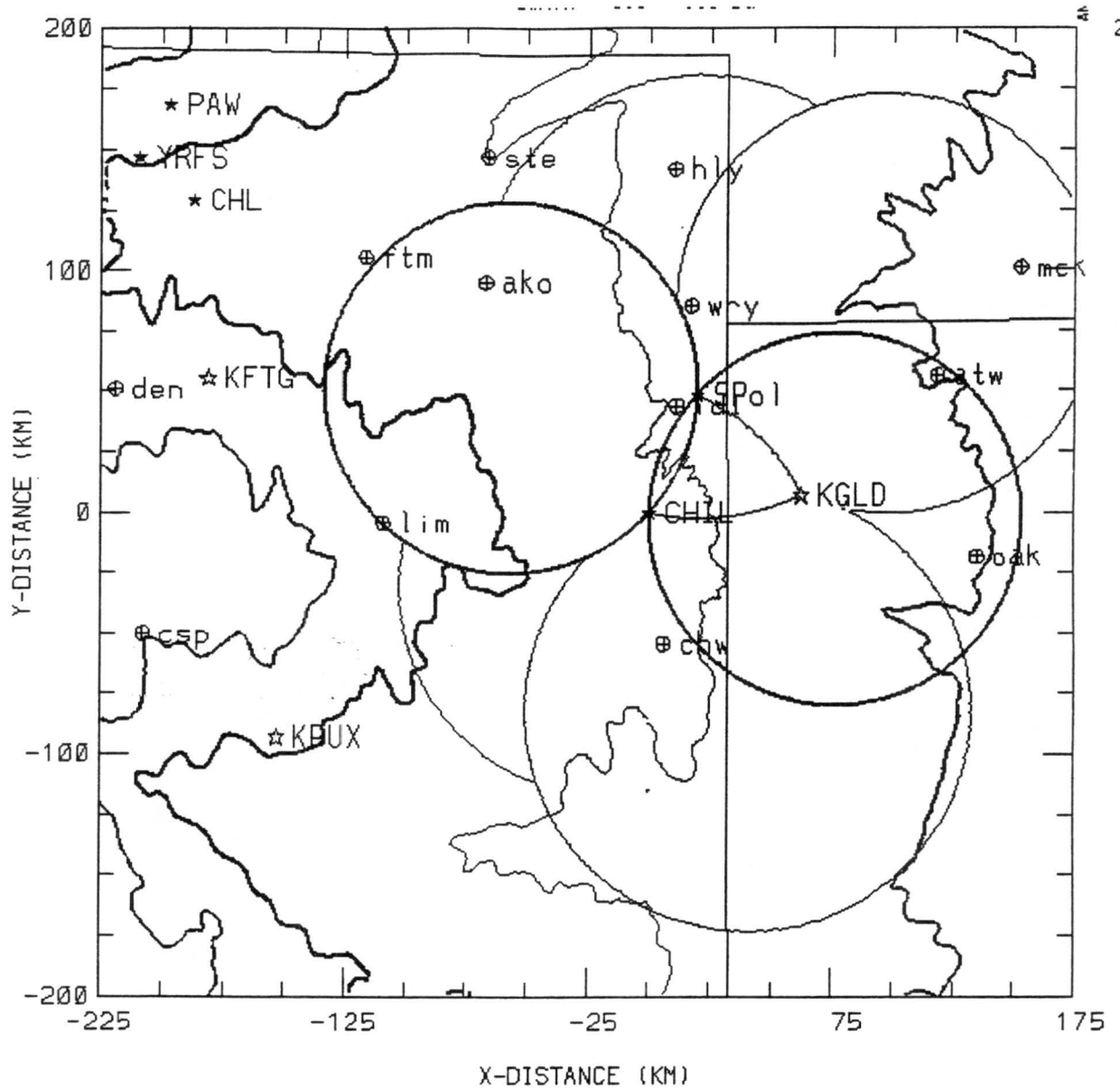


Figure 1. The triple-Doppler radar network (and associated dual/triple-Doppler lobes) for the STEPS field campaign (STEPS Scientific Overview). East-west and north-south straight lines are CO-KS, CO-NE, and NE-KS state borders in this and Figures 3-4 and 6-9. All distances are east-west (x) and north-south (y) from Goodland, Kansas in this and subsequent figures. Contours are 3, 4, 5, and 6 kft topography levels. (courtesy L. J. Miller)

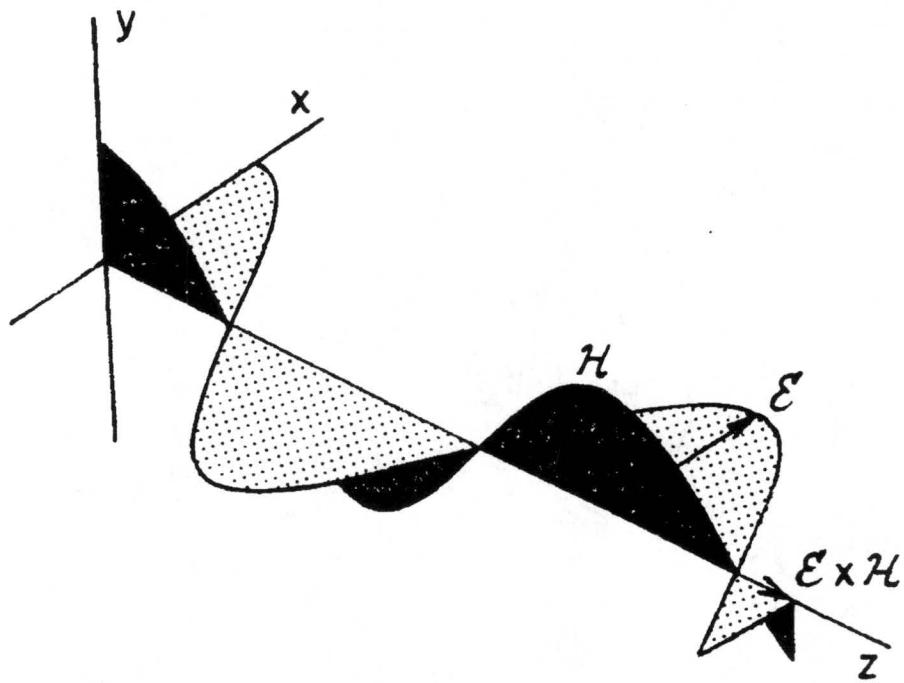


Figure 2. Illustration of a horizontally and vertically polarized electromagnetic wave.

Chapter 2

BACKGROUND

2.1 Radar as an Observational Tool for Studying Severe Storms

The use of radar in a meteorological context originated during World War II, as rain was found to obscure targets, which at the time were typically warships and aircraft (Burgess and Ray, 1986). In present day, radars operate at various wavelengths to remotely detect precipitation, clouds, and even turbulent air motions in the planetary boundary layer (Houze, 1993). Additional features available on some radars, such as Doppler velocity retrieval and dual-polarization capabilities, enable us to detect radial winds and particle types within storms.

Radial velocities from multiple Doppler radars can be combined to infer three-dimensional winds within storms. Many studies have utilized multiple-Doppler wind analysis to determine the kinematic structure of storms, including estimating storm airflow, updraft velocities, vorticity, and divergence fields (e.g. Ray, 1976; Ray et al., 1975, 1978, 1980; Nelson, 1983; Foote, 1984; Nelson and Knight, 1987; Miller et al., 1988, 1990; Bluestein and Woodall, 1990). Many of these studies were then able to relate the kinematic structure of the storm to other phenomena such as precipitation production and tornadogenesis. This study will utilize multiple Doppler radial velocity measurements to calculate the three-dimensional wind field, which will then be used to infer updraft strength and updraft volumes and perform vorticity analyses.

Polarimetric measurements have been used to infer bulk hydrometeor types for convective storms (Herzogh and Jameson, 1992; Conway and Zrnica, 1993; Carey and Rutledge, 1996; Carey and Rutledge, 1998). Polarimetric data have also been used to detect hail and discriminate its size (Bringi et al., 1986; Zrnica et al., 1993a), estimate rain rates (Sachidananda and Zrnica, 1987; Aydin and Giridhar, 1992; Gorgucci et al., 1994; Aydin et al., 1995), identify regions containing mixed phase hydrometeors and discriminate between ice particle types (Zrnica et al., 1993a). Dye and Martner (1978) emphasized that for northeastern Colorado thunderstorms the reflectivity factor alone could not discriminate hail, thus reinforcing the useful implications of polarimetric observations. In this study, polarimetric data will be used to objectively discriminate hydrometeor types using lookup table thresholds of polarimetric variables along with temperature.

2.2 A Review of Supercell Storms

Supercells have been the focus of much research due to their association with severe weather. They have commonly been defined as strong convective storms that are long-lived and contain a temporally and spatially (in the vertical) persistent mesocyclone (Moller et al., 1994). Specific characteristics about the structure and airflow within supercells have been revealed by detailed field studies. Due to the inherent variability of the weather, however, these characteristics may apply to many, but not all, supercells. Regardless, it is still important to understand the generalized structure of supercells for comparison with the current observations.

Characteristics that are typically recognized as supercellular have been the development of a bounded weak echo region (BWER), forward- and rear-flank

downdrafts, and a low-level reflectivity hook echo. The BWER, or vault-like structure, has been associated with a strong and persistent updraft which does not allow hydrometeors enough time to grow from vapor condensation on cloud condensation nuclei (CCN) just above cloud base to significant drop sizes, hence the low reflectivity values in this region (Browning and Donaldson, 1963; Browning, 1964, 1965). The forward-flank downdraft is normally located in the forward and right flanks of the storm and produces a weak surface discontinuity (Lemon and Doswell, 1979). A rear-flank downdraft (RFD) is located on the upwind side of the storm and is typically drier, more dense and cooler than the forward-flank downdraft (Lemon and Doswell, 1979). Convergence between the low-level environmental airflow and the strong outflow from the RFD lifts low-level moist air to help sustain the updraft. The hook echo, which partially surrounds the BWER and is usually detected at low levels, has been used to indicate the likely presence of a mesocyclone and is often associated with tornadoes (Browning, 1964).

Supercells have also been documented to travel in a direction to the right of the mean winds. An early conceptual model (see Figure 3) of this behavior was presented by Browning (1964). More recently, numerical simulations of supercells have been performed to study the mechanisms of storm splitting and test the dependence of the environmental wind shear on storm motion (Wilhelmson and Klemp, 1978; Klemp and Wilhelmson, 1978; Rotunno, 1981; Klemp et al., 1981; Rotunno and Klemp, 1985). These studies found that storm splitting occurred when the precipitation-induced downdraft split the low-level updraft into two components: one with cyclonic rotation that moved to the right of the mean winds, and the other anticyclonic that moved to the

left (Figure 4). Unidirectional wind shear environments were observed to produce splitting storms that favored the persistence of both the right and left-moving cells. Right-moving (left-moving) storms were most prevalent in environments with a clockwise (counterclockwise) turning hodograph, however based on climatology, clockwise turning hodographs are more common, and thus right-moving storms have been observed more often. While it has frequently been simulated in models, splitting storms have rarely been observed by Doppler radar. The limited number of studies that have documented storm-splitting processes with Doppler radar observations (Brown et al., 1973; Bluestein and Sohl, 1979; Rotunno, 1981; Kubesh et al., 1988; Bluestein and Woodall, 1990; Brown, 1992) concluded that the updraft in the right-moving storms typically rotated cyclonically while it rotated anticyclonically in the left-moving storms. Rotunno (1981) compared the vorticity and vertical velocity patterns in thunderstorms between numerical simulations and observations. A vortex pair was simulated to split into two vortex pairs, one moving to the right of the mean wind and the other to the left. This behavior, for the most part, was supported by the observations presented therein. Brown and Meitin (1994) studied two splitting storms that, unlike most splitting storms observed prior to their observations, had more dominant left-moving members and the updrafts were not observed to rotate (or be co-located with vertical vorticity). They did, however, detect a vortex pair (of cyclonic and anticyclonic rotation) in vertical vorticity with centers on the left and right sides of the updraft, typically between 6 to 8 km.

Supercells also tend to be responsible for much of the large hail in the High Plains (Browning, 1977). Browning and Foote (1976, hereafter BF76) outlined a three-stage process for hail production in supercells (Figure 5). In the first stage, small particles (or

embryos) grow during their initial ascent near the right flank of the main updraft. Secondly, some of these embryos circulate around the forward flank of the main updraft as they descend. This forms what is referred to as the “embryo curtain” around the circulating updraft. Lastly, particles from the embryo curtain re-enter the main updraft and grow into large hailstones in a single up-and-down path. Nelson (1983) further stated that a recycling process similar to that of the BF76 model must be occurring, yet the embryos’ origination area must be more extensive than the small area outlined in BF76 for some storms. To serve as effective embryos for hail growth, several studies observed that particles entering the updraft must already be as large as 100 micron to 1 mm, thus implying that a recycling process is taking place (Dye et al., 1983; Miller et al., 1983, 1988, 1990). Additionally, Miller et al. (1988, 1990) found that shedding from hailstones during wet growth or while melting was an important source of embryos for recycling. However, some studies conclude that if a single strong updraft is present in a highly sheared environment, the recycling process may be inhibited, therefore yielding less precipitation (Marwitz, 1972a, 1972b). Further studies identified a “hybrid” multicellular-supercellular storm as a proficient hail-producing storm archetype for the Central Plains (Nelson and Knight, 1987; Nelson, 1987). The “hybrid” storm exhibited large BWERs and appeared generally steady as a supercell would, but multiple updrafts were observed at any time separated by a distance of 5 to 8 km. The “hybrid” storm’s updraft structure was similar to what Foote and Frank (1983) described as “weak” evolution (Figure 6).

In addition to the aforementioned features of supercells, these storms tend to produce large amounts of lightning. Maximum total flash rates for severe storms

(intracloud and cloud-to-ground flashes combined) vary greatly but have been observed on the order of 10^2 flashes per minute, whereas a nonsevere storm typically averages 1-3 flashes per minute (Williams, 2001). The relationship between intracloud (IC) and CG flashes, also known as the IC/CG ratio, tends to increase with increased storm severity and electrical activity (Williams, 2001). Lang et al. (2000) observed severe convective storms that produced high IC flash rates, while the (negative) CG flash rates were particularly low (< 1 per minute).

Supercells also occasionally produce unusually large amounts of positive cloud-to-ground (CG) lightning during portions of their lifetimes. Why some storms produce PPCG lightning as opposed to the more commonly observed supercells that produce predominantly negative CG lightning is not understood. Some hypothesize that the difference lies in the kinematic structure and microphysical properties of the storm or storm intensity (Rust et al., 1985; Branick and Doswell, 1992; MacGorman and Burgess, 1994). In particular, Stolzenburg (1994) suggested that large amounts of positive CG lightning may be due to rapid increases in radar echo top height and was coincident with the production of large hail. Carey and Rutledge (1996) noted that CG activity tended to lag behind the peak in IC activity and was associated with the descent of graupel and/or small hail. Lang et al. (2000) noticed that radar reflectivity intensity and hail production were anticorrelated with *negative* CG lightning and Carey and Rutledge (1998) found that large hail and *positive* CG lightning appeared to be anticorrelated, with broad peaks in the positive CGs lagging behind the peaks in large hail falling out of the storm. However, Carey and Rutledge (1998) did state that there was a direct correlation between the initial increase in the IC/CG ratio, the first positive CG, and the early production of hail aloft.

Recent work by Smith et al. (2000) revealed an intriguing relationship between surface equivalent potential temperature (θ_e) and the polarity of CG lightning. Their study indicates that storms dominated by negative CG flashes formed in regions of weak θ_e gradients and downstream of a θ_e ridge axis (track C in Figure 7). On the other hand, storms that formed in regions with a strong θ_e gradient or upstream of a θ_e maximum were usually dominated by positive CG lightning. They also noted that when storms crossed the θ_e ridge axis the polarity switched from positive to negative, while those that remained upstream from the θ_e maximum continued to produce positive CG lightning throughout their lifetimes (tracks A and B in Figure 7). These results, if proved consistent for a larger sample of storms, are promising for predicting the lightning polarity of storms, however, to fully understand the mechanisms that determine the polarity of lightning in supercells, further research is needed.

2.3 Hypotheses for Positive Cloud-to-ground Lightning Production

In the previous section, the tendency for supercells to produce anomalous positive cloud-to-ground lightning was introduced. Recent studies have begun to address this issue and four primary hypotheses outlining the charge structure in the storm that could be contributing to the positive CGs have resulted. The majority of this discussion is adapted from the review of severe storm electrification by Williams (2001).

Before discussing the hypotheses for positive CG production, a bit of background on ordinary thunderstorm charge structure is in order. It is generally understood that an ordinary (or nonsevere) thunderstorm has a dipole moment due to the charge separation from collisions between graupel and ice particles. These collisions tend to transfer

negative charge to the larger (graupel) particles, which, due to gravity, fall faster than the positively charged ice particles. This results in a negative charge layer in the lower part of the storm and a positive charge layer aloft (Figure 8). A small region of positive charge is sometimes detected below the main negative charge region (Simpson and Scrase, 1937; Marshall and Winn, 1982; Marshall and Rust, 1991; MacGorman and Rust, 1998).

The first hypothesis is typically referred to as the *tilted dipole* hypothesis (Figure 9a). In this situation, the upper positive charge region has been displaced laterally from that in Figure 8 by a tilted updraft and strong upper level winds. Positive CG strokes would then result from the transfer of positive charge over the distance from the upper positive charge layer to the ground. This hypothesis does not explain the lack of negative CG flashes observed at the time of predominantly positive CG activity, however, since the lower negative charge layer has not been altered from the traditional thunderstorm model.

A second hypothesis attempts to account for the reduction of negative CG flashes in predominantly positive storms. It has been referred to as the *precipitation unshielding* hypothesis (Figure 9b). This hypothesis suggests that precipitation carries the negative charge out of the storm as it falls and “unshields” the upper positive charge layer (Carey and Rutledge, 1998). The upper positive charge layer would then be more capable of producing a ground stroke.

The *inverted dipole* hypothesis proposes that the polarity of the traditional thunderstorm dipole (depicted in Figure 8) is reversed (Figure 9c) yielding a positive charge layer closer to the ground to initiate positive CG strokes (Seimon, 1993). The

weakness of this hypothesis is that field changes in the intracloud lightning would have the opposite polarity than that of the traditional charge layer model, and this has not been observed (Williams, 2001).

The fourth hypothesis, generally called the *tripole* hypothesis, assumes that the lower positive charge found in an ordinary thunderstorm (Figure 8) is enhanced and can then dominate over the elevated negative charge region in the production of ground flashes (Figure 9d). This hypothesis is typically associated with the inverted dipole process because an enhanced lower positive charge region exists in both situations. Both this hypothesis and the “unshielding” hypothesis allow intracloud lightning to occur simultaneously with the positive ground flashes. More so, the intracloud lightning may “short-circuit” the negative ground flashes since the negative charge layer would be shared for both types of lightning (Williams, 2001). This would further explain the reason for the lack of negative ground flashes observed in PPCG storms.

Several laboratory experiments have investigated the conditions for which particles obtain charge during collisions (Takahashi, 1978; Saunders et al., 1991; Saunders, 1994). Though differences in the results of these experiments have not been resolved, the work of Takahashi (1978) is typically referenced in the literature. This experiment related cloud liquid water content (CLWC) and temperature to the polarity of charge that the larger particle would receive upon collision with another particle (Figure 10). For CLWC near $1\text{-}2\text{ g m}^{-3}$, a charge reversal level of -10° C was found. For especially large values of CLWC, the larger particles were found to obtain a positive charge under all cloud temperatures used in the experiment (0° C to -30° C).

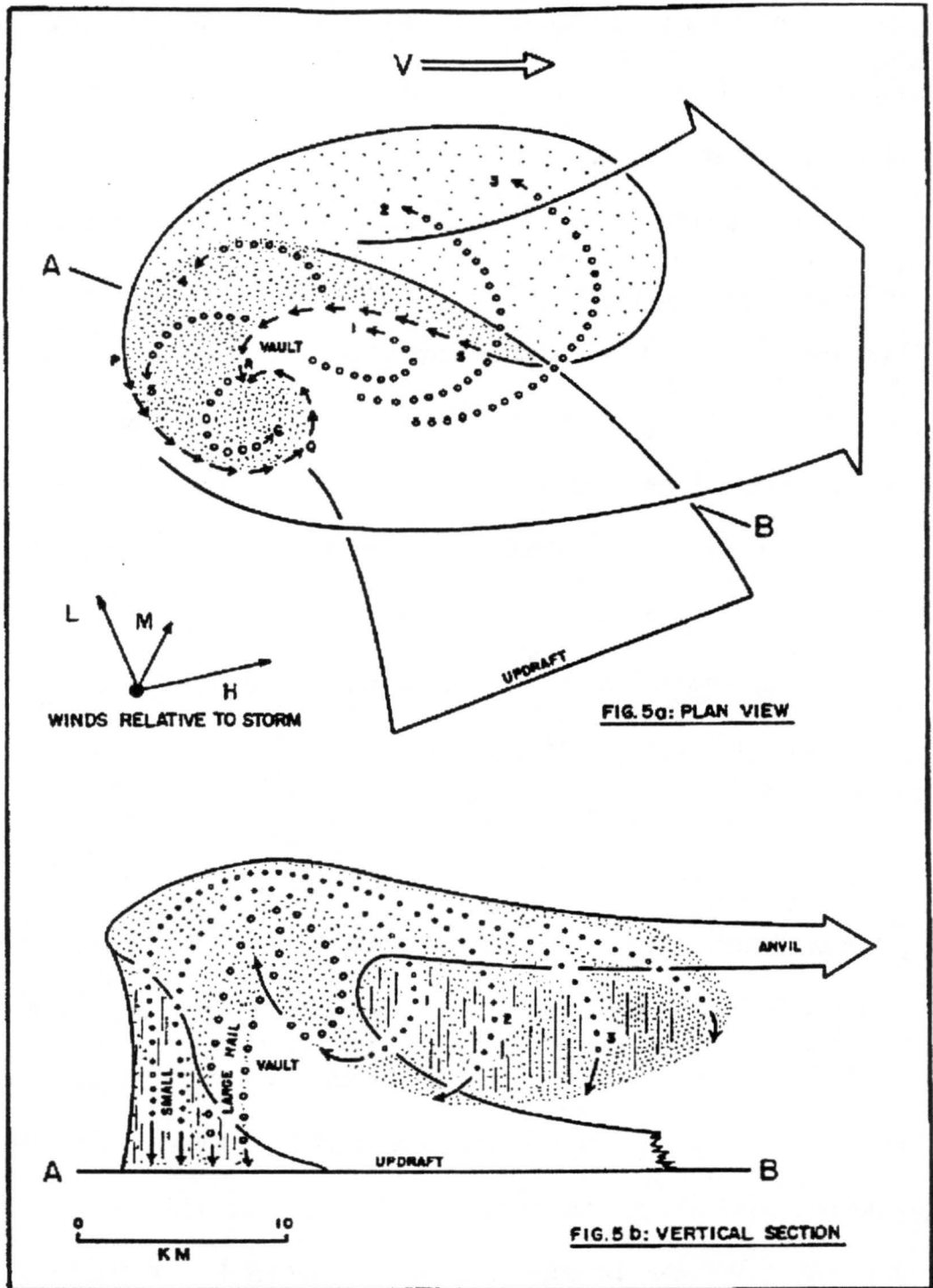


Figure 3. Schematic of a severe storm that travels to the right of the winds from Browning (1964). The storm is traveling at a velocity V , and the winds relative to the storm at the low, middle, and upper levels are depicted as the L, M, and H vectors respectively.

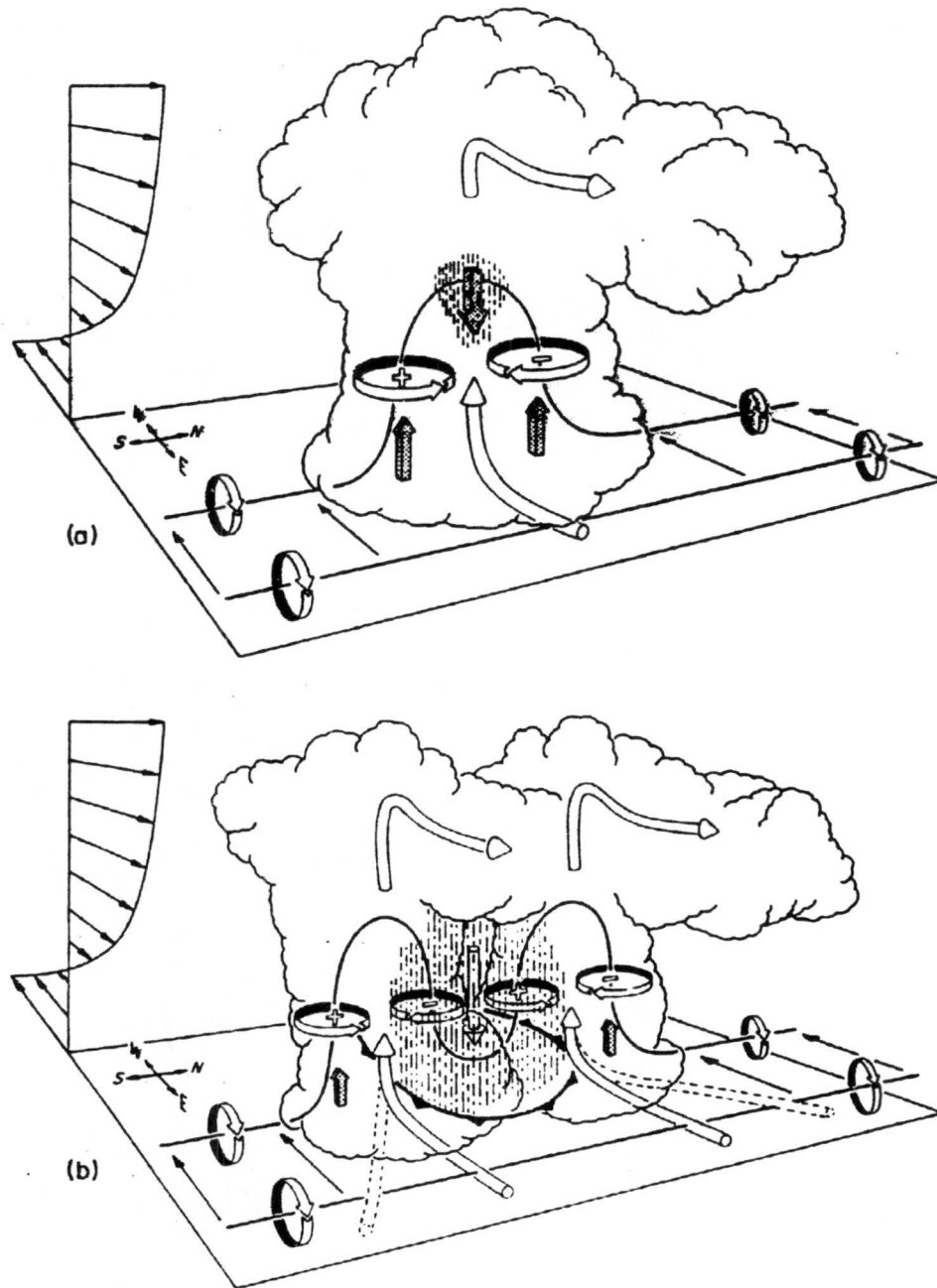
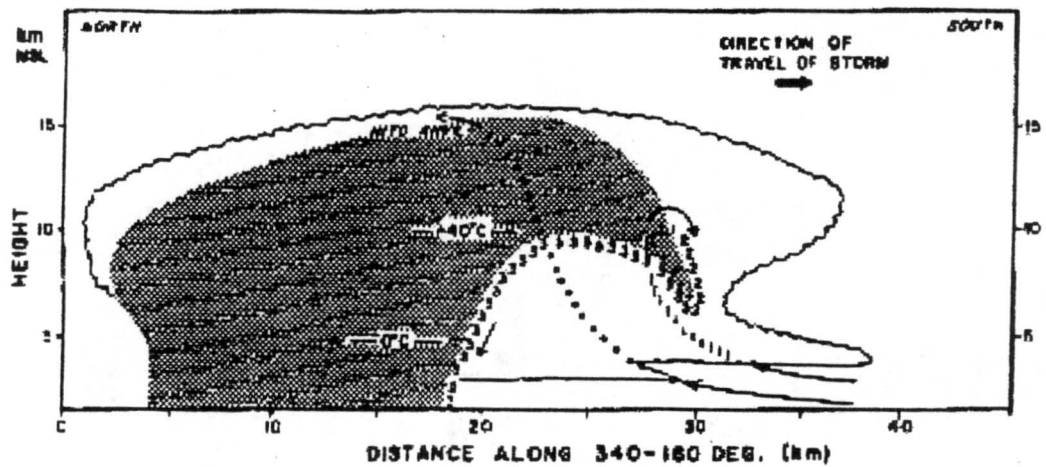
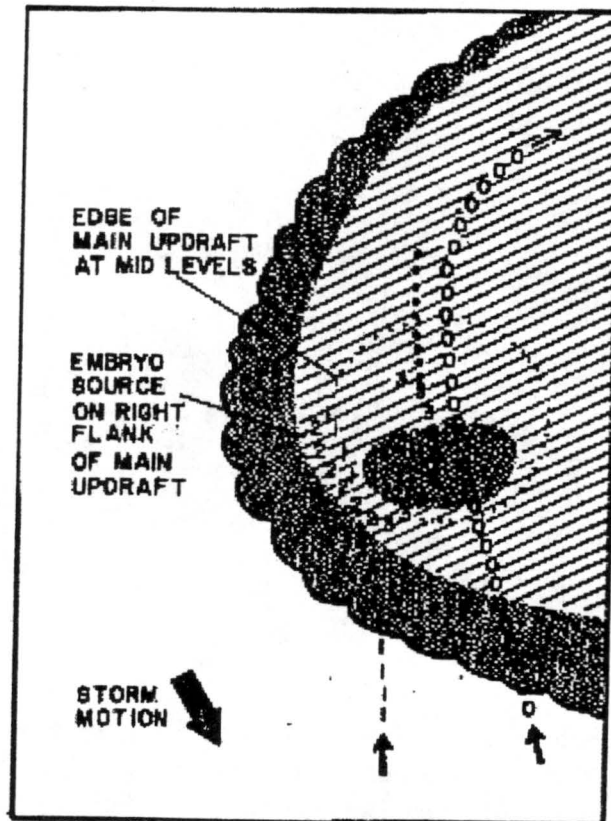


Figure 4. Schematic of how a vortex tube (in a westerly environmental shear regime) interacts with a convective storm. (a) Initial stage in which an updraft draws the vortex tube into the vertical. (b) Splitting stage in which a precipitation-induced downdraft forms between the splitting updrafts and pulls the vortex tube downward. This yields two vortex pairs (from Klemm, 1987)



(a)



(b)

Figure 5. Schematic of hail trajectories in a supercell based on the model of Browning and Foote (1976). (a) shows trajectories in a vertical cross section along the direction of storm motion. (b) shows trajectories in a plan view. Categories 1, 2, and 3 represent the three stages of hail growth outlined in Section 2.2.

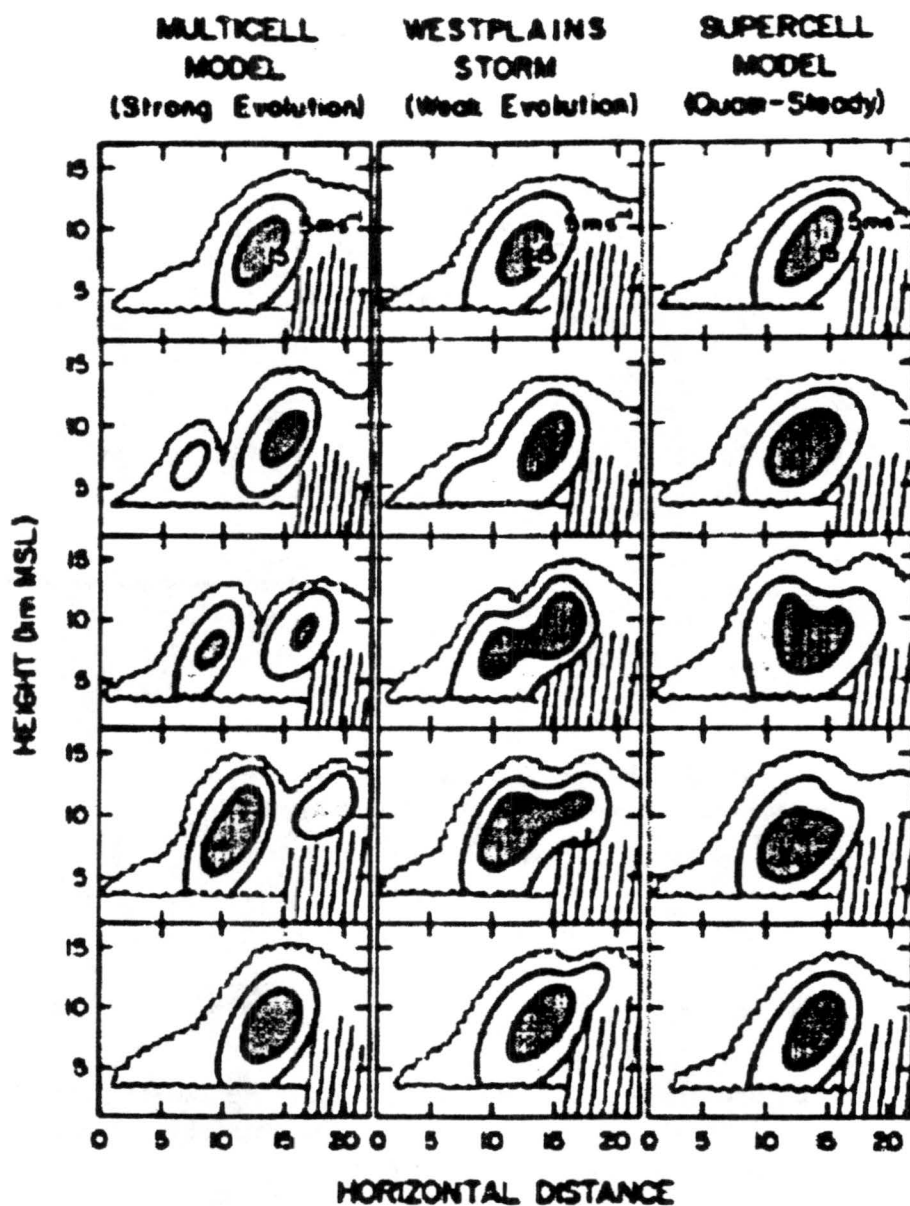


Figure 6. Schematic of updraft evolution as depicted by Foote and Frank (1983). The left column illustrates “strong” evolution, the center column “weak” evolution, and the right column “quasi-steady” evolution. Contours are isotachs of vertical wind speed.

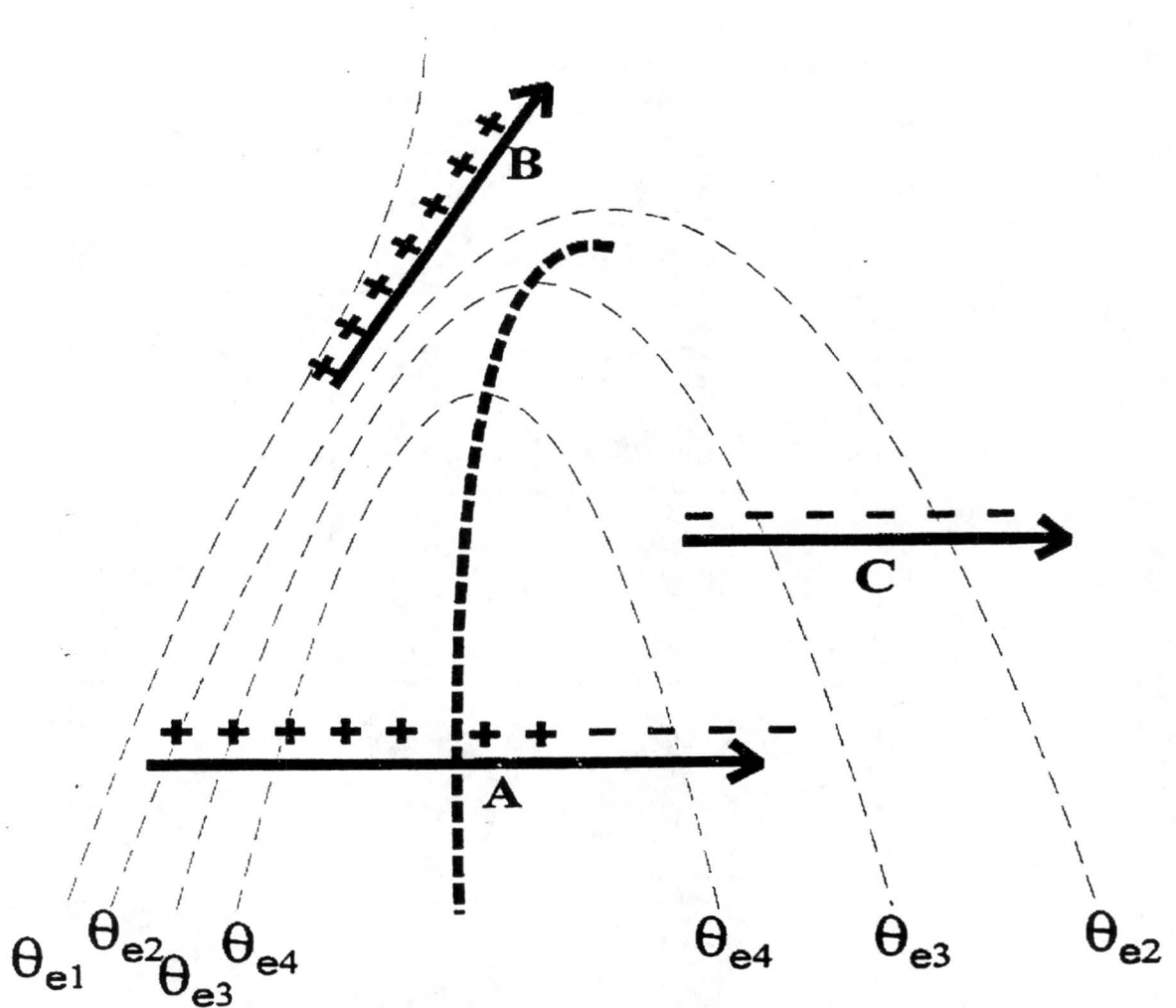


Figure 7. Schematic diagram illustrating that the polarity of cloud-to-ground lightning as a function of location with respect to a surface equivalent potential temperature maximum. Three storm tracks and associated CG lightning polarity are indicated. The θ_e ridge is denoted by the bold dashed line, while contours of surface θ_e are indicated as thin dashed lines (from Smith et al., 2000)

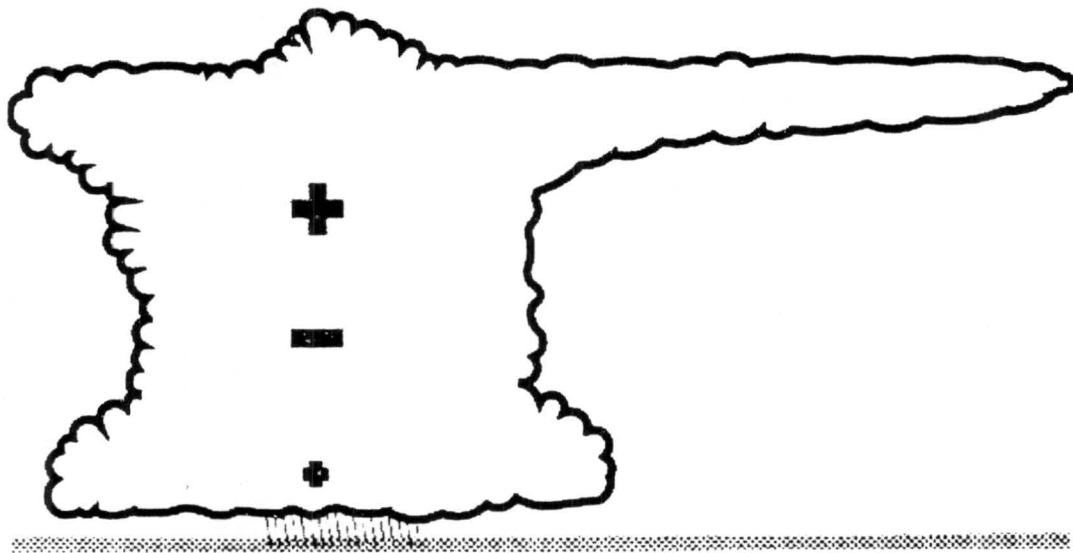


Figure 8. A schematic illustrating the charge structure of an ordinary thunderstorm. The lower positive charge region may not always be present. (MacGorman and Rust, 1998)

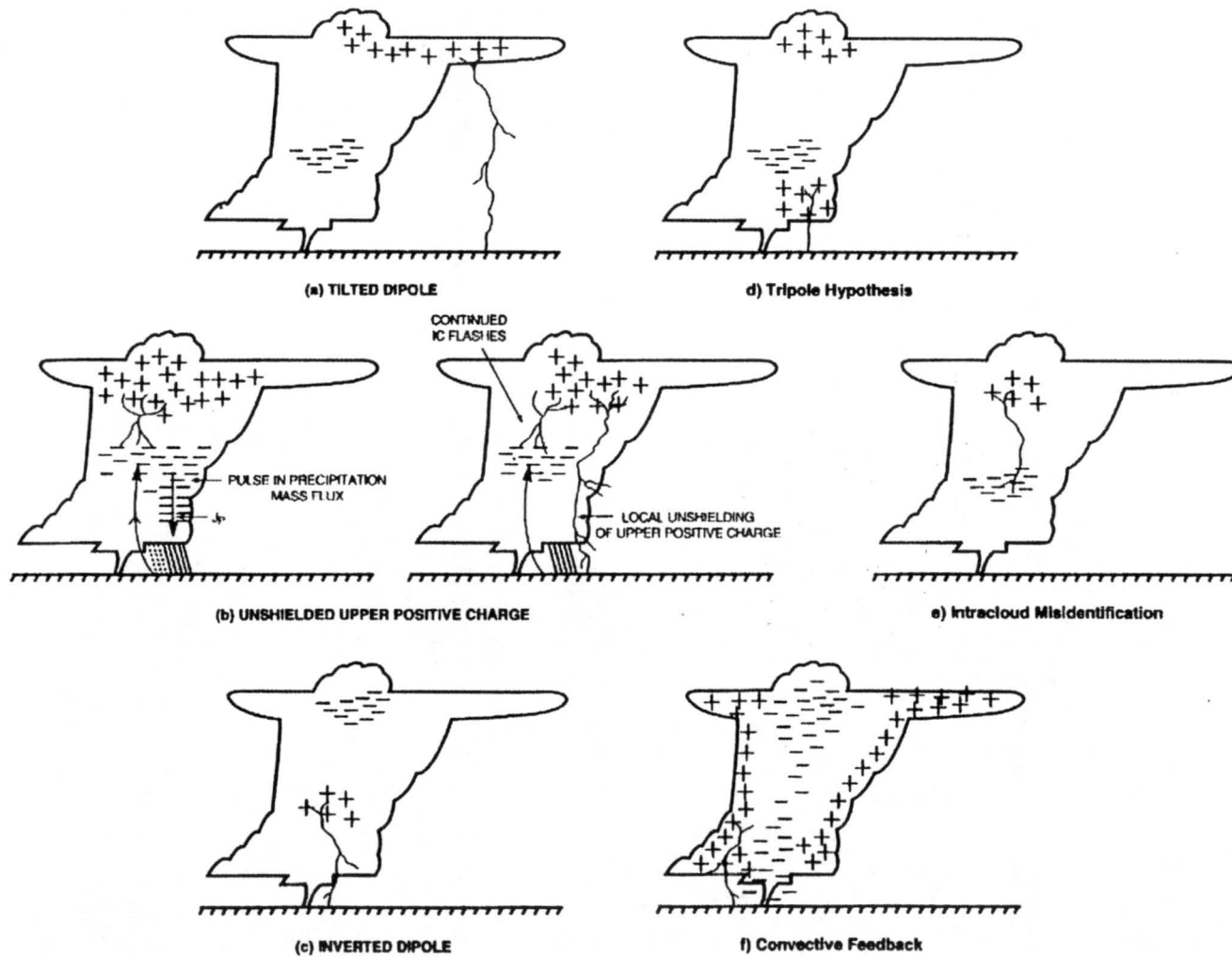


Figure 9. Schematic of hypotheses for positive cloud-to-ground lightning production in severe storms: (a) tilted dipole, (b) precipitation “unshielding”, (c) inverted dipole, (d) tripole. (Williams, 2001)

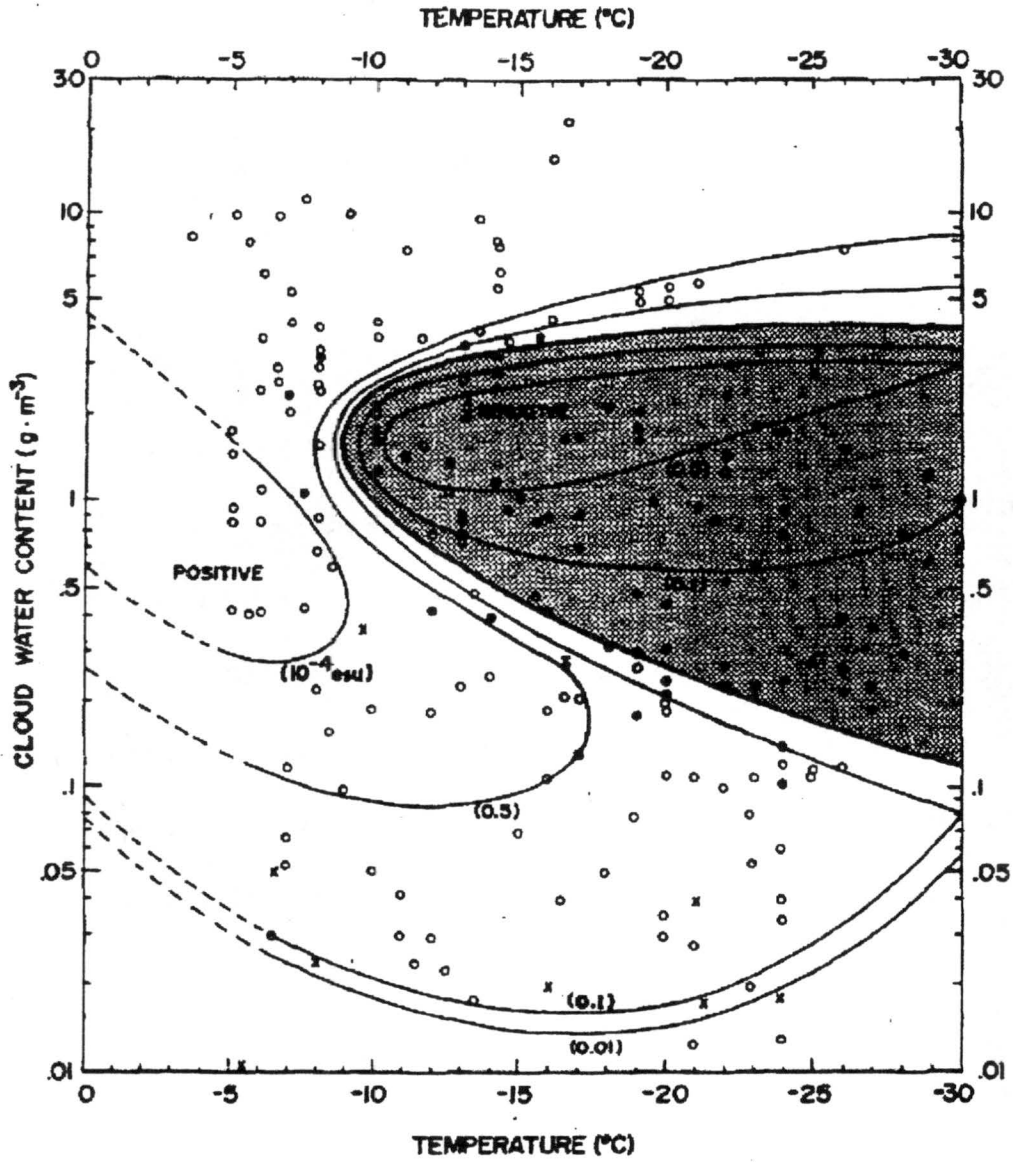


Figure 10. Electrification of rime from Takahashi (1978). Open circles indicate positive charge, solid circles negative charge, and crosses denote uncharged cases.

Chapter 3

DATA AND METHODS

3.1 Radar Variables

Data used in this study were obtained from three radars: the CSU-CHILL and NCAR S-Pol research radars, and the Goodland, Kansas NWS WSR-88D radar. All of these radars measured horizontal reflectivity (Z_h) and radial velocity (V_r) while the CSU-CHILL and NCAR S-Pol radars also measured polarimetric variables (see section 3.2).

Horizontal reflectivity (Z_h) measures the amount of power backscattered in each radar volume. Under Rayleigh scattering assumptions (i.e. where the diameter of the targets are much smaller than the wavelength of the radar), reflectivity depends on the target diameter to the sixth power. The following equation represents the reflectivity factor (Z):

$$Z = \int_0^{\infty} N(D)D^6 dD \quad (3.1.1)$$

where $N(D)$ is the number density and D is the diameter of the targets. In Equation 3.1.1, Z is in linear units of mm^6m^{-3} . However, for meteorological purposes a logarithmic scale is commonly used (see Eqn. 3.1.2).

$$Z_h = 10 \log_{10} Z \quad (3.1.2)$$

This scale yields reflectivity values in dBZ units and ranges from values near zero in cumulus clouds to values greater than 60 dBZ for intense rain or hail storms (Doviak and Zrnić, 1993).

The radial velocity (V_r) measures the mean velocity of particles in the storm along the radial direction (i.e., inbound/outbound to/from the radar). The Doppler-shifted frequency of the moving targets is utilized to calculate this variable. A full description of the Doppler radar techniques used to calculate radial velocity can be found in Doviak and Zrnić (1993) and Bringi and Chandrasekar (2000).

3.2 Polarimetric Variables

In addition to horizontal reflectivity (Z_h) and radial velocity (V_r), the CSU-CHILL and NCAR S-Pol radars measure the following polarimetric variables: differential reflectivity (Z_{dr}), linear depolarization ratio (LDR), the correlation coefficient (ρ_{hv}), and the differential propagation phase (Φ_{dp}). Overviews of polarimetric variables and their use in bulk hydrometeor detection can be found in Herzegh and Jameson (1992), Doviak and Zrnić (1993), Bringi and Chandrasekar (2000), Straka et al. (2000), and many other references.

Differential reflectivity is the ratio between the horizontally and vertically polarized received power from horizontally and vertically polarized transmitted waves. It is defined as $Z_{dr} = 10 \log (Z_{hh}/Z_{vv})$ where the first h and v subscripts refer to the transmitted polarization and the second to that received (this convention may vary by author). Z_{dr} provides a measure of the shape (or oblateness) of precipitation particles. For example, as large raindrops fall they encounter air drag, and become oblate with their

minor axis oriented vertically; thus the Z_{dr} will be positive and increases with increasing drop size (Figure 11). However, as a hailstone falls it tends to tumble and thus appears spherical to the radar. Corresponding Z_{dr} values approach zero. Ambiguities exist in situations where a large hailstone becomes oblate during growth (Browning and Beimers, 1967) or when melting forms a water torus around an ice particle's equator giving it a more oblate shape (Rasmussen et al., 1984). In some instances Z_{dr} values can be negative suggesting large, prolate hail (Doviak and Zrnicek, 1993).

Linear depolarization ratio is a ratio of power returned in the vertical polarization to the power received in the horizontal, using a horizontally polarized transmit pulse, and is defined as $LDR = 10 \log (Z_{hv}/Z_{hh})$. In this fashion, LDR can detect the canting angle of a hydrometeor as it falls. LDR values typically rise when particles become more oblate or their refractive index increases (Doviak and Zrnicek, 1993). Particles with an oblate shape may wobble as they fall and result in a wide spread of canting angles, which would increase LDR. Irregularly shaped particles also can cause increased depolarization and thus elevate LDR. Rain has LDR values between -27 dB and -34 dB, while hail tends to be greater than -20 dB with large, wet hail as high as -10 dB to -15 dB (Doviak and Zrnicek, 1993). Melting snowflakes are also characterized by large LDR values, similar to that of hail, due to their irregular shapes and wet surfaces.

The correlation coefficient, $\rho_{hv}(0)$, at zero time lag between successive pulses of the horizontally and vertically polarized reflectivities depends on the size, shape, canting angle, and differential phase shift upon scattering of the precipitation particles (Doviak and Zrnicek, 1993). The correlation coefficient decreases in mixed-phase situations because the distribution of sizes, shapes, phase and canting angles broaden as the ice

particle size increases (Zrníc et al., 1993b; Carey and Rutledge, 1996). The reduction in $\rho_{hv}(0)$ would be largest if the reflectivity-weighted distributions of the different particle types are similar. If one particle type dominates the reflectivity, then the correlation coefficient is weighted toward that particle type. The correlation coefficient has been used to deduce regions of large (> 2 cm) hail and to distinguish between large and small (< 2 cm) hail by taking into consideration that ρ_{hv} decreases as hail size increases (Balakrishnan and Zrníc, 1990; Kennedy and Rutledge, 1995; Carey and Rutledge, 1998). Standard values of ρ_{hv} are near unity for drizzle, rain, dry snow, and graupel and are greater than 0.9 for a rain and hail mixture (Doviak and Zrníc, 1993). Low ρ_{hv} values, between 0.8 and 0.95, are typical of wet, melting snow which helps identify a bright band (Doviak and Zrníc, 1993).

Specific differential phase (K_{dp}) is derived from the range derivative of the differential propagation phase (Φ_{dp}), which is a measure of the difference between propagation phase constants for horizontally and vertically polarized waves (Carey and Rutledge, 1996). Specific differential phase is insensitive to isotropic scatterers (i.e. quasi-spherical and/or tumbling hail), but very sensitive to anisotropic scatterers (i.e. oblate raindrops). Therefore, in a mixed phase environment, K_{dp} can be used to discriminate between rain and hail. Specific differential phase is linearly related to the liquid water content of precipitation, which allows for more accurate rainfall estimations, especially in rainfall greater than 60 mm h^{-1} (Jameson, 1985; Chandrasekar et al., 1990).

3.3 Multiple-Doppler Radar Analysis

Wind field syntheses were completed for 36 volume scans during the period 2130 UTC (29 June)-0115 UTC (30 June), yielding approximately six-minute time resolution. Radar data from each radar were interpolated onto a Cartesian grid using NCAR's Sorted Position Radar INTerpolator (SPRINT). Grid resolution was 0.5 km in both the horizontal and vertical directions. Before the interpolation process, the velocities were locally unfolded to place adjacent measurements used in the bi-linear interpolation within a new Nyquist co-interval centered on one of the measured values rather than zero. This process maintains the discontinuity that was originally due to folding (Miller et al., 1986). After the grid interpolation, the velocity data were globally unfolded by means of NCAR's Custom Editing and Display of Reduced Information in Cartesian Space (CEDRIC) software (Mohr et al., 1986). CHILL data were omitted where polarimetric measurements indicated a second trip echo, and S-Pol radial velocities were omitted where sidelobe contamination was suspected. The three dimensional wind fields were computed using the radial velocities from all three radars when available; otherwise winds were computed from only two radars. The speed and direction of storm movement were calculated and used for the advection parameters. The vertical velocities were obtained by integrating the continuity equation (Eqn. 3.3.1) via three methods: upward, downward, and variationally (O'Brien, 1970).

$$\frac{\delta(\rho w)}{\delta z} + \frac{\delta(\rho u)}{\delta x} + \frac{\delta(\rho v)}{\delta y} = 0 \quad (3.3.1)$$

All three results were evaluated, and the variational integration scheme was used for this analysis (see Appendix for details and limitations of the multiple radar data analysis methods).

The three-dimensional wind fields derived in the multiple-Doppler analysis were used to calculate vertical vorticity and to evaluate the vorticity tendency equation. Vertical vorticity (ζ) was calculated at each grid point as a centered finite difference following Equation 3.3.2.

$$\zeta = \frac{\partial v}{\partial x} - \frac{\partial u}{\partial y} \quad (3.3.2)$$

The variables u and v are the x and y components of the horizontal wind field respectively. Vorticity tendency was calculated at each grid point using the equation for the material rate of change for vertical vorticity (Eqn. 3.3.3).

$$\frac{D\zeta}{Dt} = -\underbrace{\zeta \left(\frac{\partial u}{\partial x} + \frac{\partial v}{\partial y} \right)}_{\text{stretching}} - \underbrace{\left(\frac{\partial w}{\partial x} \frac{\partial v}{\partial z} - \frac{\partial w}{\partial y} \frac{\partial u}{\partial z} \right)}_{\text{tilting}} \quad (3.3.3)$$

Ground-relative wind vectors calculated from the wind field syntheses were used to directly calculate the stretching and tilting terms of Equation 3.3.3, and the total tendency was then calculated as a residual. Planetary vorticity was neglected in this calculation since it has little effect at the storm scale. The solenoidal term in the full vorticity tendency equation could not be calculated due to a lack of thermodynamic data. Our derivation assumes that the solenoidal production of vertical vorticity was small compared to that produced by stretching and tilting.

3.4 Polarimetric Radar Analysis

The polarimetric data were edited to eliminate noise, clutter, and suspect data following the methods of Ryzhkov and Zrníc (1998). The processed data were then gridded in the same manner as described above. A hydrometeor classification scheme,

adapted from Carey and Rutledge (1998) and Straka et al. (2000), was implemented to estimate bulk hydrometeor types within the storm. The criteria used for hydrometeor classifications are listed in Table 2. Hydrometeor echo volumes were then calculated by multiplying the number of grid points (N) that satisfied the category of interest by the volume of a grid box ($N \cdot 0.125 \text{ km}^3$).

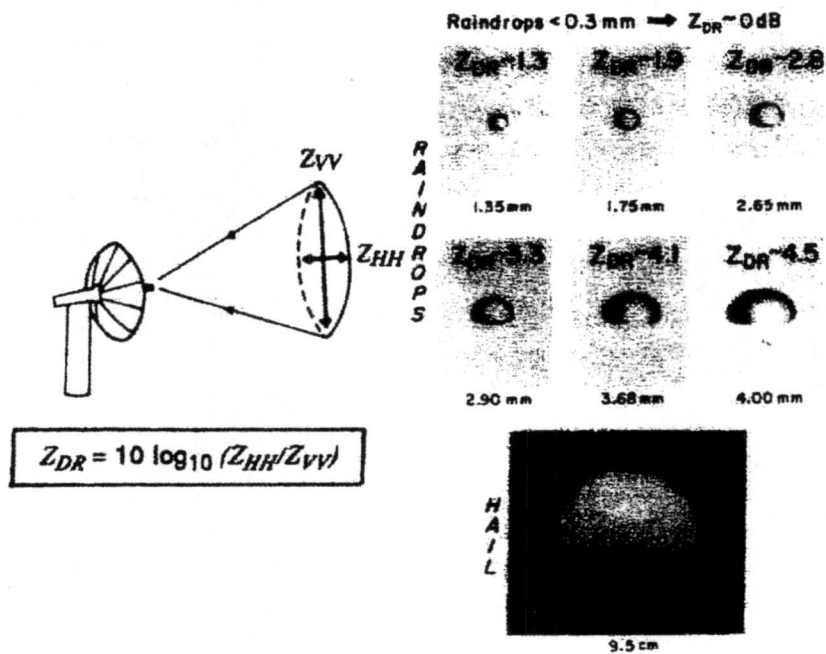


Figure 11. Illustration of precipitation particle and associated differential reflectivity (Houze, 1993).

Table 2. Hydrometeor classification criteria

	HYDROMETEOR	ZH (DBZ)	ZDR (DB)	LDR (DB)	KDP (DEG/KM)	RHV
T ≥ 0°C						
	1, Small hail (D < 2 cm)	≥ 50	≤ 0.5	< -18	< 0.5	> 0.96
	2, Small hail/rain	≥ 50	< 1.0	-27 to -20	≥ 0.5	≤ 0.98
	3, Large hail (D > 2 cm)	≥ 55	≤ 0.5	≥ -18	< 0.5	≤ 0.96
	4, Large hail/rain	≥ 55	< 1.0	≥ -20	≥ 0.5	≤ 0.96
	5, Rain	35 to 60	not used	not used	not used	not used
T < 0°C						
	6, Dry Hail (D > 1 cm)	≥ 55	not used	> -26	< 0.5	> 0.96
	7, Wet Hail (D > 1 cm)	≥ 55	not used	≥ -20	-0.5 to 1.0	< 0.97
	8, Graupel (D < 1 cm)	35 to 55	not used	≤ -20	< 0.5	> 0.95
T ≤ -20°C						
	9, Vertically oriented ice	< 40	not used	not used	< -0.25	not used

Chapter 4

ENVIRONMENTAL CONDITIONS

4.1 Synoptic Environment

The synoptic conditions, prior to the onset of the 29 June supercell included a weak ridge over the western U.S. and a weak trough over the eastern U.S. with a jet streak at 250 mb that may have induced some upward vertical motion in its right entrance quadrant over the region in which the storm developed (Figure 12). Upper-level confluence (at 250 mb) of two branches of the jet and negative vorticity advection (at 500 mb) were two features that offset the upper-level support for upward vertical motion in this region; however, according to Doswell (1980), High Plains thunderstorms tend to lack well-defined upper-air features (500 mb and higher). Therefore, it is not uncommon for convection in this region to be forced by low-level mesoscale features. A low-level jet at 850 mb was present and, coupled with a ridge of high equivalent potential temperature (θ_e) air, enhanced the low-level wind shear and the buoyancy of the air ingested into the storm (Figure 13).

4.2 Thermodynamic Structure

The environmental soundings (Figure 14) from the NCAR Mobile GPS/Loran Sounding System (MGLASS) on 29 June 2000 indicated that there was moist, southerly

flow in the pre-storm environment ahead of the advancing surface boundary. This boundary was oriented northeast to southwest in the northwestern corner of Kansas and propagating to the southeast. The wind profile for 2022 UTC (Figure 14a) at Goodland indicated a southerly component to the low-level flow and veering winds up to the tropopause ahead of the surface boundary. Convective Available Potential Energy (CAPE) was also abundant (1254 J kg^{-1} according to Figure 14a, but estimated to be as high as 4000 J kg^{-1} based on RUC-2 model data). High surface-based CAPE values and a veering wind profile with height, favor severe thunderstorm development (Moller et al. 1994). The hodograph at this time indicated that a right-moving storm would be favored if storm splitting were to occur. A sounding taken at 2338 UTC (Figure 14b) behind the surface boundary showed a much drier environment, and since the storm seemed to form along this boundary, at times the upwind side of the storm was exposed to this drier air. The winds from the 2338 UTC sounding showed veering in the low-levels and slight backing from northwesterly to westerly between 650 mb and 350 mb. The upper-level winds at both times were westerly and as strong as 40 m s^{-1} .

4.3 Surface Conditions

The surface conditions, characterized by warm temperatures and high dew points, were optimal for convection. By 2100 UTC temperatures were in the mid-to-upper $80^{\circ}\text{s}^{\circ}\text{F}$ ($\sim 30^{\circ}\text{C}$) and dew points were near 60°F (15.5°C) ahead of the outflow boundary (OFB) that propagated into northwestern Kansas. Behind the OFB, the temperatures were still warm yet the dew points were in the $30^{\circ}\text{s}^{\circ}\text{F}$ (-1.1°C). The OFB was recognized in the surface observations by a wind shift line that was traced from central

Wyoming as far back as 1200 UTC, and was first seen by radar as a thin line echo in northeastern Colorado near 2000 UTC. As alluded to above, this OFB was a likely trigger for the convection that initiated this storm.

Wind Speed (m/s)
2100Z (250 mb)

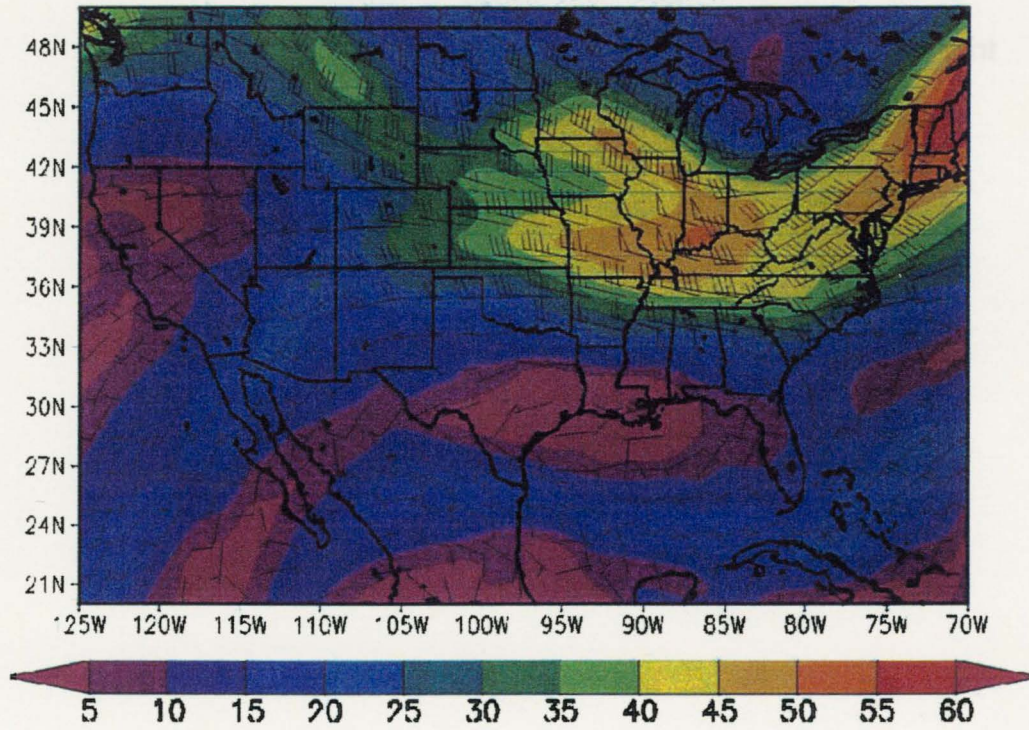
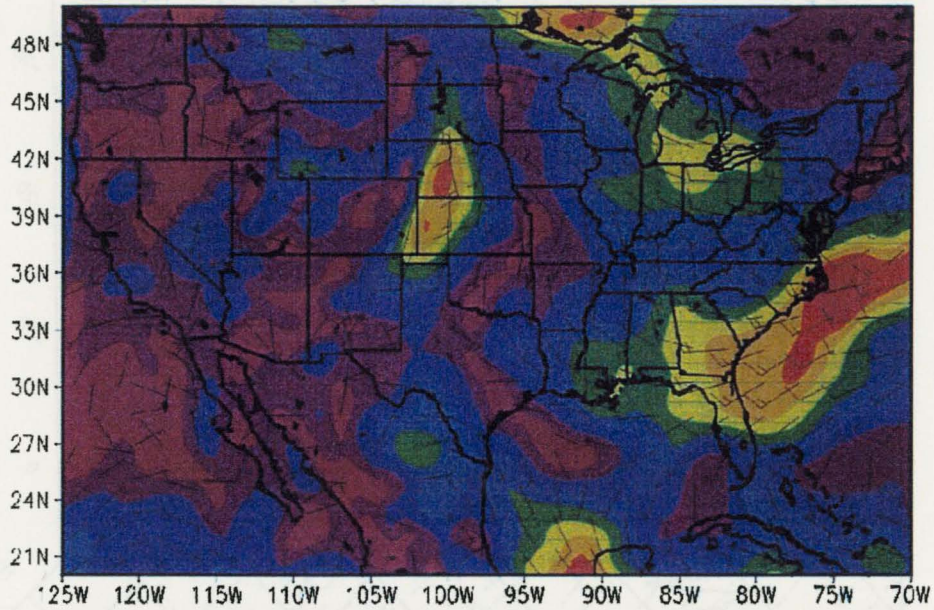


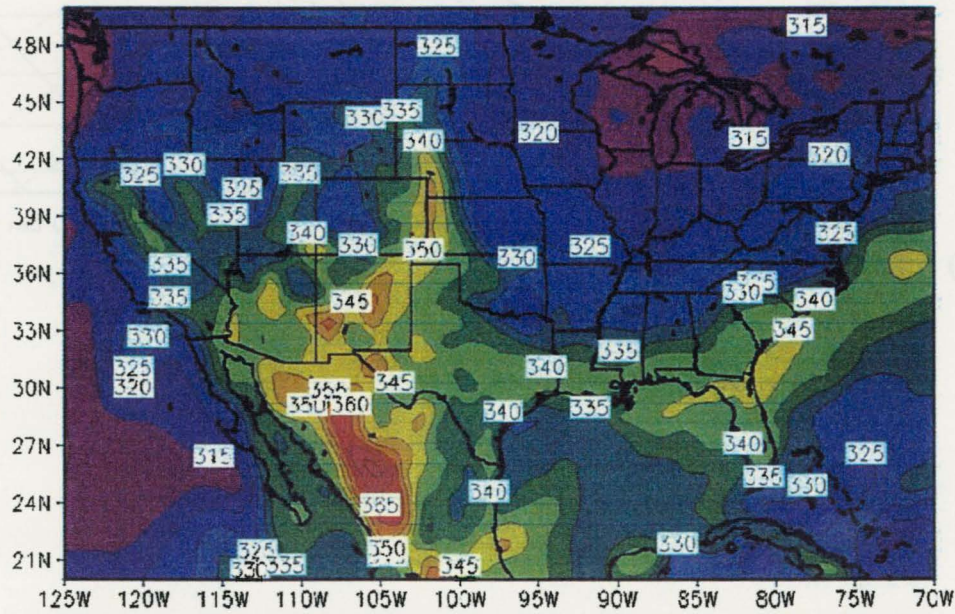
Figure 12. 250 mb RUC-2 wind analysis for 2100 UTC on 29 June 2000. Wind barbs are overlaid in black.

Wind Speed (m/s)
2100Z (850 mb)



a)

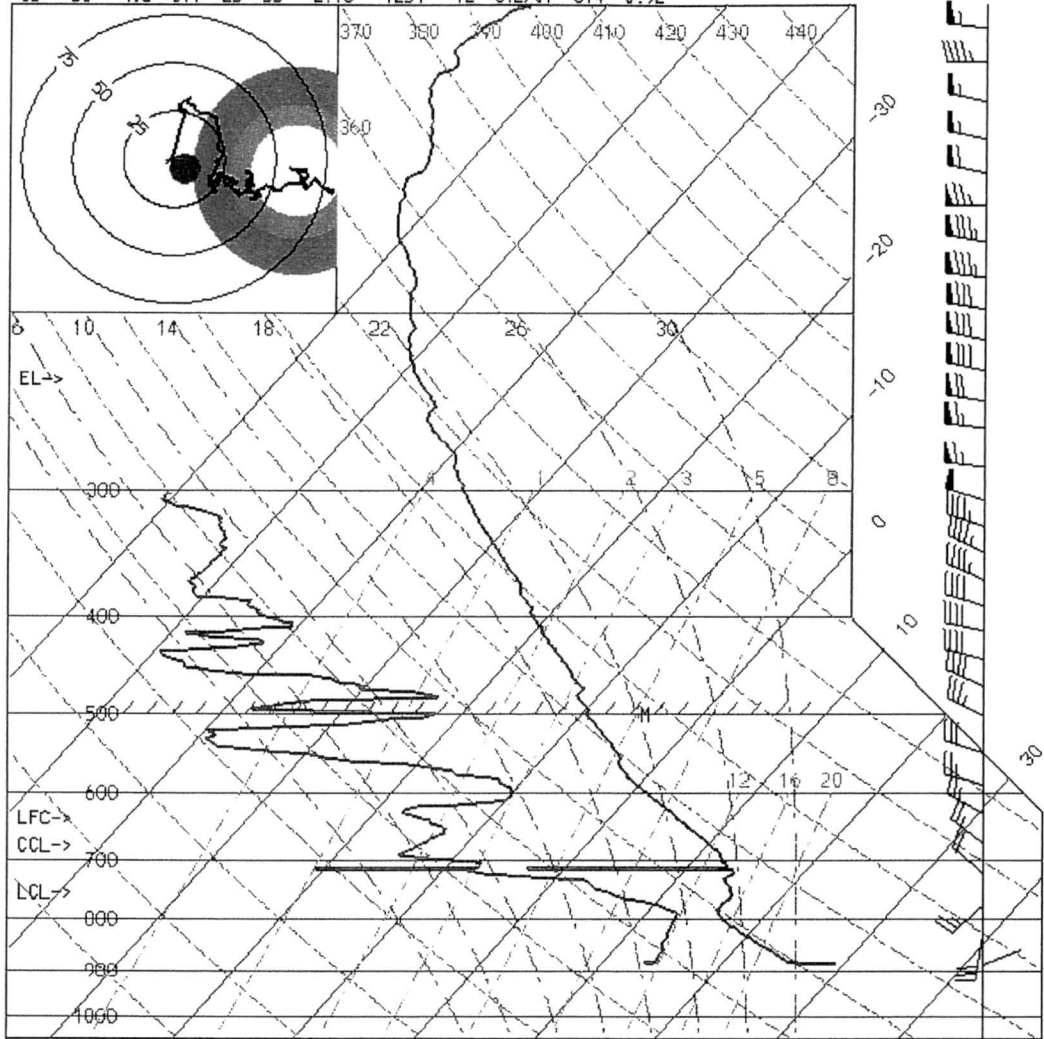
Equivalent Potential Temperature (K)
2100Z 29JUN(850 mb)



b)

Figure 13. 850 mb RUC-2 analysis for 2100 UTC on 29 June 2000. Contours are of (a) wind speed and (b) equivalent potential temperature. Wind barbs are overlaid in black on (a).

T(F) Td LI SWT K TT Pw(cm) CAPE Tc CELL SREH YGP
 85 58 -4.8 517 25 55 2.18 1254 92 312/07 314 0.92



SKEN-T/LOG-P VALID 2022 UTC 06/29/00 et1

Lat = 39.37 , Lon = -101.70

a)

Chapter 5

AIRFLOW AND MICROPHYSICAL STRUCTURE

5.1 Storm Overview

The 29 June 2000 supercell (referred to as storm Storm I; see Figure 15) was first detected as a small echo at 2130 UTC along a southeastward-moving outflow boundary. Another storm (II in Figure 15) persisted throughout most of Storm I's lifetime, although it did not become severe, in sharp contrast to Storm I's behavior. During the period 2130-2325 UTC, prior to the tornadic stage, Storm I moved southeastward, toward 115° , at a speed of 9.7 m s^{-1} . By 2230 UTC, it began exhibiting high reflectivities near 65 dBZ. A bounded weak echo region (BWER), indicative of a strong updraft, was evident around 2233 UTC. According to the online *Storm Data* (maintained by the National Climatic Data Center on the internet at <http://www4.ncdc.noaa.gov/cgi-win/wwcgi.dll?wwEvent~Storms>), large hail ($D > 2 \text{ cm}$) was first reported at 2235 UTC. Hail as large as 4.5 cm in diameter was reported at 2307 UTC. The first cloud-to-ground (CG) lightning flash (positive CG) was detected by the NLDN near 2245 UTC; however, CG flash rates did not become noteworthy until $\sim 2328 \text{ UTC}$ (Figure 16). At this point in time, the storm turned right and began to travel somewhat more slowly with a velocity of 8.9 m s^{-1} towards 150° (Figure 17). Vigorous positive CG lightning activity commenced, and a deep mesocyclone was also observed. A tornado was first reported at 2328 UTC, however, a hook echo was not observed in the low-level reflectivity structure until 0004

UTC (Figure 18). The tornado¹ (categorized as F1 on the Fujita scale) remained on the ground until 2344 UTC. At 0004 UTC (30 June), the low-level radar reflectivities resembled a “classic” supercell with a gust front and hook echo (Figure 18). Prior to this time, the low-level storm structure was quite variable. By 0054 UTC, the storm exhibited large radar reflectivities (up to 75 dBZ) and was producing large hail (up to 4.5 cm in diameter) according to storm reports². The storm began to dissipate near 0200 UTC and was all but non-existent by 0400 UTC.

As previously mentioned, appreciable CG flash rates did not commence until near 2328 UTC. Only one CG strike, of positive polarity, was detected prior to this time. A total of 171 CG strikes were observed by the NLDN for this storm, and of that 157 (~92%) were positive (Figure 16). Total lightning flash rates (calculated according to the method outlined in Wiens et al., 2002) were as high as 300 flashes per minute when averaged over the time of each radar volume. CG flash rates (also averaged over the time of the radar volume) reached 5 flashes per minute just beyond the end of the analysis period, but peaked between 2-3 flashes per minute within the analysis period. As can be clearly seen in the bottom panel of Figure 16, positive CG lightning dominated the flash rates for every radar volume.

5.2 Time Series Analysis

On the overall timescale of this detailed analysis period (nearly 3 hours), the storm’s intensity (indicated by updraft volume) continually increased, until approximately 0010 UTC, and then it leveled off and gradually began to decrease beyond

¹ Tornado report was obtained from Mobile Mesonet observations.

² Hail report obtained from Mobile Mesonet observations.

0023 UTC (Figure 19). The total echo volume of precipitation below the melting level continued to increase for the entire analysis period (Figure 20). The rain echo volume (volume of grid points satisfying category 5 in Table 2) dominated this trend.

On shorter timescales, of approximately 30-50 minutes, both the updraft strength and the volume of significant updrafts were observed to pulse. This is clearly evident in time series depictions of storm updraft statistics (Figure 19, Figure 21, Figure 22). The magnitude and vertical extent of maximum updraft in each pulse increased with time (Figure 22). Since the updraft supplies supercooled water droplets which accrete onto ice particles forming graupel and hail, and the stronger the updrafts are the more likely hail will form because the updraft can suspend larger particles aloft, it is likely that a relationship between the updraft strength and microphysical trends exists. The following discussion documents each noteworthy pulse of the updraft and microphysical characteristics over the duration of the analysis period. Vertical vorticity is also analyzed as a function of updraft pulse in order to provide a more complete description of the storm kinematics. For easier reference, the entire analysis period has been divided into shorter time periods (A, B, C...) defined by their updraft volume trends (as seen in Figure 19).

5.2.1 Period A

Updraft pulses between 2130 and 2213 UTC were weak and did not contain much volume relative to the size of the storm at later times (Figure 19). Maximum updrafts were near 15 m s^{-1} and resided between 7-10 km MSL (Figure 22). Graupel echo volume aloft (number of grid points satisfying category 8 in Table 2 multiplied by the volume of

each grid box) began to increase between 2144 and 2159 UTC when it increased to near 50 km^3 and increased in vertical extent up to 11 km MSL (Figure 23). Following the increase in graupel echo volume, IC flashes were observed at an approximate rate of 25 flashes per minute (Figure 16).

5.2.2 *Period B*

The storm exhibited a maximum in upward vertical velocity (between $30\text{-}35 \text{ m s}^{-1}$) near 2220 UTC (Figure 21). A sharp increase in updraft strength was evident just prior to this time. Lower levels in the storm were now filled with updrafts to 20 m s^{-1} (near 3 km MSL; Figure 22). A bounded weak echo region (BWER) was present in the midlevel reflectivity structure at 2233 UTC (Figure 24 shows the BWER at 2239), also consistent with the presence of a strong updraft. An associated increase in updraft volume began at 2213 UTC and further increased until 2246 UTC, with a small peak at 2233 UTC (Figure 19). The maximum updraft was centered at about 12 km MSL at 2246 UTC and had increased to over 40 m s^{-1} (Figure 22). Some pockets of maximum vorticity up to $12 \times 10^{-3} \text{ s}^{-1}$ were first seen between 2227 to 2252 UTC scattered in the 6-9 km MSL levels (Figure 25). Graupel echo volume extended up to 13 km MSL by this time, and exhibited values up to 75 km^3 (Figure 23). A marked increase in the hail echo volume aloft (volume of grid points satisfying categories 6 and 7 in Table 2) was seen at 2246 UTC (Figure 26), corresponding to the peak in updraft volume. A subsequent peak in small hail ($D < 2 \text{ cm}$) echo volume, and somewhat in large hail ($D > 2 \text{ cm}$) echo volume, below the melting level (volume of grid points satisfying categories 1 and 2 for small hail and 3 and 4 for large hail in Table 2) was seen at 2252 UTC (Figure 20),

implying that the large hail aloft had descended in the storm. The total flash rate increased to near 75 flashes per minute in this period, and the first CG flash occurred near 2245 UTC and was positive (Figure 16). This positive CG was concurrent with the first maximum in hail echo aloft and preceded the detection of hail in lower levels of the storm.

5.2.3 *Period C*

A second, small pulse in updraft volume was apparent at 2312 UTC (Figure 19). The maximum updraft by this time was near 50 m s^{-1} (Figure 21). The center of this maximum updraft was situated near 13 km MSL (Figure 22). A corresponding BWER at 2312 UTC and a short-lived pulse in hail echo volume at 2318 UTC were observed (Figure 26). A peak in large hail echo volume below the melting level was seen at 2325 UTC (Figure 20). The graupel echo volume now extended as high as 14 km MSL (Figure 23). The maximum vorticity was still near $12 \times 10^{-3} \text{ s}^{-1}$, yet it now extended between 6-10 km MSL (Figure 25). Maximum total flash rates were near 50 flashes per minute, and a second CG flash was observed near 2317 UTC, which was of negative polarity (Figure 16).

5.2.4 *Period D*

The updraft volume (contained by the 10 m s^{-1} contour) nearly doubled between 2318-2343 UTC. A considerable increase in the $\geq 20 \text{ m s}^{-1}$ updraft volume was also apparent (Figure 19). The maximum updraft speeds were still near 50 m s^{-1} (Figure 21) and was now centered around 9 km MSL (Figure 22) at 2331 UTC. Clearly the storm

was intensifying at this time. Concurrently, vigorous positive CG lightning activity began, accompanied by the touchdown of the tornado (Figure 17). Previous studies have documented anomalous CG lightning activity in some storms that produce tornadoes (Seimon, 1993; MacGorman and Burgess, 1994; Perez et al., 1997; Carey and Rutledge, 1998; Gilmore and Wicker, 2002; Carey et al., 2002b). Many of these studies found that storms dominated by positive CG lightning produced tornadoes after a maximum in positive CG flash rate, during a relative minimum in CG lightning activity, or during a reversal from positive to negative polarity CG lightning. However, consistent with this study, Carey et al. (2002b) found that for a tornadic storm on 30 May 1998 positive CG lightning activity increased during the touchdown of its tornado.

A BWER was also detected at 2325 UTC and it persisted until 2343 UTC, at which time the BWER's bordering reflectivities were remarkably high (~ 60 dBz; Figure 27). Midlevel maximum vorticity rapidly increased at 2325 UTC and achieved values to $28 \times 10^{-3} \text{ s}^{-1}$ by 2331 UTC (Figure 25). Values of vertical vorticity up to $16 \times 10^{-3} \text{ s}^{-1}$ ranged from 2.5 km MSL to near 12.5 km MSL by 2338 UTC, yielding maximum vorticity of this strength or greater throughout 10 km of the storm's depth. This value is consistent with previous studies (Ray, 1976). Furthermore, these values are above those values typically associated with a mesocyclone (10^{-2} s^{-1} , Brown and Meitin, 1994).

Graupel echo volumes reached 15 km MSL in this period and were as great as 150 km^3 (Figure 23). The hail echo volume aloft also dramatically increased in the latter half of this period, yielding a large reservoir of hail (up to 55 km^3) just above the melting level and centered near the -10° C isotherm at 2343 UTC (Figure 26). A substantial peak in the low-level small hail echo volume (Figure 20) was apparent at 2351 UTC. Total

flash rates increased up to 200 flashes per minute, and the total CG flash rate was as high as 5 flashes per minute (Figure 16). A peak in positive CG flash rate (2.5 flashes per minute) occurred near 2343 UTC. As in period B, the positive CG flashes were correlated with hail echo aloft. Contrary to the findings of Carey and Rutledge (1998) that large hail and positive CG lightning were anticorrelated, the hail and positive CG flash rate in this storm seem to be well correlated.

5.2.5 *Period E*

Another noteworthy pulse in the 10 m s^{-1} and 20 m s^{-1} updraft volume occurred between 2357-0010 UTC (Figure 19). The maximum updraft speed continued to peak near 50 m s^{-1} (Figure 21). A hook echo was present in the horizontal reflectivity structure (Figure 18). At this time, the hail echo volume aloft also exhibited a substantial peak not only in volume, but also in vertical extent as hail was detected up to 13 km MSL (Figure 26). A subsequent peak in large hail echo volume below the melting level was seen at 0010 UTC (Figure 20). The total flash rate remained high (near 200 flashes per minute), as did the total CG flash rate, however, the positive CG flash rate went down during this period (Figure 16). It could be speculated that the positive CG flash rate decreased at this time due to less hail echo concentrated in the -10° C regime, rather it was dispersed throughout a great depth of the storm, reaching much colder growth temperatures. Implications of hail growth regimes influencing CG polarity will be discussed further in section 5.2.8.

5.2.6 *Period F*

At 0023 UTC the updraft volume was at its maximum for this analysis period (Figure 19), a BWER was observed in the reflectivity field (Figure 28), and a short peak in hail echo volume aloft occurred subsequently at 0030 UTC (Figure 26). The maximum updraft speed persisted near 50 m s^{-1} (Figure 21). Low-level vorticity and large hail echo volume below the melting level also started to increase at this point (Figure 20, Figure 25). The total flash rate increased to near 300 flashes per minute near 0023 UTC, and near 0030 UTC the positive CG flash rate was as high as 3 flashes per minute (Figure 16). The hail echo maximum was again coincident with positive CG flashes, in contrast to the previously mentioned findings of Carey and Rutledge (1998).

5.2.7 *Period G*

The last pulse in updraft volume began at 0043 UTC (Figure 19) with an associated BWER (Figure 29). Strong vorticity extended throughout a 6 km depth of the storm and was as high as $24 \times 10^{-3} \text{ s}^{-1}$ (Figure 25). A maximum in hail echo volume aloft was found at 0049 UTC (Figure 26) and a corresponding peak in large hail echo volume below the melting level occurred immediately afterward at 0056 UTC (Figure 20). The total flash rate had diminished to between 200-250 flashes per minute by this time, and the positive CG flash rate was down to 2 flashes per minute (Figure 16).

5.2.8 *Summary of time series findings*

The updraft volume and strength were observed to pulse on approximately 30-50 minute timescales. In general, the updraft volume tended to level off as hail volume aloft

was increasing and near a local maximum, possibly indicating that precipitation loading countered the acceleration and growth of the updraft at those times. Furthermore, as the updraft volume leveled off and began to decrease, its capability to suspend hail aloft decreased, as seen in the subsequent decreases in hail volume aloft after the updraft volume began to decrease. This implies that the formation and fallout of hail could be responsible for the pulsing of the updraft that was observed.

Positive CG flashes were well correlated with maxima in hail echo volume above the melting level, particularly when the hail was growing near -10° C or warmer. This result differs from the study by Carey and Rutledge (1998) where they studied a storm on 7 June 1995 and found large hail and positive CG lightning to be anticorrelated, with peaks in positive CGs occurring 20-35 minutes after peaks in large hail. However, that study focused on hail falling from the storm at 0.5 km AGL, whereas this work focuses on hail production within the storm (above the melting level). Consistent with Carey et al. (2002b), the positive CG lightning flash rate increased as the storm became tornadic.

Overall, the maxima in hail echo volume above the melting level occurred at or near the -10° C level (~ 7 km MSL). For storms with cloud liquid water contents (CLWCs) between $1-5 \text{ g m}^{-3}$, the work of Takahashi (1978) implies that ice particles growing in regimes warmer than -10° C will experience positive charging, while those growing in regimes cooler than -10° C will experience negative charging (Figure 10). The CLWC of this storm near 7 km MSL (the -10° C level)³ was between 4 and 5 g m^{-3} (Figure 30). This implies that the hail growing in this storm was possibly in a positive charging regime which might support a reason why the maxima in hail echo volume

³ An NSSL in situ electric field sounding at 0004 UTC was used to estimate the temperature level heights.

above the melting level were coincident with maxima in positive CG flash rates. In situ CLWC measurements of this storm by Detwiler et al. (2002) confirm this result.

5.3 Detailed Analysis of Selected Intensification Periods

5.3.1 Period B

The period 2239-2246 UTC was interesting because the first cloud-to-ground lightning strike was detected. Nearly an hour after the intra-cloud (IC) lightning activity had initiated, one lone CG occurred at 2245 UTC and most interestingly, was of positive polarity. An additional feature in the time series that makes this time period appealing was that the first noteworthy peak in the hail echo volume aloft was detected. Since the hail echo volume maximum was centered around the 7 km level, a closer look at the radar observations at this level will follow.

At 2239 UTC the 7 km S-Pol reflectivity field had a BWER (Figure 31). Maximum updraft speeds were near 30 m s^{-1} and the updraft was located in the BWER. A vorticity maximum of $10\text{-}12 \times 10^{-3} \text{ s}^{-1}$ was also present and located to the south of the updraft. Graupel echo mostly dominated the reflectivity core, with some dry hail echo detected to the south of the BWER. By 2246 UTC, the 7 km S-Pol reflectivities showed two branches of high reflectivity, with an appendage of high reflectivity on the storm's western flank (Figure 32). The maximum updraft (35 m s^{-1}) was co-located with the high reflectivity appendage. A maximum in vorticity was still located at the south end of the main updraft and was about the same magnitude to that at 2239 UTC. Dry hail echo was detected along the two branches of high reflectivity with graupel surrounding it. Two

branches of high reflectivity and hail are similar to what was described in Miller et al. (1990) as two preferential trajectories for hail. They established that the northern branch of hail came from hydrometeors ascending in the updraft and then out the “anticyclonic branch” before descending. The southern (“cyclonic”) branch of hail typically came from graupel on the western side of the updraft that was then carried cyclonically around the updraft by the streaming flow.

5.3.2 *Period D*

The period 2325-2351 UTC was the most striking intensification period in these observations. The storm began producing appreciable positive CG flash rates, became a “right-mover”, became tornadic, and contained large hail throughout a substantial volume of the storm. Additionally, maximum updraft speeds of 50 m s^{-1} were diagnosed and updraft volume increased dramatically (see section 5.2.4). Again, the large reservoir of hail echo volume aloft was centered at the 7 km level. The following discussion regarding reflectivity structure in relation to hydrometeor type and vertical velocity will highlight the radar observations at that level. Additional discussion regarding the storm split and related vorticity pattern will refer to the 5.5 km MSL level (for comparison with previous studies) and selected vertical cross sections of the data.

At 2325 UTC a BWER could be seen in the 7 km S-Pol reflectivities on the rear flank of the storm (Figure 33). A vorticity maximum of $15\text{--}20 \times 10^{-3} \text{ s}^{-1}$ was located to the southwest of the updraft and a vorticity minimum of between -5 and $-10 \times 10^{-3} \text{ s}^{-1}$ was located to the northeast of the updraft. A weaker couplet of cyclonic (positive) and anticyclonic (negative) vorticity was evident on the right rear flank as well. Both

vorticity couplets were oriented along a line in a southwest to northeast direction. The updraft maximum was near 40 m s^{-1} and was, for the most part, within the BWER. The reflectivity core was predominantly comprised of graupel at this point.

By 2331 UTC, the 7 km S-Pol reflectivities showed two branches of high reflectivity again, similar to 2246 UTC (Figure 34). A cyclonic (near $20 \times 10^{-3} \text{ s}^{-1}$) and anticyclonic vorticity couplet surrounded the main updraft. The maximum updraft at this time was located within the weak echo region (Figure 35a) and appeared well correlated with cyclonic vorticity (Figure 35b). The updraft had developed a new branch on the southwest and that branch was surrounded by the weaker vorticity couplet described in the 2325 UTC analysis, which is clearly seen in Figure 35b. Both vorticity couplets were still oriented along a southwest to northeast line. A vertical cross section of vorticity (in Figure 35c) illustrates the vertical extent of the cyclonic vorticity that spawned the F1 tornado 3 minutes prior to this synthesis. Low-level vorticity production was dominated by the stretching term of the local vorticity tendency equation (Figure 36). This has also been documented in previous numerical and observational studies (Ray, 1976; Bluestein and Sohl, 1979; Brandes, 1978; Rotunno, 1981). Tilting of horizontal vorticity into the vertical, in addition to stretching, was responsible for the vorticity production between 4-6 km. Some dry hail echo was now detected at this level in the reflectivity core (Figure 34c). Graupel echo coverage was considerable at this time as well and extended along the two branches of high reflectivity. The maximum updraft speed persisted near 40 m s^{-1} .

The 7 km S-Pol reflectivities at 2338 UTC showed very high reflectivities ($> 60 \text{ dBZ}$) with the BWER starting to reappear (Figure 37). The updraft was now strongest on

its southwestern branch (rather than its northeastern branch as in the previous synthesis). Each branch of the updraft was still surrounded by a cyclonic and anticyclonic vorticity couplet. Each vorticity couplet had become stronger by this time. Dry hail echo was now dominating a larger area of the storm at this level.

The BWER in S-Pol reflectivity was bounded by very high reflectivities (between 60-70 dBZ) by 2343 UTC (Figure 38). The two branches of the updraft had completely split at this time, leaving the southwestern branch (i.e. the right-moving cell) as the dominant updraft (Figure 38d). Each updraft had its own associated vorticity couplet, with cyclonic vorticity co-located with the new maximum updraft (Figure 39b). This pattern of vertical vorticity in a splitting storm has been documented in simulations by Finley et al. (2001). The correlation of cyclonic vorticity with the updraft is a common attribute of supercells (Weisman and Klemp, 1984). In addition, Rotunno (1981) stated that a vortex pair followed each updraft/downdraft pair when a storm split. An updraft/downdraft pair was not observed, however, likely because the downdrafts were poorly resolved in this synthesis. Ray (1976) acknowledged that divergence in a shallow layer near the surface, such as that induced by a downdraft, may be poorly sampled or undetected by radar. This is indeed a likely reason for the lack of downdrafts detected in this synthesis, since the storm was approximately 80 km from at least one of the radars used in the synthesis at any given time during the analysis period, inhibiting the detection of low-level features. Negative (positive) vorticity dominating the low-levels of the “left-mover” (“right-mover”) can be seen in a vertical cross section of vorticity (Figure 39c); the complete separation of the two updrafts is also evident. Rotunno (1981) documented this low-level vorticity feature of splitting storms from his simulations, as was also

recognized by Wilhelmson and Klemp (1978). Again, stretching was most responsible for the vorticity production in the lowest kilometer of the storm (Figure 40), however tilting was dominant just above that near 4 km. Dry hail echo was detected surrounding the BWER, with some wet hail being detected on the western edge of the BWER (Figure 38c). The dominant updraft was located within the BWER (Figure 39a). High reflectivity branched off to the northeast in association with the updraft on the north flank of the storm (i.e. the left-moving cell).

Following that, at 2351 UTC, S-Pol reflectivities showed that the BWER was larger in area and still was bounded by high reflectivities (Figure 41). The northern branch of high reflectivity had weakened. The vorticity couplet and associated updraft on the north flank of the storm had also weakened considerably. Thus, the left-mover from the storm split diminished before it was distinguishable as a separate cell in the reflectivity field. The new dominant updraft was still very strong (up to 40 m s^{-1}) and was within the BWER. Dry hail echo had filled in the BWER and wet hail was still detected on the west edge of the BWER at this level.

5.3.3 *Period F*

A peak in the positive CG flash rate occurred near 0036 UTC. The period leading to that (0023-0030 UTC) had a small maximum in hail echo volume aloft as discussed in section 5.2.6. The hail echo maximum was centered more at the 6.5 km level at this time, yet the 6.5 km observations were similar to those at 7 km and for comparison with the previous discussion, a closer examination of the radar observations at the 7 km level will follow.

The 7 km S-Pol reflectivities at 0023 UTC had a BWER on the rear flank of the storm (Figure 42). A new cell had developed northwest of the storm. The main storm's updraft was associated with the observed BWER. Some dry hail echo was detected at this level on north edge of the BWER and in the new cell also. Cyclonic vorticity was detected south of main cell's updraft, but was marginal.

By 0030 UTC, S-Pol reflectivities showed the BWER persisting and the new cell was still growing to the northwest (Figure 43). The updraft was still inside the BWER and was as strong as 40 m s^{-1} . Vorticity had increased to near $15 \times 10^{-3} \text{ s}^{-1}$ south of the updraft. Dry hail echo was detected within the core of the reflectivity at this level. Graupel was distributed surrounding the core of reflectivity and outward from the core along two branches oriented to the northeast and southeast, similar to observations at 2246 and 2331 UTC.

At 0036 UTC, a less organized pattern within the main cell was seen in the S-Pol reflectivities at 7 km, however, the new cell to the north persisted (Figure 44). Some sort of appendage of high reflectivity was evident to the west of the main core of high reflectivity. Two areas of cyclonic vorticity (near $15 \times 10^{-3} \text{ s}^{-1}$) were detected on either side of the updraft. Less dry hail echo was detected at this level compared to the last volume, but it was still detected in the reflectivity core.

5.3.4 *Period G*

A maximum in hail echo volume occurred at 0049 UTC and was centered around 7 km MSL. The following discussion highlights the observations at 7 km for the period 0043-0049 UTC leading to this maximum in hail echo volume aloft.

At 0043 UTC a BWER was observed as was noted in section 5.2.7 (Figure 29). This BWER was also visible in the reflectivity field in Figure 45 at the 7 km level and an updraft near 20 m s^{-1} was located near the BWER. Two areas of cyclonic vorticity were still present (see section 5.3.3); however, the vorticity to the southwest of the updraft had weakened, while the other region of vorticity was now greater than $15 \times 10^{-3} \text{ s}^{-1}$. Two branches of higher reflectivity were also detected, again similar to what was observed in previous sections. Graupel echo was present in the two branches as well. Dry hail echo was dominant in the high reflectivity core.

A large region of high reflectivity dominated the core of the cell still by 0049 UTC (Figure 46). The maximum updraft still resided near 20 m s^{-1} and was located on the south side of the core. The cyclonic vorticity to the northeast of the updraft was still strong, although decreasing in horizontal extent. The core was still dominated by hail echo, yet some wet hail echo signatures were detected in the center of the core by this time.

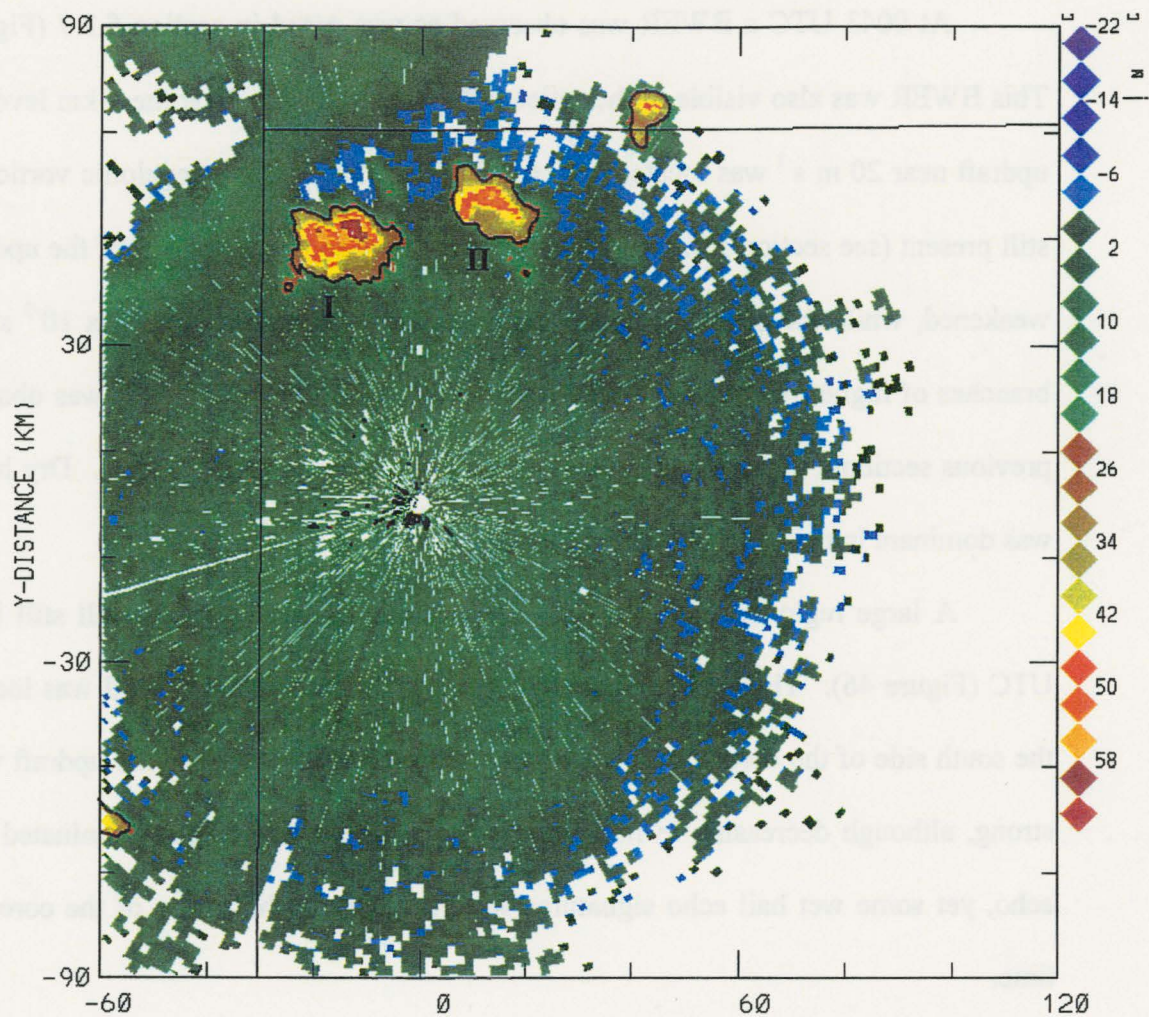


Figure 15. 2215 UTC base reflectivity from KGLD (0,0) indicating a surface boundary (thin line radar echo) behind (northwest) Storm I. Storm II is an earlier storm (see Section 5.1). The 25 dBZ contour is in black. Storm I is located near $(x,y) = (-20, 50)$ and Storm II is located near $(x,y) = (10, 55)$.

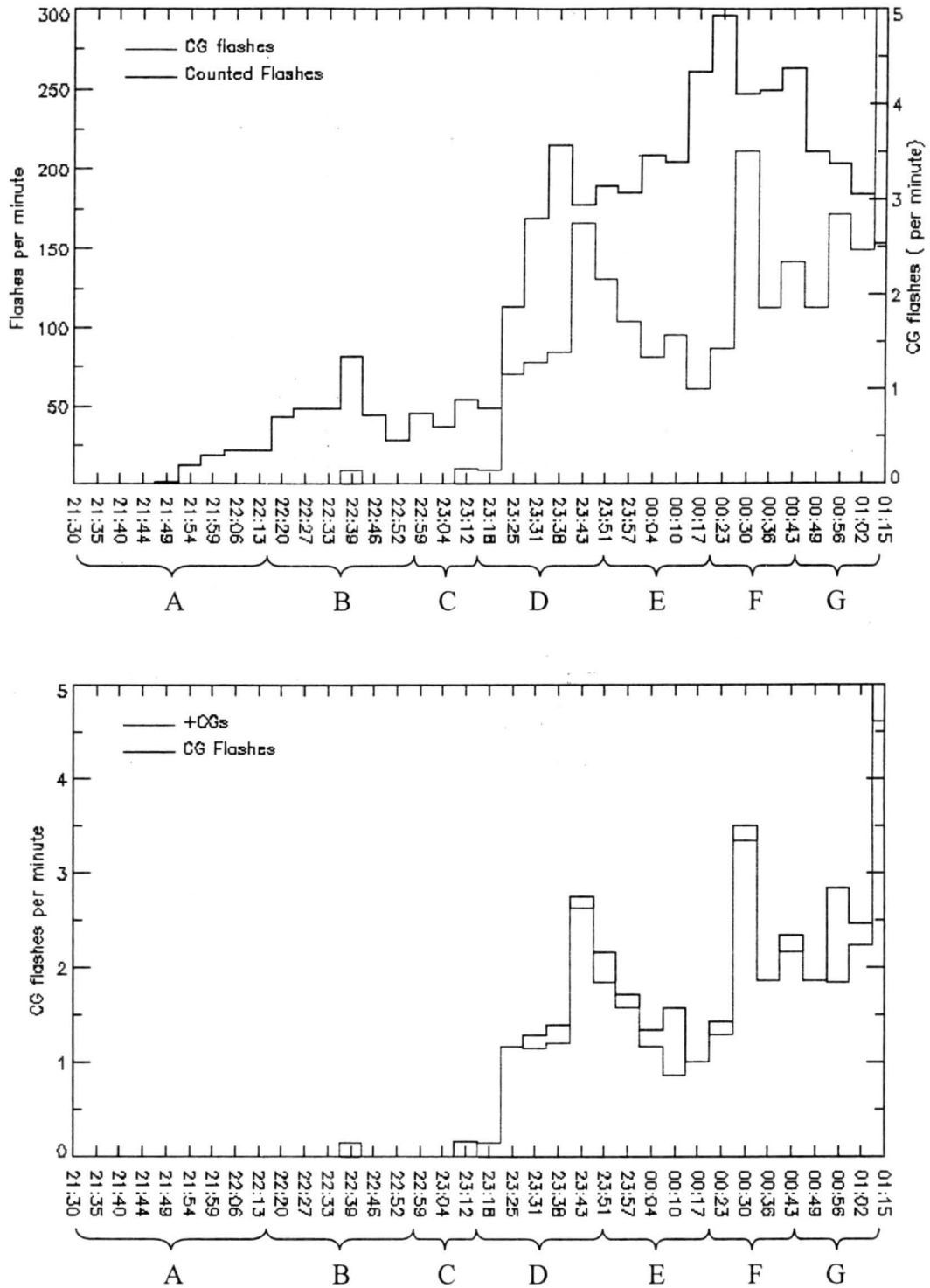


Figure 16. Time series of total flash rate (IC + CG) and total CG activity (top panel) and total CG activity with only positive CG activity overlaid (bottom panel). Shorter time periods have been defined (labeled A, B, C...) to reference updraft volume pulses and phases in the overall evolution of the storm.

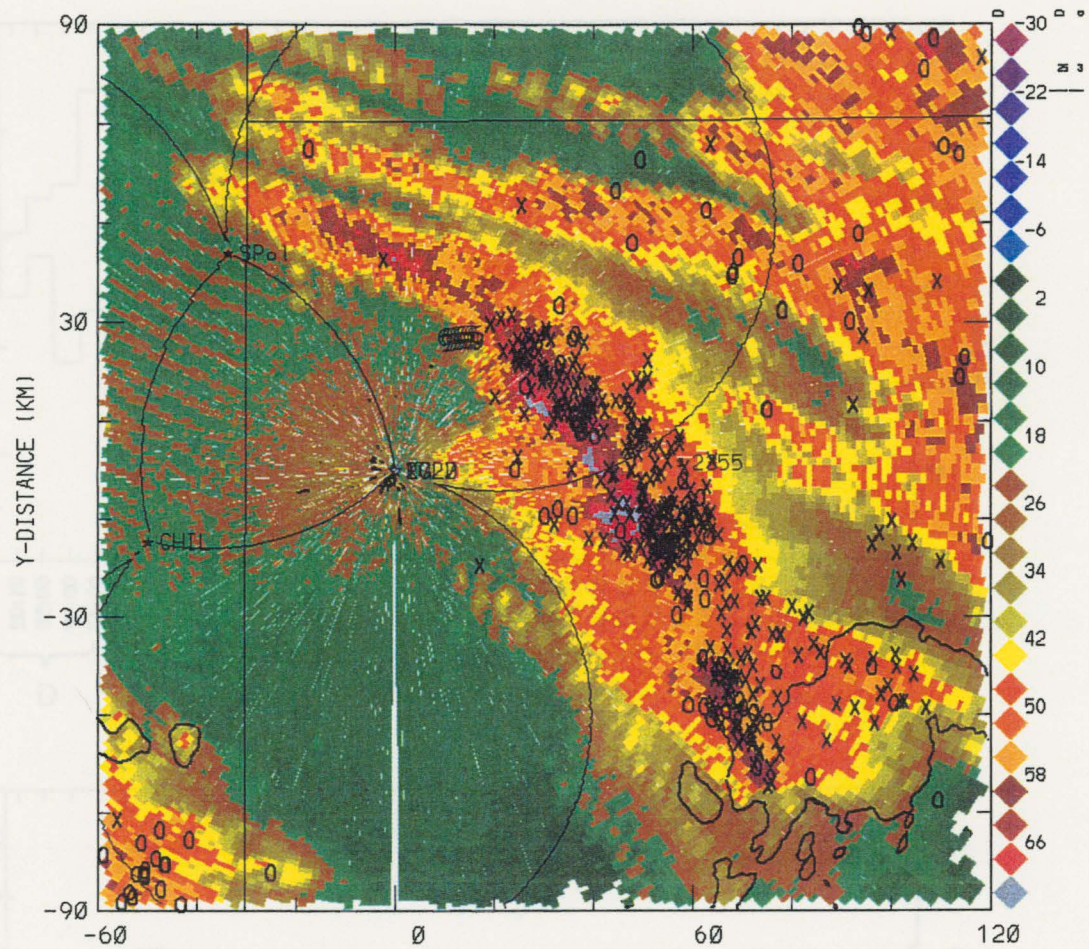


Figure 17. Swath of base reflectivities from KGLD (0,0) for the period 2100-0251 UTC with NLDN lightning data overlaid (x = positive CG, o = negative CG). 25 dBZ is contoured as in Figure 15.

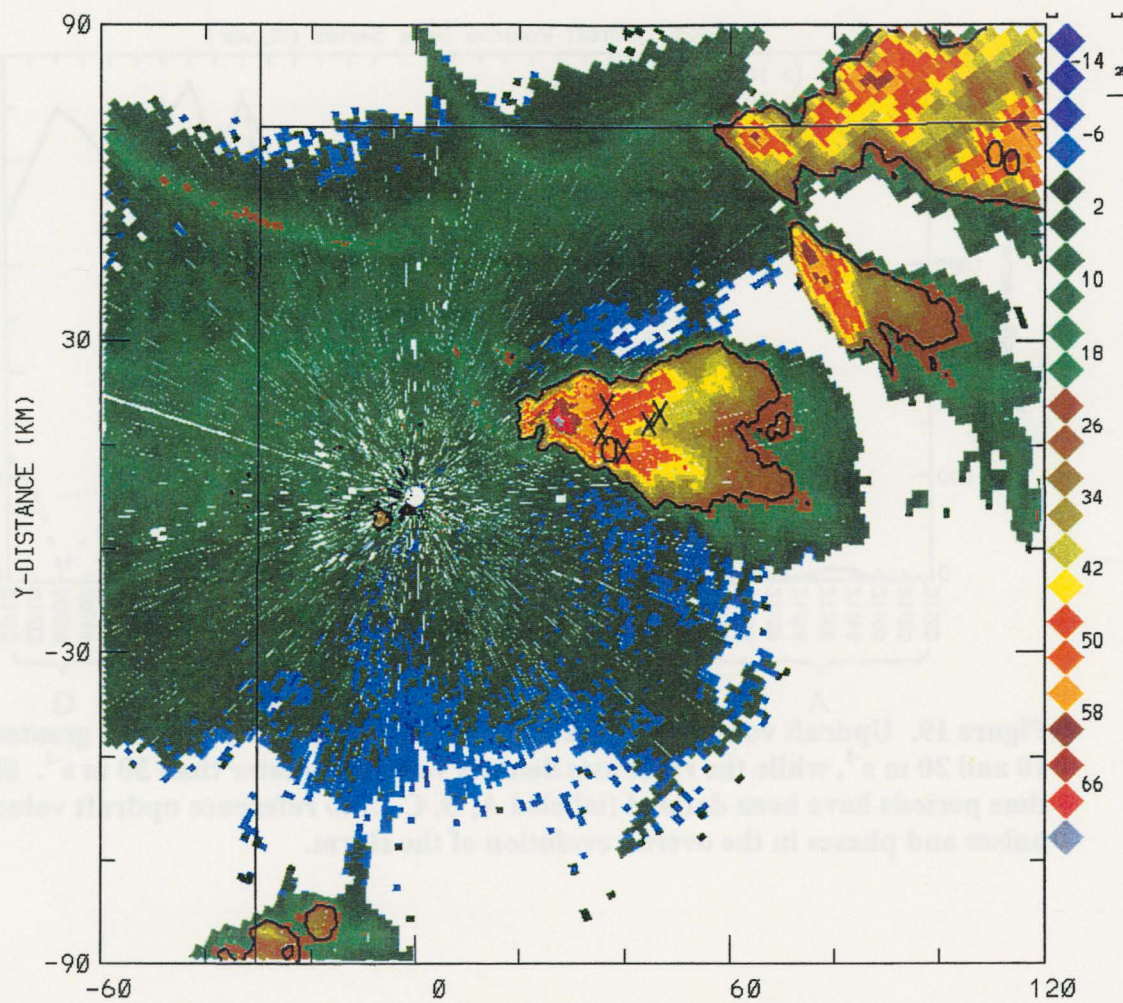


Figure 18. 0004 UTC base reflectivities from KGLD (0,0) indicating a thin line echo is present. NLDN data is overlaid as in Figure 17. 25 dBZ is contoured as in Figure 15.

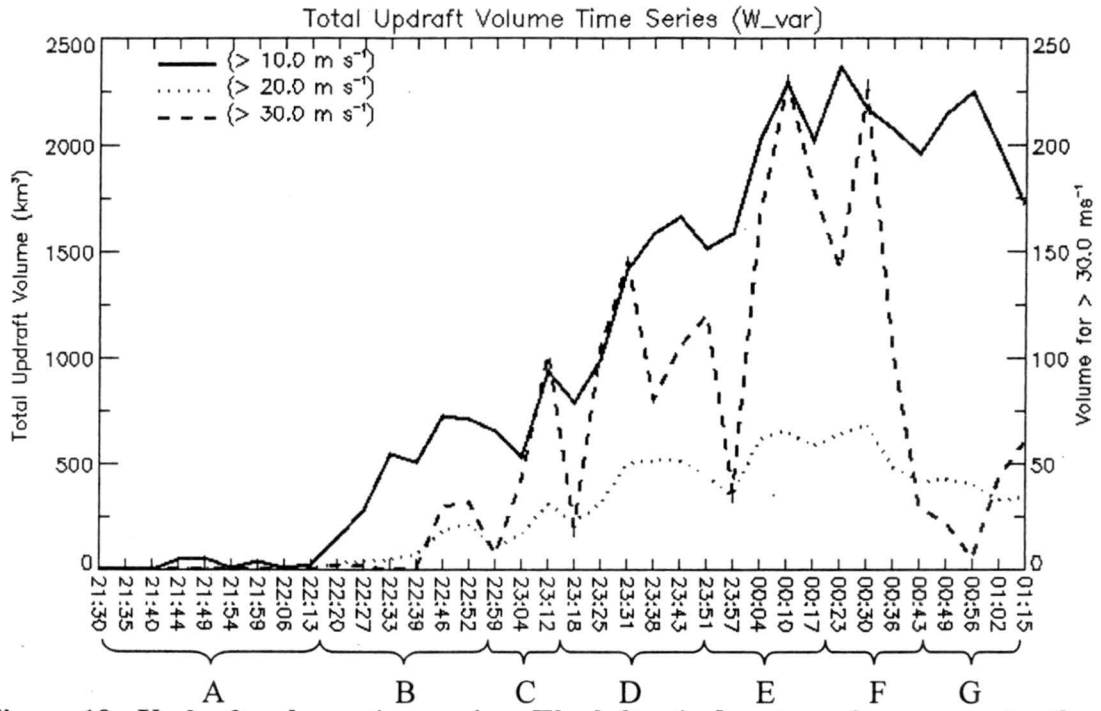


Figure 19. Updraft volume time series. The left axis denotes volumes greater than 10 and 20 m s^{-1} , while the right axis denotes volumes greater than 30 m s^{-1} . Shorter time periods have been defined (labeled A, B, C...) to reference updraft volume pulses and phases in the overall evolution of the storm.

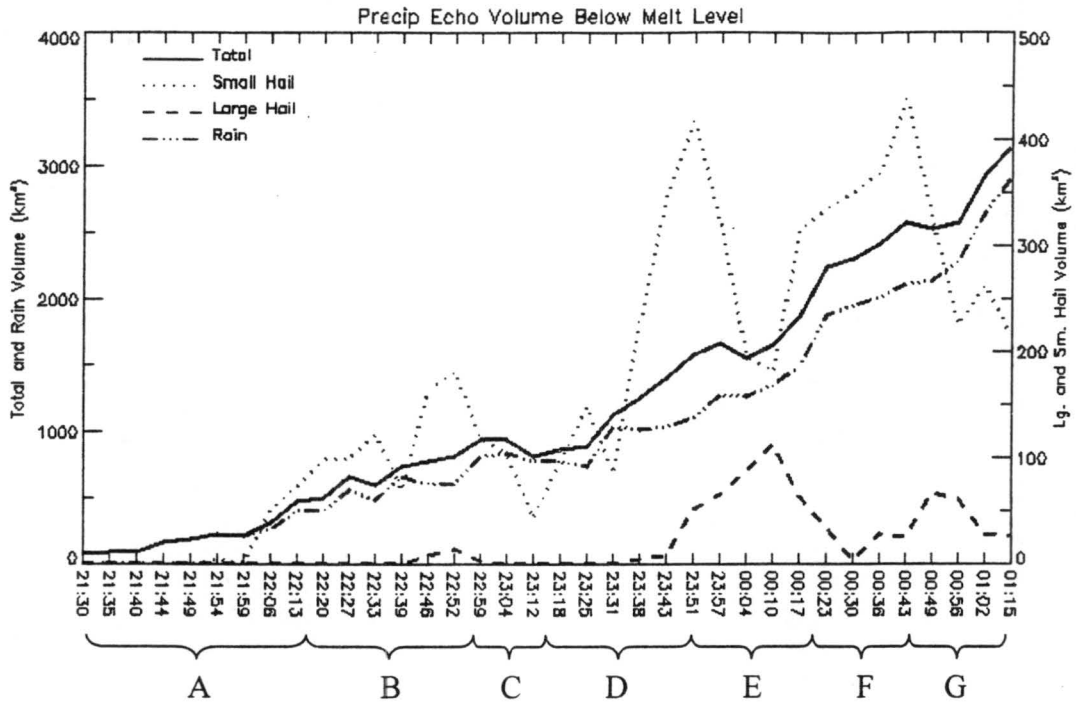


Figure 20. Precipitation echo volumes below the melting level. The left axis denotes total precipitation and rain echo volumes and the right axis denotes small and large hail echo volumes.

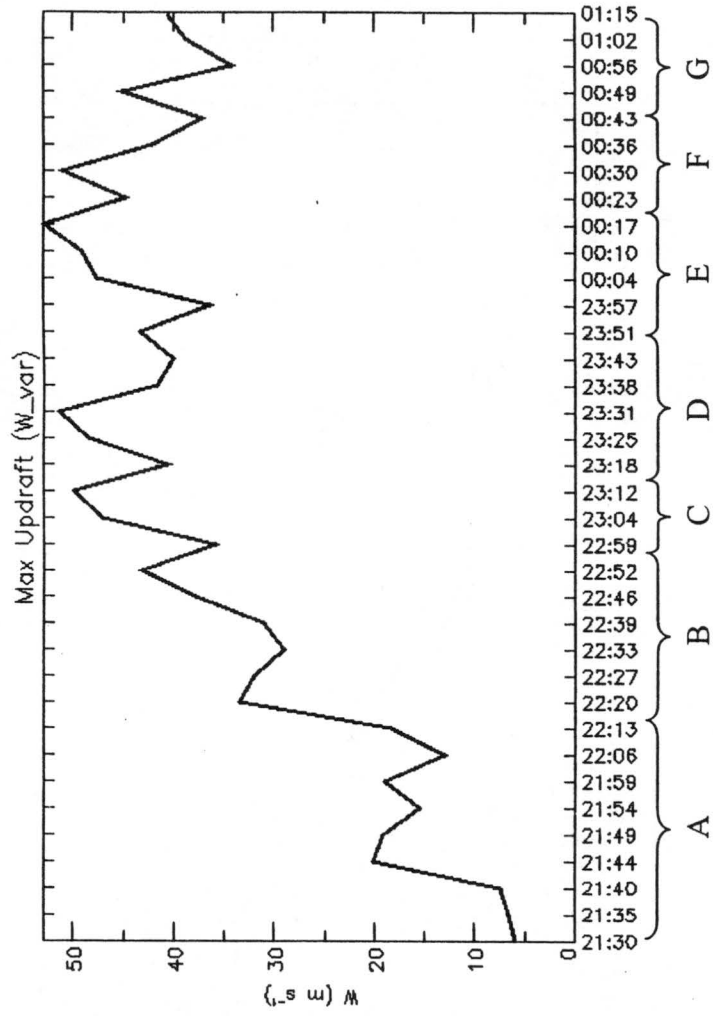


Figure 21. Maximum updraft time series.

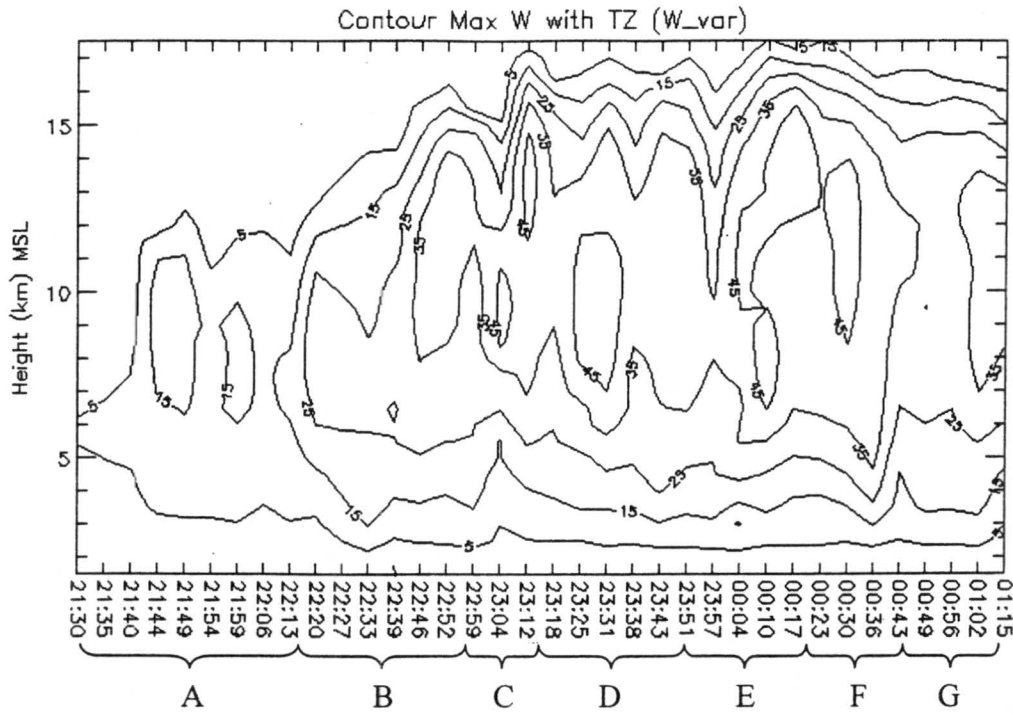


Figure 22. Time-height cross section of the maximum updraft contoured at 10 m s^{-1} intervals.

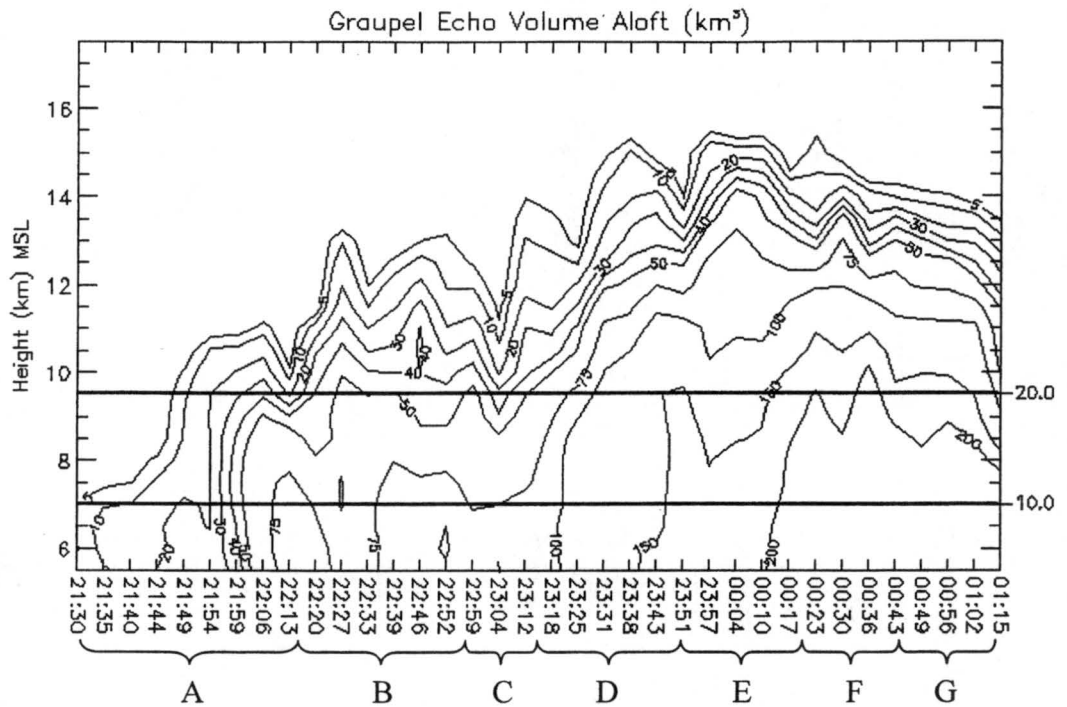


Figure 23. Graupel echo volume above the melting level at each time and height. Isotherms for -10°C and -20°C are overlaid for reference.

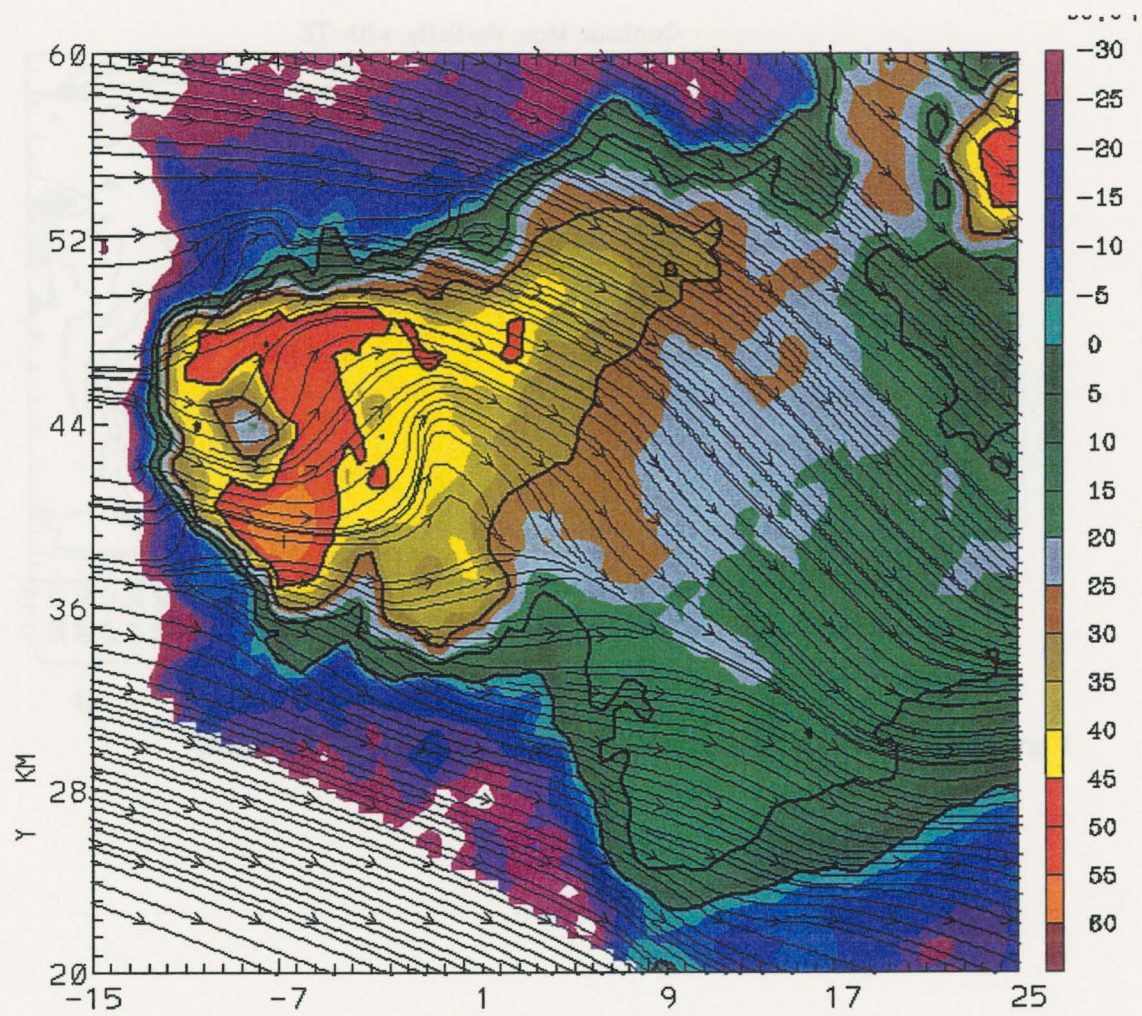


Figure 24. 2239 UTC 8 km synthesis with storm relative streamlines overlaid on S-Pol reflectivity.

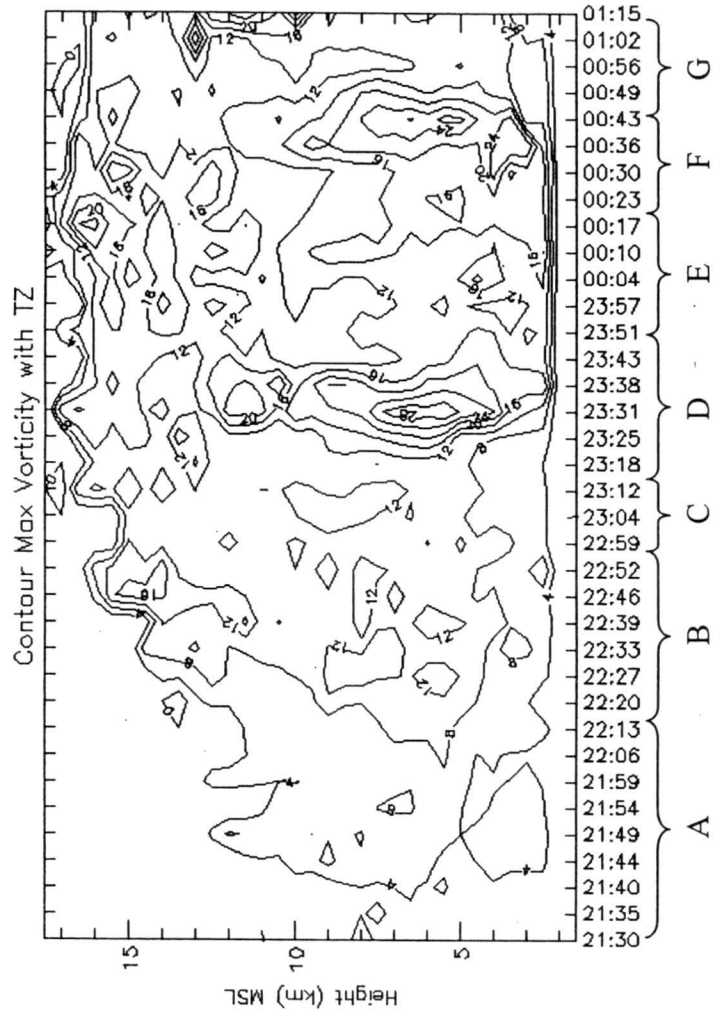


Figure 25. Maximum vorticity (10^{-3} s^{-1}) at each time and height.

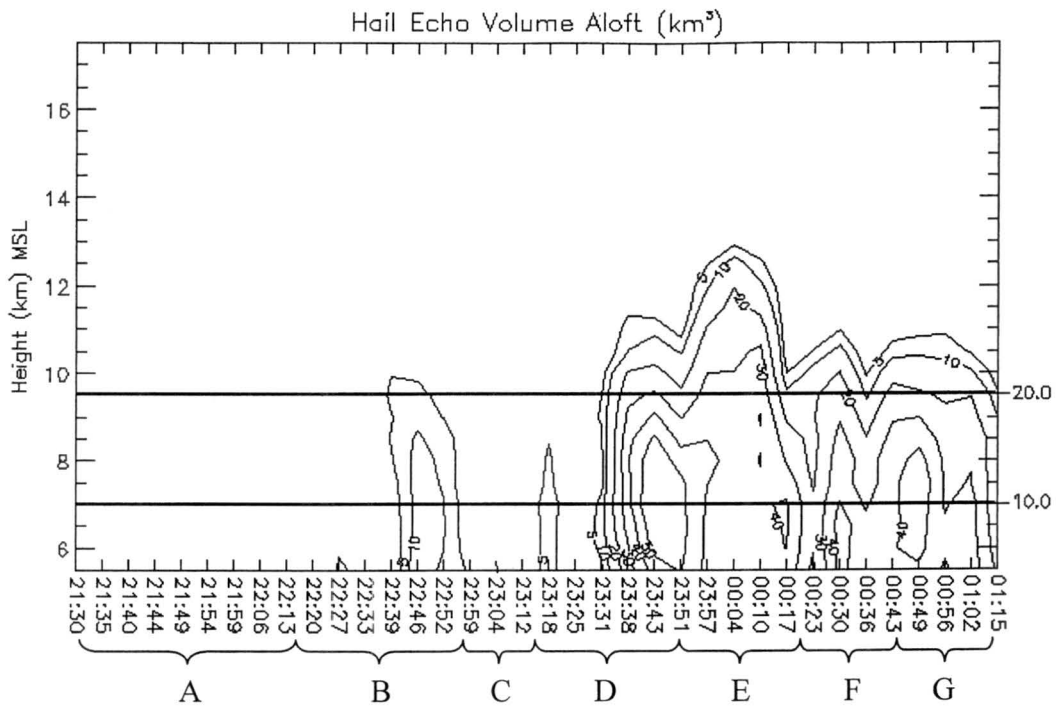


Figure 26. Hail echo volume above the melting level at each time and height. Isotherms for -10°C and -20°C are overlaid for reference.

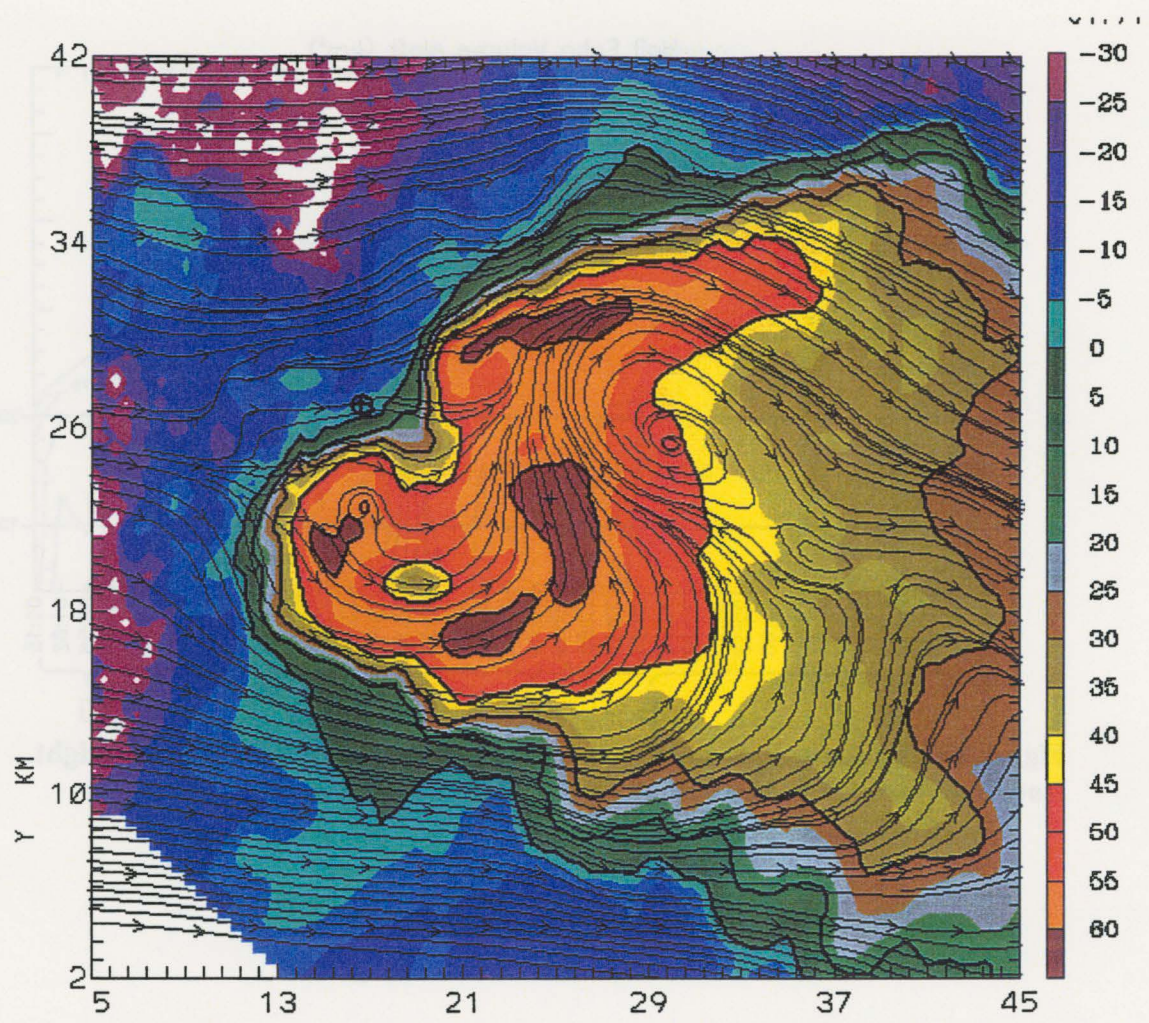


Figure 27. 2343 UTC 6 km synthesis with storm relative streamlines overlaid on S-Pol reflectivity.

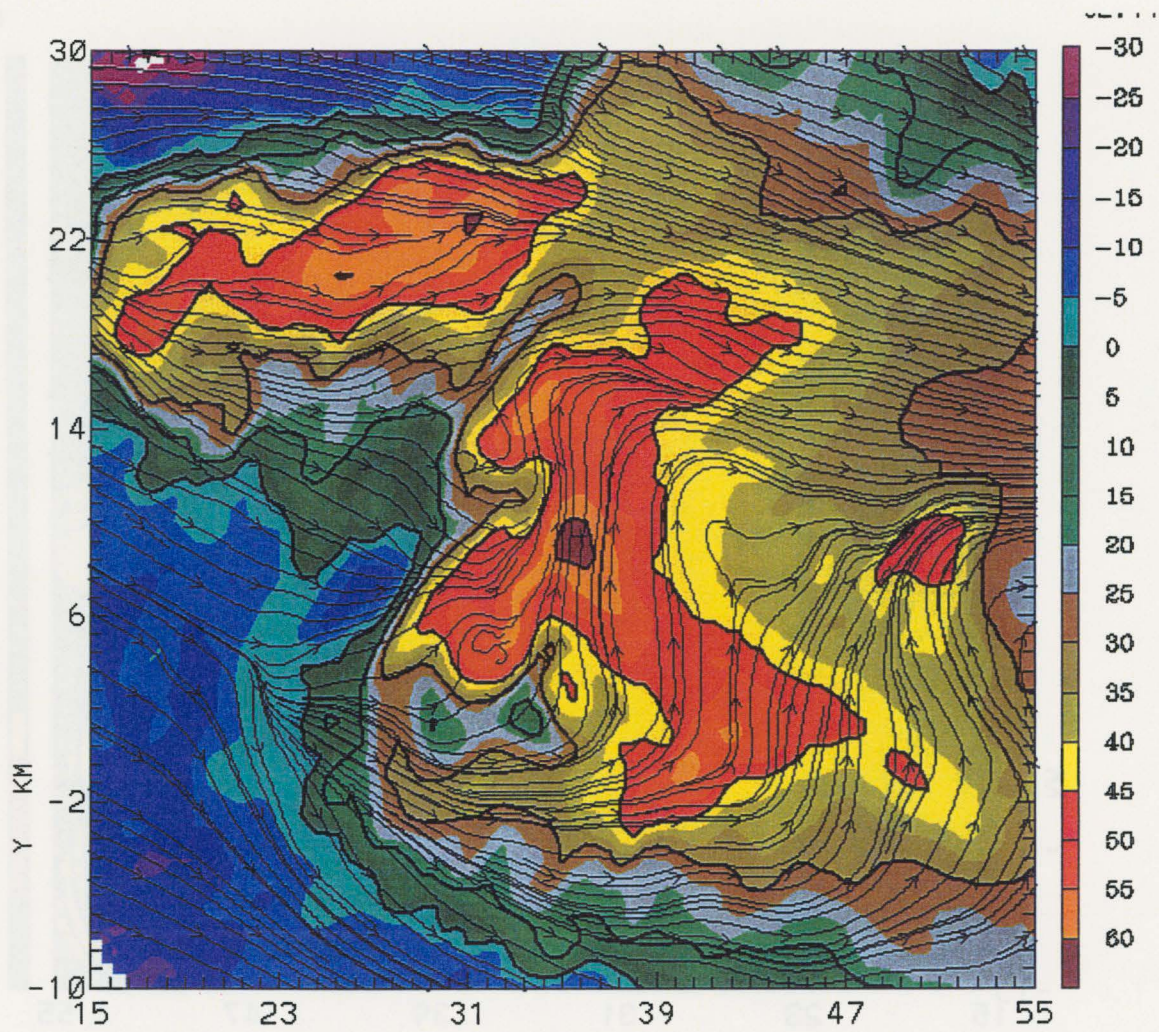


Figure 28. 0023 UTC 6 km synthesis with storm relative streamlines overlaid on S-Pol reflectivity.

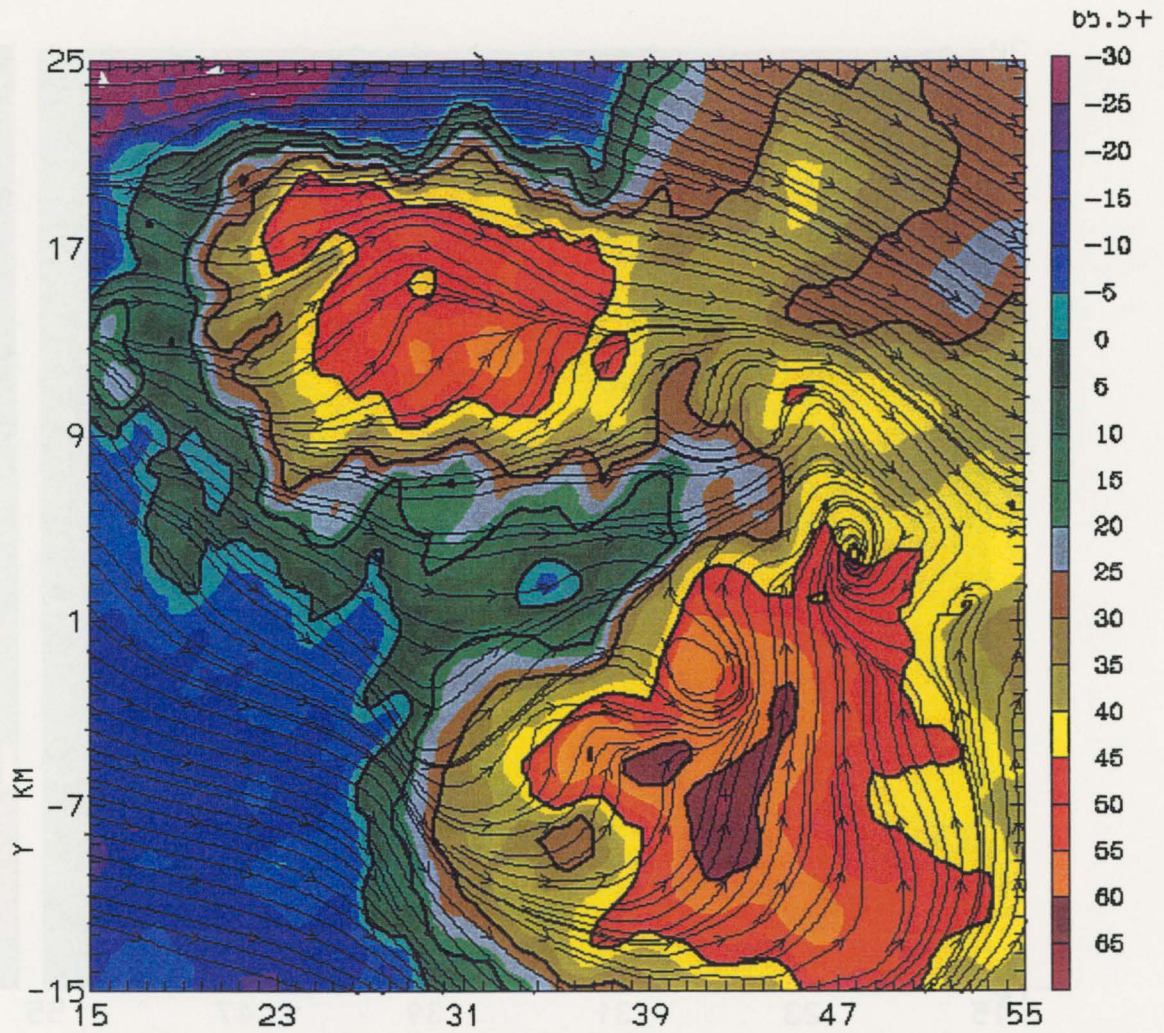


Figure 29. 0043 UTC 6 km synthesis with storm relative streamlines overlaid on S-Pol reflectivity.

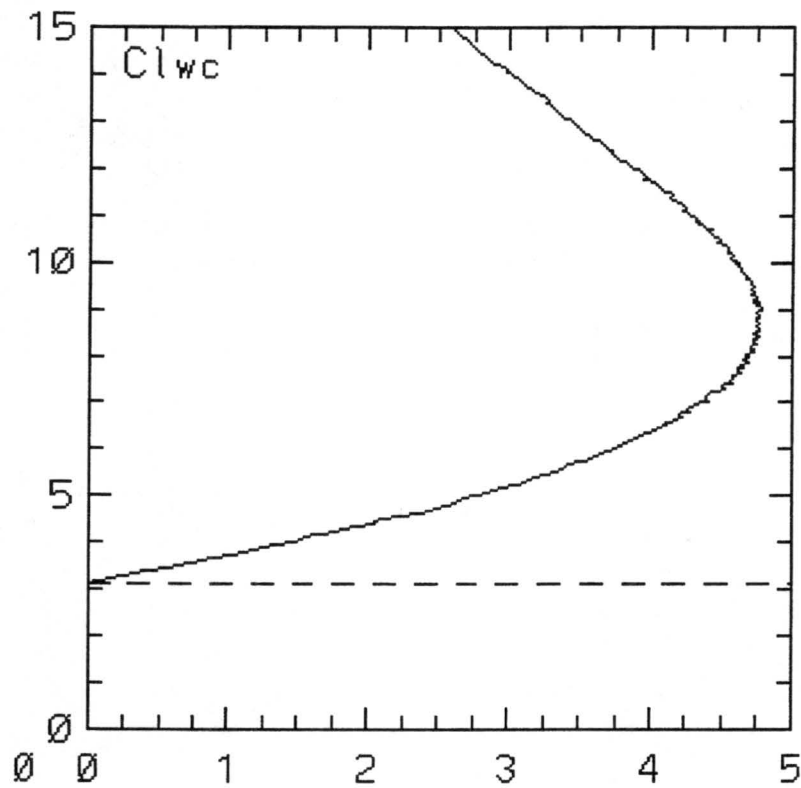
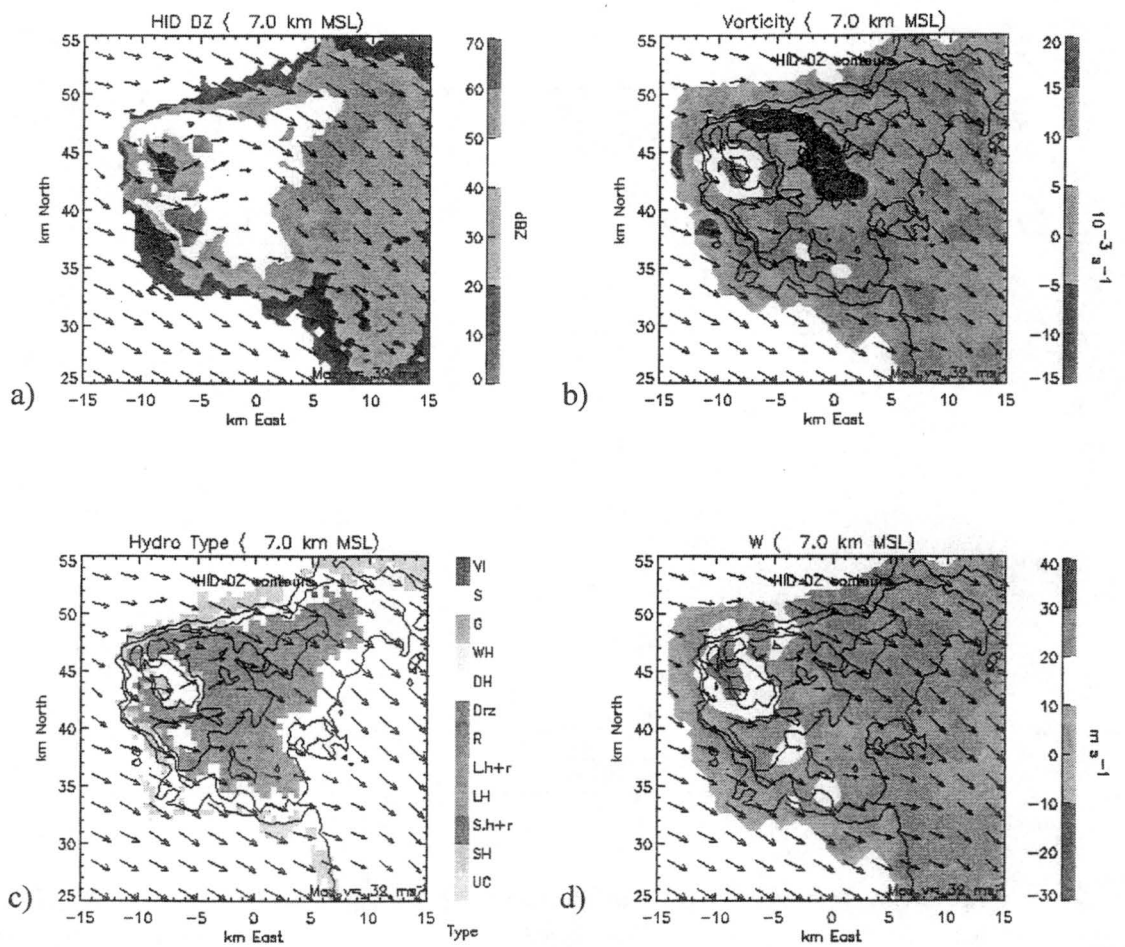
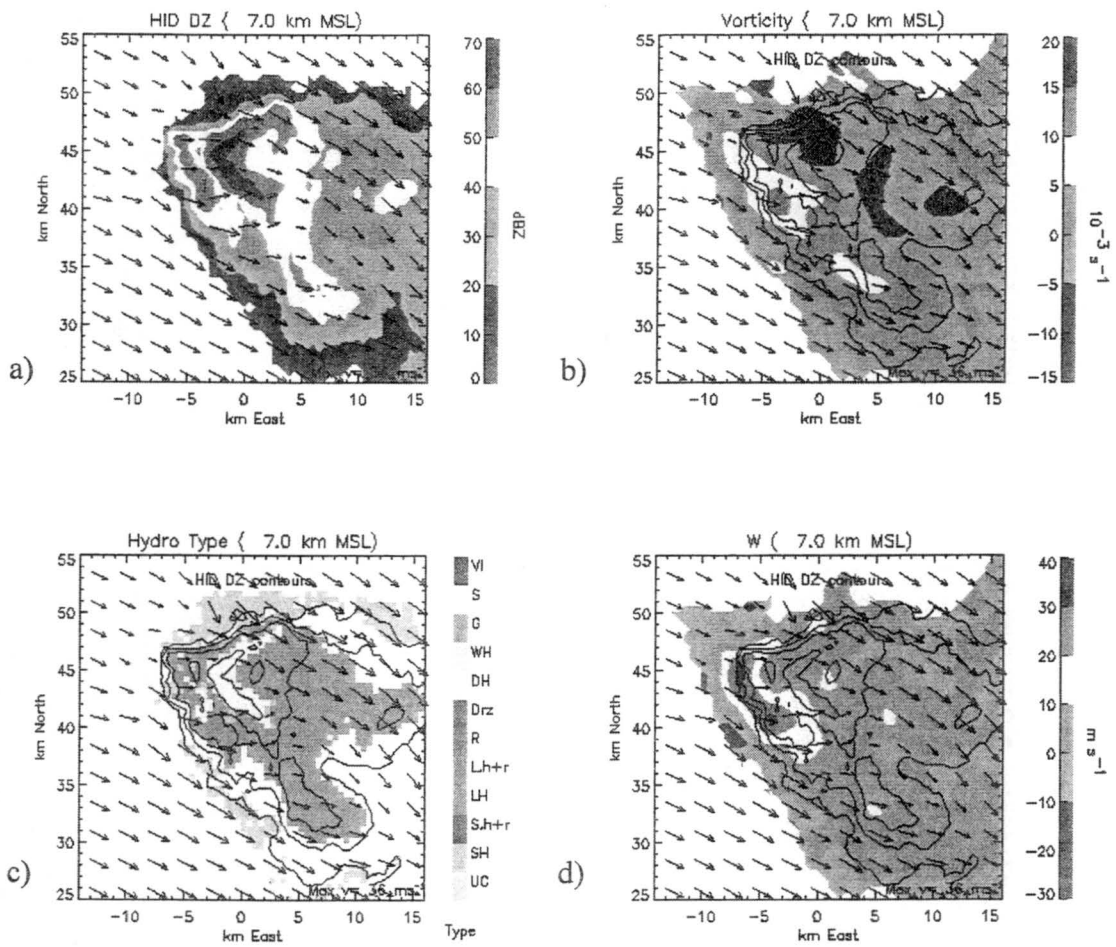


Figure 30. A height profile of cloud liquid water content from the MGLASS sounding at 2022 UTC at Goodland, Kansas. The ordinate axis is height (km MSL) and the abscissa is cloud liquid water content (g m^{-3}).



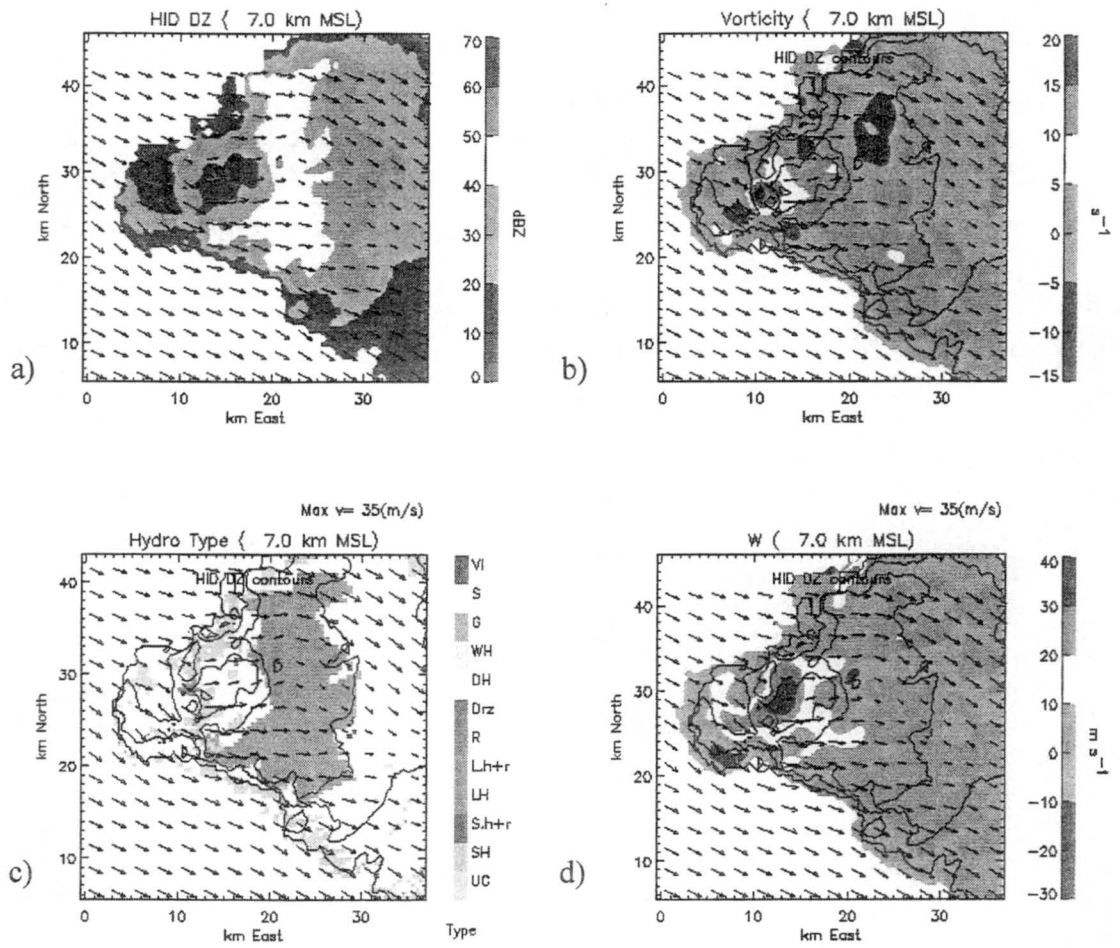
SPOL Date: 06/29/00, Time: 22:39

Figure 31. 2239 UTC synthesis at 7 km showing (a) S-Pol reflectivity, (b) vertical vorticity, (c) Hydrometeor type, and (d) vertical velocity. Ground-relative wind vectors are overlaid in black. Contours of S-Pol reflectivity are overlaid in black on (b), (c), and (d) for reference. Contour interval is 15 dBz.



SPOL Date: 06/29/00, Time: 22:46

Figure 32. Same as Figure 31 except for 2246 UTC.



SPQI Date: 06/29/00, Time: 23:25

Max $v = 35(m/s)$

Figure 33. Same as Figure 31 except for 2325 UTC.

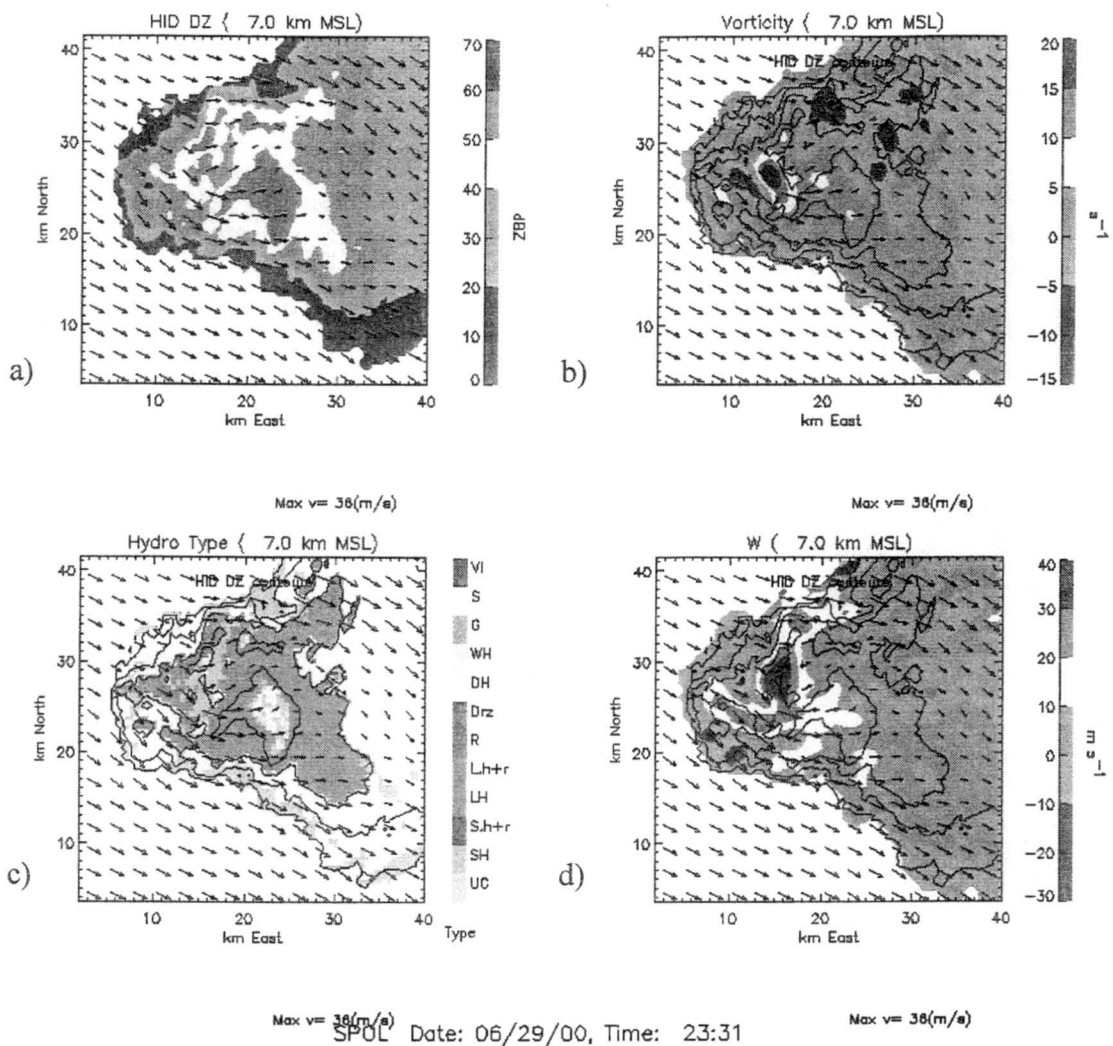
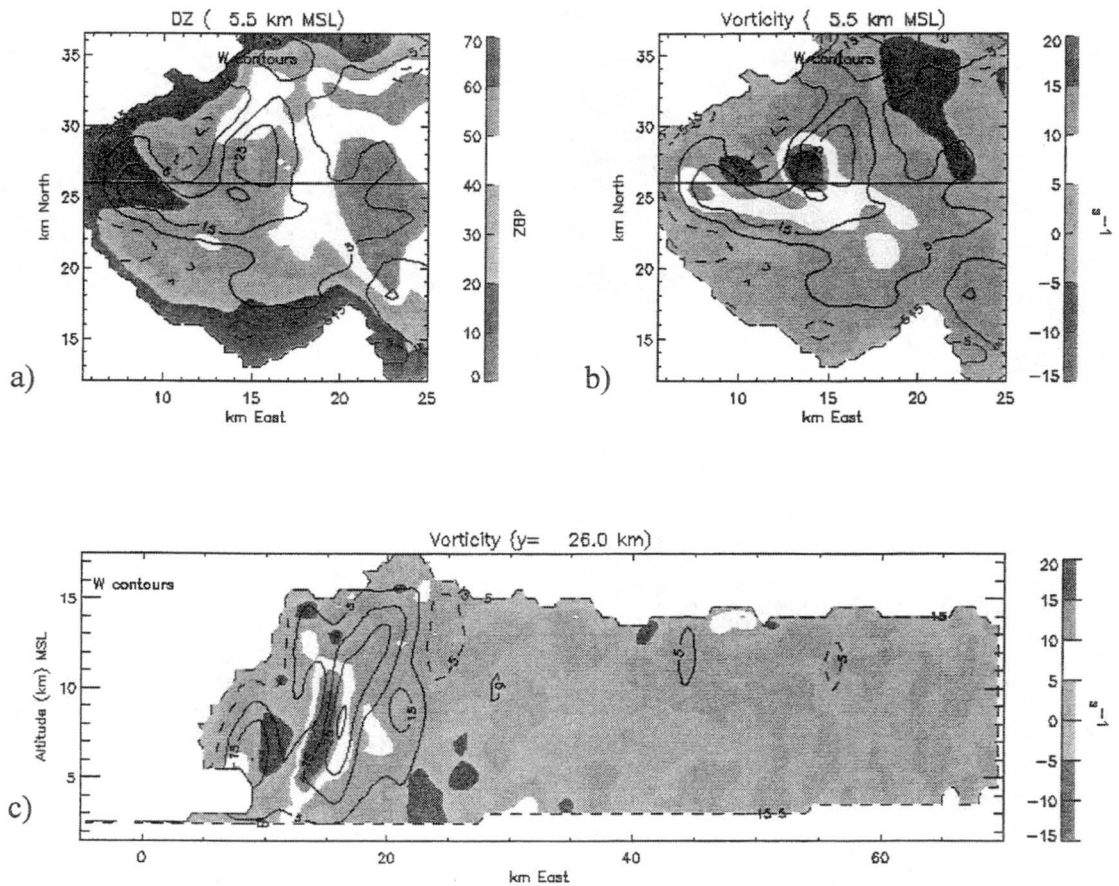


Figure 34. Same as Figure 31 except for 2331 UTC.



Date: 06/29/00, Time: 23:31

Figure 35. 2331 UTC synthesis at 5.5 km showing (a) S-Pol reflectivity, (b) vertical vorticity, and a vertical cross section at y = 26.0 km with ground-relative wind vectors are overlaid in black in (c). Positive vertical velocities are overlaid as solid black contours, and negative vertical velocities are dashed black contours. Contour interval is 10 m s⁻¹.

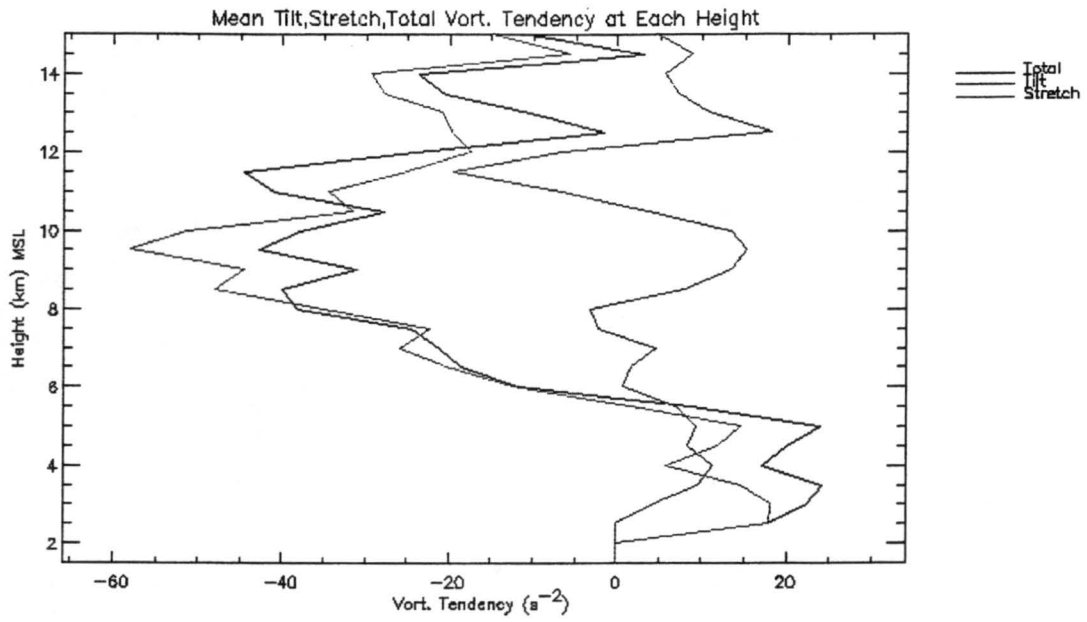
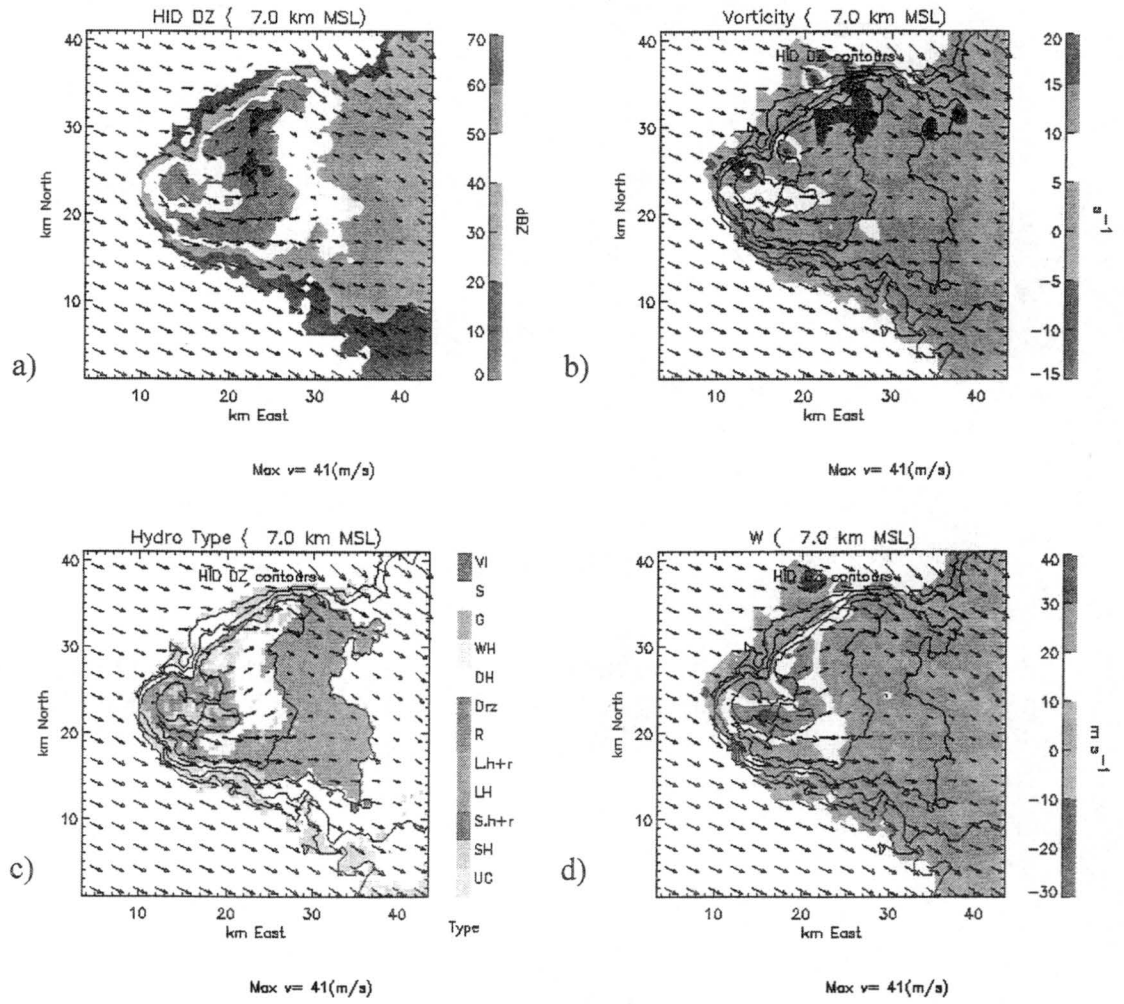


Figure 36. Vertical profile of the mean tilting (red) and stretching (green) terms of the local vorticity tendency (black) at 2331 UTC for the (x,y) domain illustrated in Figure 35 (a) and (b).



SPOL Date: 06/29/00, Time: 23:38

Figure 37. Same as Figure 31 except for 2338 UTC.

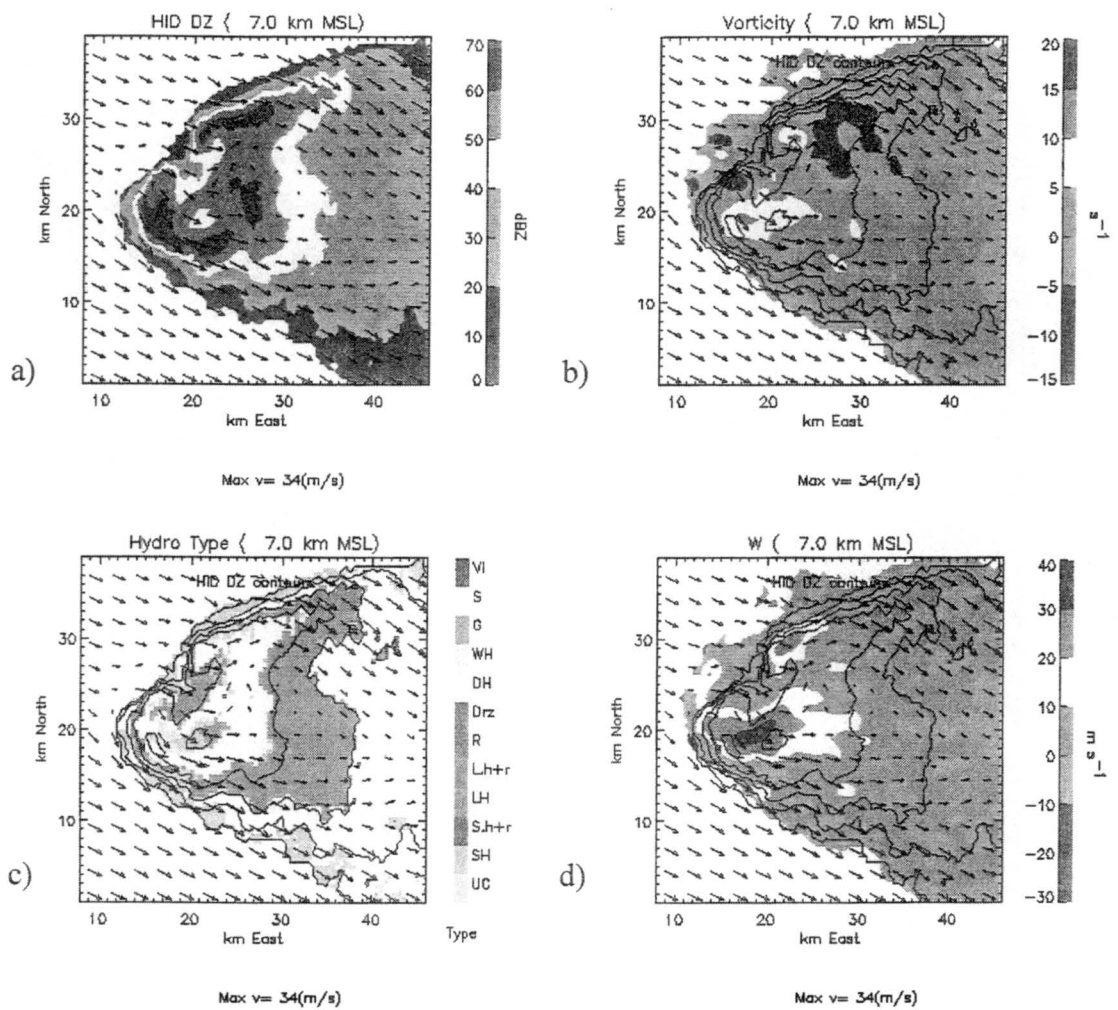
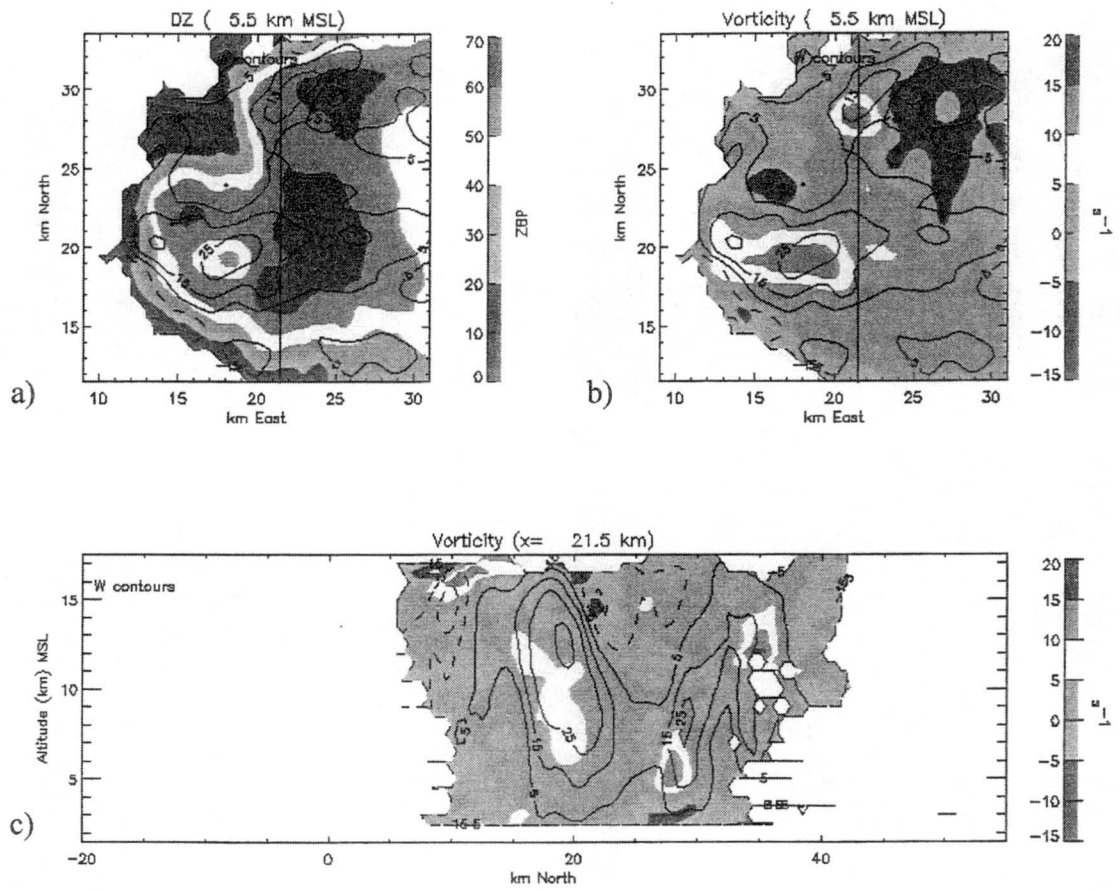


Figure 38. Same as Figure 31 except for 2343 UTC.



Date: 06/29/00, Time: 23:43

Figure 39. Same as Figure 35 except for 2343 UTC and the vertical cross section is $x = 21.5$ km.

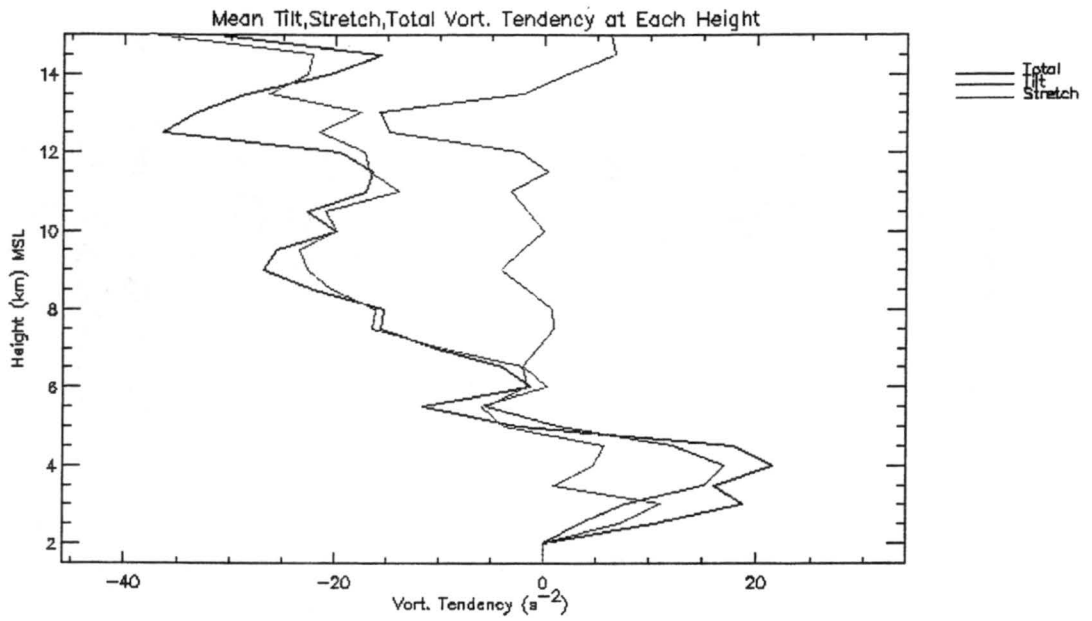
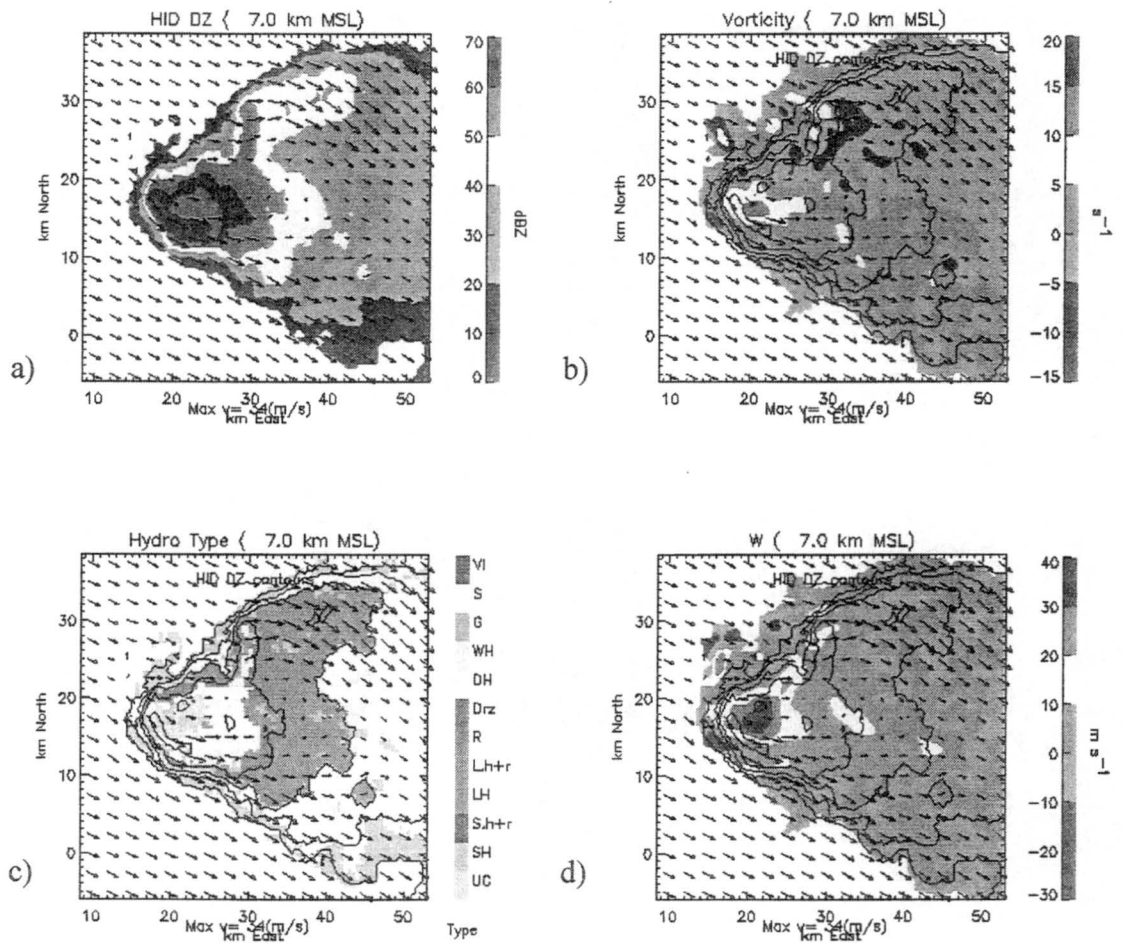
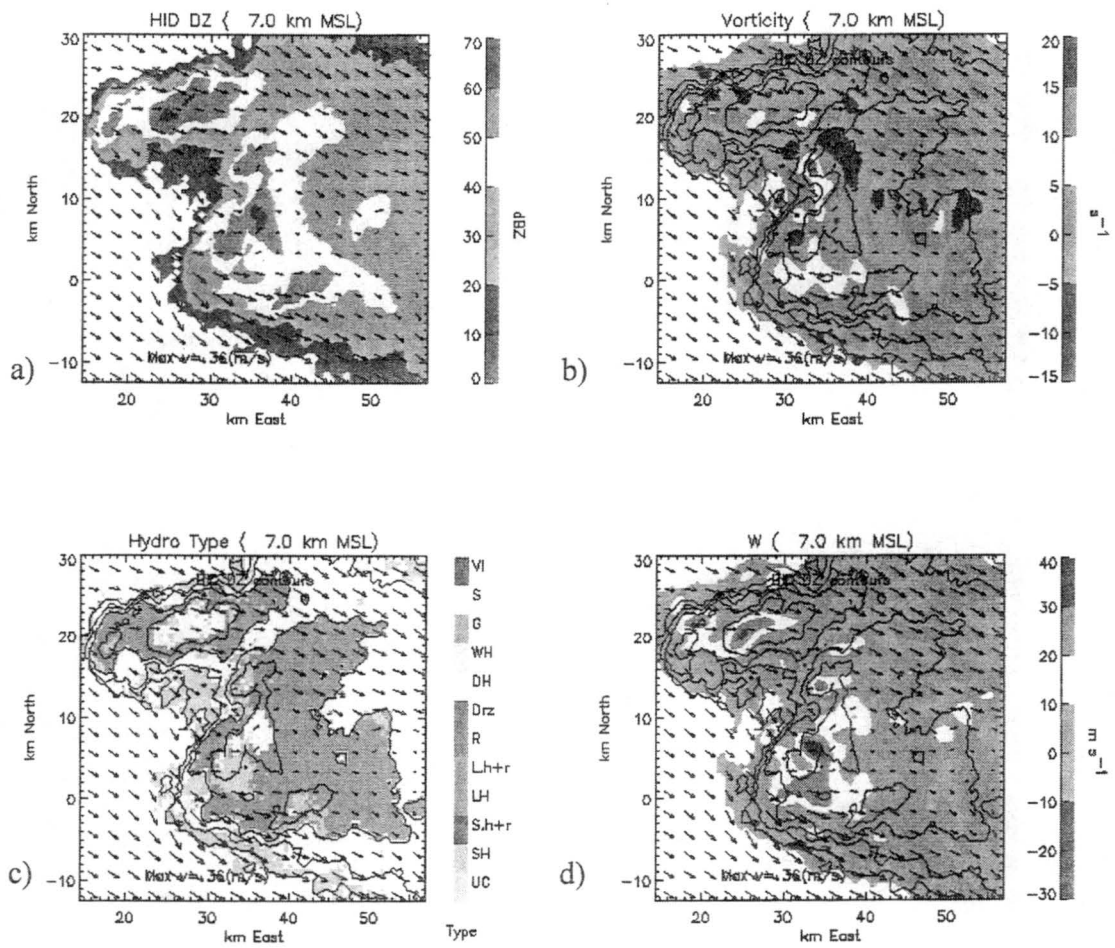


Figure 40. Vertical profile of the mean tilting (red) and stretching (green) terms of the local vorticity tendency (black) at 2343 UTC for the (x,y) domain illustrated in Figure 39 (a) and (b).



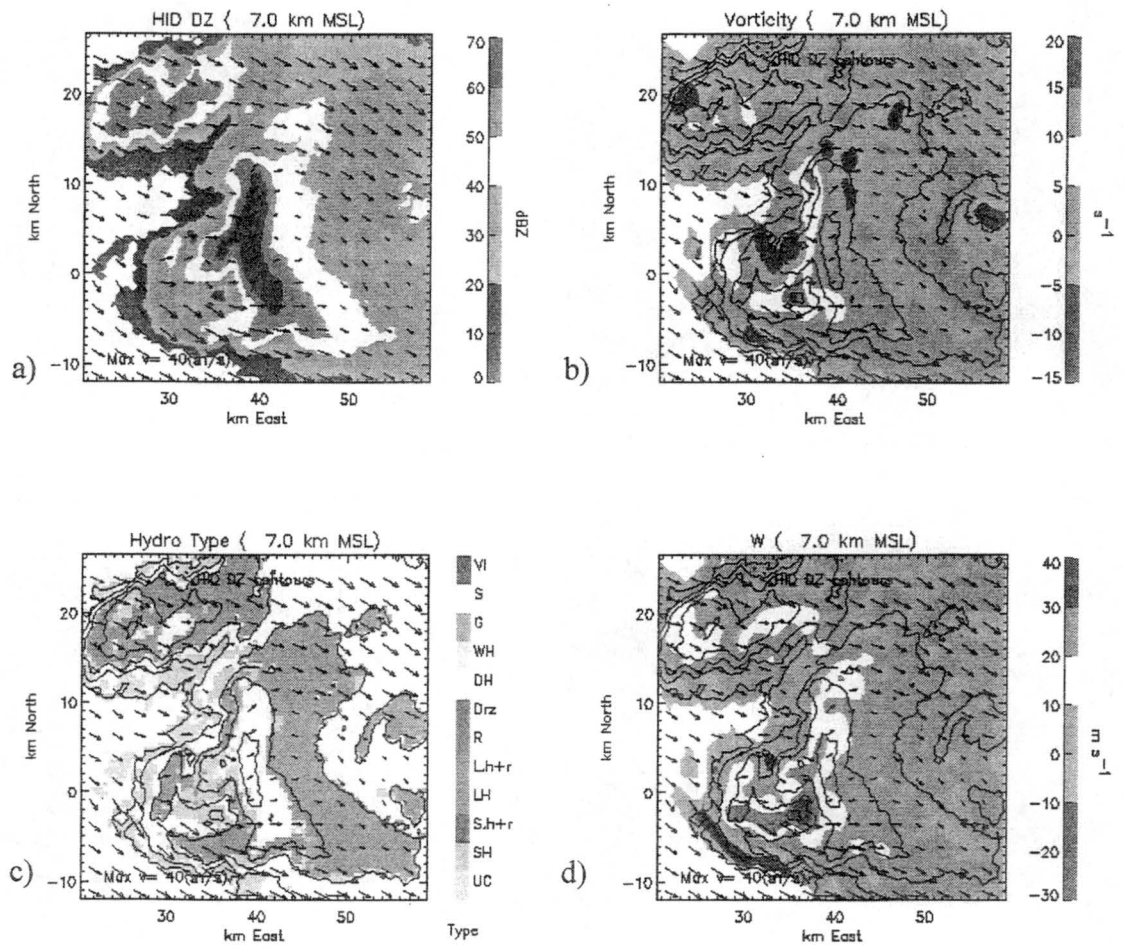
SPOL Date: 06/29/00, Time: 23:51

Figure 41. Same as Figure 31 except for 2351 UTC.



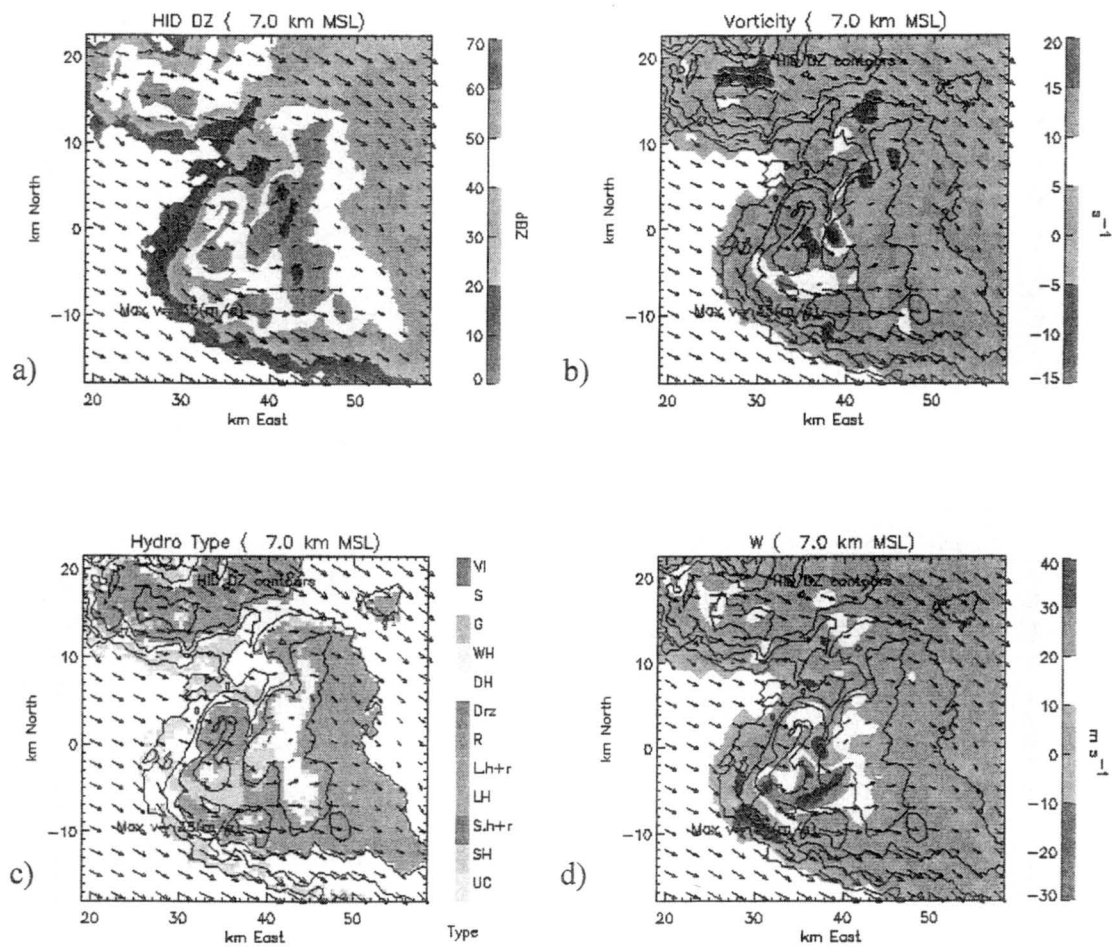
SPOL Date: 06/30/00, Time: 00:23

Figure 42. Same as Figure 31 except for 0023 UTC.



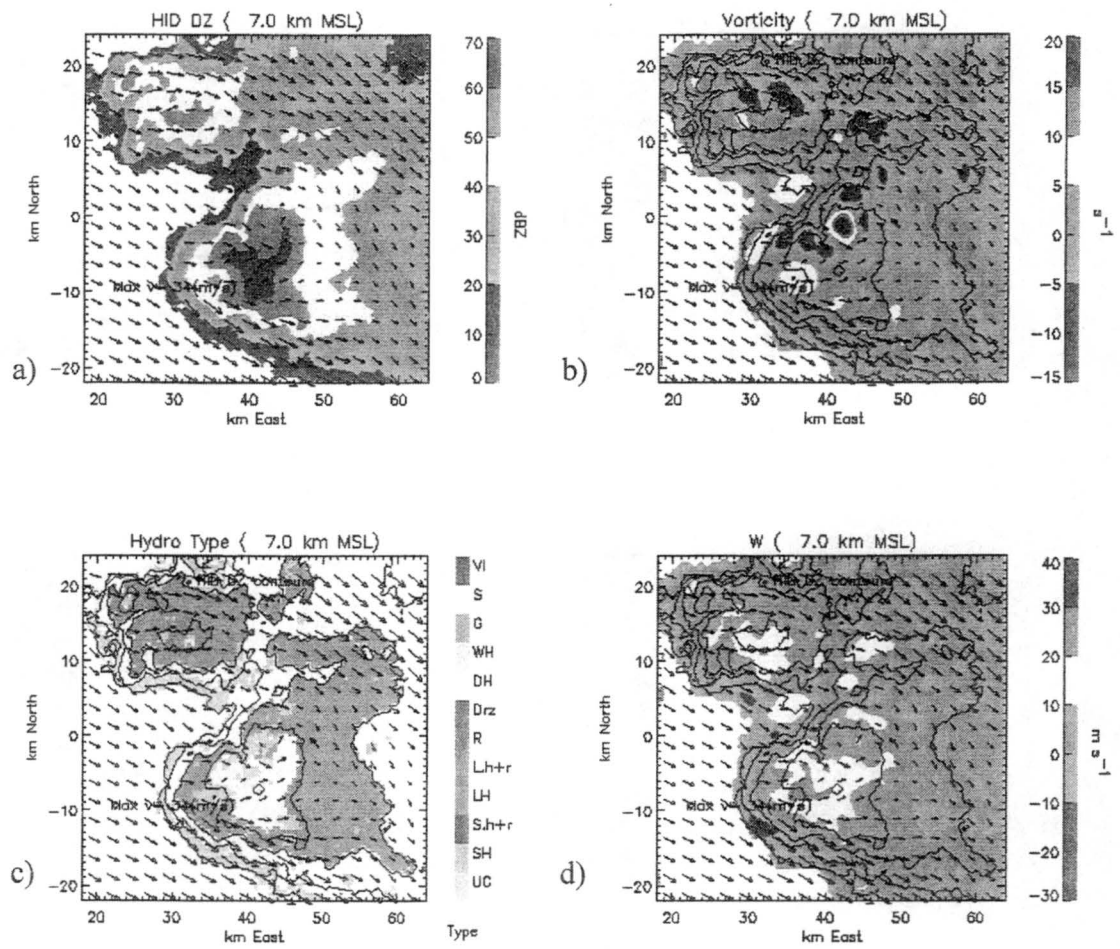
SPOL Date: 06/30/00, Time: 00:30

Figure 43. Same as Figure 31 except for 0030 UTC.



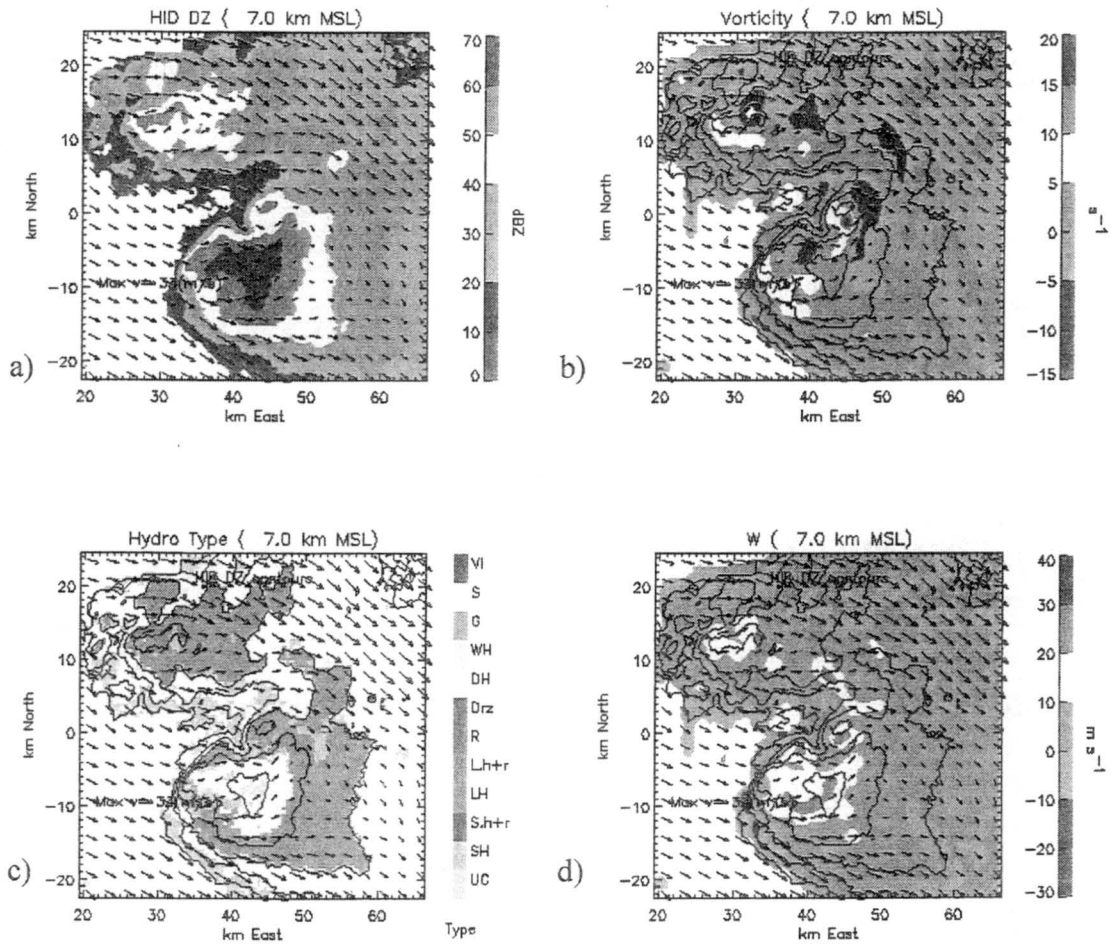
SPOL Date: 06/30/00, Time: 00:36

Figure 44. Same as Figure 31 except for 0036 UTC.



SPOL Date: 06/30/00, Time: 00:43

Figure 45. Same as Figure 31 except for 0043 UTC.



SPOL Date: 06/30/00, Time: 00:49

Figure 46. Same as Figure 31 except for 0049 UTC.

Chapter 6

SUMMARY AND DISCUSSION

The objective of this study was to examine the relationship between the kinematics and microphysics of the 29 June supercell during STEPS. Radar data from the CSU-CHILL, NCAR S-Pol, and Goodland WSR-88D radars were synthesized to determine the three dimensional wind fields, and polarimetric variables from the CSU-CHILL and NCAR S-Pol radars were used to estimate the bulk hydrometeor types within the storm.

This thesis described the relationship between the strength and volume of the updraft and hail production aloft. Pulses in updraft volume occurred numerous times within the analysis period, most having an associated BWER. Maxima in hail echo volume above the melting level immediately followed the BWER signatures and the largest maxima in hail echo volume aloft also corresponded with increases in vorticity. Maxima in hail echo volume aloft generally preceded those in hail echo volume below the melting level, thus signifying the hail aloft descended and providing reassurance for the precipitation identification algorithm.

The updraft evolution of this storm is similar to that which has been depicted by Foote and Frank (1983; Figure 6). They suggest a range of evolution regimes among storms: supercell, "weak evolution" multicell, and "strong evolution" multicell. They consider a supercell to have a steady-state updraft, while a multicell storm that has new

updrafts separated from the next is classified as having "strong evolution". In between these two regimes is a classification called "weak evolution" in which a new updraft develops in close proximity to the previous one. This storm's evolutionary characteristics tended to resemble "strong evolution" in its beginning phases, and then it tended toward the "weak evolution" regime later in its lifetime. "Hybrid" storms described by Nelson and Knight (1987) and Nelson (1987) also displayed weak evolution trends. It was only between updraft pulses, which occurred approximately every 30-50 minutes, that the storm's structure appeared more steady.

In relation to each pulse of the updraft, the updraft volume tended to level off as hail volume aloft was increasing and achieved a local maximum, possibly indicating that precipitation loading countered the acceleration and growth of the updraft at those times. Furthermore, as the updraft volume leveled off and began to decrease, its capability to suspend hail aloft decreased, as was confirmed by subsequent decreases in hail volume aloft. Without information about the buoyancy of the air ingested into the updraft, hail production and fallout cannot be isolated as the sole reason for updraft pulsing. However, based on the temporal relationship of the updraft and hail production seen herein, it can be speculated that the formation and fallout of hail could be responsible for the pulsing of the updraft that was observed.

Hail and graupel were observed in and near the core during the intense phases of this storm's evolution. Moreover, two preferential trajectories for hail outlined in Miller et al. (1990) were observed in the reflectivity and estimated hydrometeor type fields. One along the northern periphery of the storm, referred to as the anticyclonic branch by Miller et al. (1990), and another on the southern flank (i.e. the cyclonic branch).

Shortly after 2325 UTC, near the time of the F1 tornado touchdown and onset of positive cloud-to-ground lightning, the storm became a right-mover. Owing to the availability multiple-Doppler measurements, the vorticity and vertical velocity fields were resolved and documented the splitting updraft over successive syntheses. Two couplets of cyclonic and anticyclonic vertical vorticity were observed prior to the split as has been simulated by Wilhelmson and Klemp (1978), Rotunno (1981), and Finley et al. (2001). The updraft then developed a new branch on the southwest, which became the dominant updraft within a few volume scans. By 2343 UTC, the two branches of the updraft had completely split (and each had an associated vortex pair), and in the subsequent volume scan the left-moving updraft had dramatically weakened to the point where it was never a separable cell in the reflectivity field. The relationship between the vertical vorticity field and vertical velocity during the storm split was remarkably consistent with simulations by Wilhelmson and Klemp (1978) and Rotunno (1981) and the conceptual model by Klemp (1978).

The maxima in hail echo volume resided near the -10° C level (~ 7 km MSL) of the storm. The CLWC of this storm around the -10° C level was between 4 and 5 g m^{-3} (Figure 30). According to Takahashi (1978) this implies that the hail growing in this storm was in a positive charging regime (recall Figure 10). Moreover, the maxima in hail echo volume above the melting level were coincident with maxima in positive CG flash rates. Additionally, the large updraft volumes observed during the periods with large hail echo volume and positive CG flashes have also been proposed as a possible reason for more positive charge, in the lower positive charge region of a thunderstorm, which then enables the storm to produce predominantly positive CG lightning (Lang and Rutledge,

2002). The details of the electrification mechanism that produced the positive CG lightning are still uncertain, however, a link between hail production near the -10° C level and the occurrence of positive CG lightning was evident in this study.

Many questions remain about the mechanisms responsible for the production of positive CG lightning, and therefore more storms will need to be analyzed to develop sound hypotheses. Yet, the results presented herein imply that hail, particularly its quantity and growth regime, could be an important factor in positive CG lightning production. Previous studies have argued, however, that hail is likely not produced in high enough concentrations to be electrically significant compared to graupel or that it may be electrically neutral (Carey and Rutledge, 1998; Lang and Rutledge, 2002). Perhaps in some storms the quantity of hail *is* sufficient to yield approximately the same surface area as graupel for charging purposes, or the interaction between graupel *and* hail in certain environments enables sufficient positive charge to be produced. Additionally, we must not discount the involvement of large updraft volumes in the production of large positive charge layers, as hypothesized by Lang and Rutledge (2002). Clearly, more cases need to be analyzed before a link between hail production, updraft volume, and positive CG lightning can be further solidified. However, this study concludes that a relationship between hail production and positive CG lightning appears to be present for the 29 June 2000 supercell.

The results of this study advance our understanding of supercell evolution and can be used to help determine the electrification mechanisms of severe storms that produce predominantly positive cloud-to-ground lightning. These results will be compared with,

and any electrification hypotheses generated from this case will be tested on additional cases from STEPS.

level and the occurrence of positive CG lightning was evident in this study. Many questions remain about the mechanisms responsible for the production of positive CG lightning, and therefore more storms will need to be analyzed to develop sound hypotheses. Yet, the results presented herein imply that hail, particularly its quantity and growth regime, could be an important factor in positive CG lightning production. Previous studies have argued, however, that hail is likely not produced in high enough concentrations to be electrically significant compared to graupel or that it may be electrically neutral (Cary and Rutledge, 1998; Lang and Rutledge, 2002). Perhaps in some storms the quantity of hail is sufficient to yield approximately the same surface area as graupel for charging purposes, or the interaction between graupel and hail in certain environments enables sufficient positive charge to be produced. Additionally, we must not discount the involvement of large updraft volumes in the production of large positive charge layers, as hypothesized by Lang and Rutledge (2002). Clearly, more cases need to be analyzed before a link between hail production, updraft volume, and positive CG lightning can be further solidified. However, this study concludes that a relationship between hail production and positive CG lightning appears to be present for the 29 June 2000 supercell.

The results of this study advance our understanding of supercell evolution and can be used to help determine the electrification mechanisms of severe storms that produce predominantly positive cloud-to-ground lightning. These results will be compared with

APPENDIX

Limitations

A few limitations of this study need to be considered when interpreting the data. Radial velocity values are reflectivity-weighted, so along strong reflectivity gradients, the radial velocities may not be representative of actual values. Further, there were second-trip echoes contaminating the low-level CHILL and KGLD data and sidelobes contaminating the upper-levels for all three radars. Areas with second trip echo were eliminated for CHILL and KGLD, leaving us with only radial velocities from S-Pol. Advection was done during the synthesis in order to put all radial velocity information into the storm's moving coordinate system and at a fixed instant for the entire volume scan. This step requires a reasonably accurate estimate of the storm motion. Since the research radars were synchronized only at the beginning of the storm-volume scan, time differences between separate radar measurements at a grid point gradually increase as radars scan the storm, reaching as much as ~ 2 min near storm top. Further, the Goodland radar only scans in prearranged elevation angle sequences, which take about 5-6 min to complete. Therefore, an error in storm motion of about 1 m s^{-1} will result in a repositioning (advection) error of about 120 to 360 meters, depending on the radar. Such an error would be less than the synthesis grid resolution and, therefore, relatively unimportant. However, for larger storm motion errors, the positioning error can become comparable to the grid resolution and would impact our ability to resolve smaller features such as tornadic vortices.

Three types of vertical velocity integrations can be performed, although each contains uncertainties (Nelson and Brown, 1987). The upward integration tends to become more suspect with increasing height above the lower boundary. The downward integration is not as poor as the upward throughout most of the column and is most representative in the mid to upper levels. The variational integration attempts to redistribute errors throughout the entire column and, because of this, tends to be the best method (O'Brien, 1970). However, the lack of low-level data (at and near the surface) contributes to errors in the boundary conditions for all three integration techniques. Interpolation of the data from radar coordinates to Cartesian coordinates contains some uncertainty as well. An additional consideration must be made when interpreting the vertical velocities, as fall speed contributions to the radial velocity have not been accounted for. Thus, the vertical velocity calculations are a combination of the total vertical velocity plus the fall speed of the particles. These effects are minimal, however, when the radars' elevation angles are relatively small ($\leq 10^\circ$), as was the case for much of this storm, yet this uncertainty must not be fully neglected (Lemon et al., 1978). Nonetheless, the measurements appear to be representative, and while conclusions based on the measurements are constrained by the limitations presented herein, they are still upheld with confidence.

REFERENCES

- Aydin, K., and V. Giridhar, 1992: C-Band dual-polarization radar observables in rain. *J. Atmos. Oceanic Technol.*, **9**, 383-390.
- Aydin, K., V.N. Bringi, and L. Liu, 1995: Rainrate estimation in the presence of hail using S-band specific differential phase and other radar parameters. *J. Appl. Meteor.*, **34**, 404-410.
- Balakrishnan, N., and D. S. Zmic, 1990: Use of polarization to characterize and discriminate large hail. *J. Atmos. Sci.*, **47**, 1525-1540.
- Bluestein, H.B., and C.J. Sohl, 1979: Some observations of a splitting severe thunderstorm. *Mon. Wea. Rev.*, **107**, 861-878.
- Bluestein, H.B., and G.R. Woodall, 1990: Doppler-radar analysis of a low-precipitation severe storm. *Mon. Wea. Rev.*, **118**, 1640-1664.
- Brandes, E.A., 1978: Mesocyclone evolution and tornadogenesis: Some observations. *Mon. Wea. Rev.*, **106**, 995-1011.
- Branick, M.L., and C.A. Doswell III, 1992: An observation of the relationship between supercell structure and lightning ground strike polarity. *Wea. Forecasting*, **7**, 143-149.
- Bringi, V.N., T.A. Seliga, and K. Aydin, 1986: Hail detection using a differential reflectivity radar. *Science*, **225**, 1145-1147.
- Bringi, V.N., and V. Chandrasekar, 2000: Polarimetric Doppler Weather Radar: Principles and Applications, Cambridge University Press, Cambridge, United Kingdom, 636 pp.
- Brown, R.A., 1992: Initiation and evolution of updraft rotation within an incipient supercell thunderstorm. *J. Atmos. Sci.*, **49**, 1997-2014.
- Brown, R.A., D.W. Burgess, and K.C. Crawford, 1973: Twin tornado cyclones within a severe thunderstorm: Single Doppler radar observations. *Weatherwise*, **26**, 63-69, 71.
- Brown, R.A., and R.J. Meitin, 1994: Evolution and morphology of two splitting thunderstorms with dominant left-moving members. *Mon. Wea. Rev.*, **122**, 2052-2067.

- Browning, K.A., 1964: Airflow and precipitation trajectories within severe local storms which travel to the right of the winds. *J. Atmos. Sci.*, **21**, 634-639.
- Browning, K.A., 1965. Some inferences about the updraft within a severe local storm. *J. Atmos. Sci.*, **22**, 669-677.
- Browning K.A., 1977: The structure and mechanisms of hailstorms. *Hail: A Review of Hail Science and Hail Suppression*, G.B. Foote and C.A. Knight, Eds., *Meteor. Monogr.*, No. 38, , Amer. Meteor. Soc., 1-43.
- Browning, K.A., and R.J. Donaldson, 1963: Airflow and structure of a tornadic storm. *J. Atmos. Sci.*, **20**, 533-545.
- Browning, K.A., and J.G.D. Beimers, 1967: The oblateness of large hailstones. *J. Appl. Meteor.*, **6**, 1075-1081.
- Browning, K.A., and G.B. Foote, 1976: Airflow and hail growth in supercell storms and some implications for hail suppression. *Quart. J. Roy. Meteor. Soc.*, **102**, 499-533.
- Burgess. D., and P.S. Ray, 1986: Principles of radar. *Mesoscale Meteorology and Forecasting*, P.S. Ray, Ed., Amer. Meteor. Soc., 85-117.
- Carey, L. D., and S. A. Rutledge, 1996: A multiparameter radar case study of the microphysical and kinematic evolution of a lightning producing storm. *Meteorol. Atmos. Phys.*, **59**, 33-64.
- Carey, L.D. and S.A. Rutledge, 1998: Electrical and multiparameter radar observations of a severe hailstorm. *J. Geophys. Res.*, **103**, 13,979-14,000.
- Carey, L.D., S.A. Rutledge, and W.A. Peterson, 2002a: The relationship between severe storm reports and cloud-to-ground lightning polarity in the contiguous United States from 1989-98. *Mon. Wea. Rev.*, in review.
- Carey, L.D., W.A. Peterson, and S.A. Rutledge, 2002b: Evolution of cloud-to-ground lightning and storm structure in the Spencer, SD, tornadic supercell of 30 May 1998. *Mon. Wea. Rev.*, in review.
- Chandrasekar, V., Bringi, V. N., Balakrishnan, N., and D. S. Zrnice, 1990: Error structure of multiparameter radar and surface measurements of rainfall. Part III: Specific differential phase. *J. Atmos. Oceanic Technol.*, **7**, 621-629.
- Conway, J.W., and D.S. Zrnice, 1993: A study of embryo production and hail growth using dual-Doppler and multiparameter radars. *Mon. Wea. Rev.*, **121**, 2511-2528.

Cummins, K. L., M. J. Murphy, E. A. Bardo, W. L. Hiscox, R. B. Pyle, and A. E. Pifer, 1998: A combined TOA/MDF technology upgrade of the U.S. National Lightning Detection Network. *J. Geophys. Res.*, **103** (D8), 9035-9044.

Detwiler, A.G., J.H. Helsdon, D.V. Kliche, Q. Mo, and T.A. Warner, 2002: Lightning characteristics of two storms observed during STEPS. Preprints, *21st Conference on Severe Local Storms*, San Antonio, Amer. Meteor. Soc., 311-314.

Doswell, C.A. III, 1980: Synoptic-scale environments associated with High Plains severe thunderstorms. *Bull. Amer. Meteor. Soc.*, **61**, 1388-1404.

Doviak, R. J., and D. S. Zrnich, 1993: *Doppler Radar and Weather Observations*, 2nd Ed., Academic Press, San Diego, California, 562 pp.

Dye, J.E., B.E. Martner, and L.J. Miller, 1983: Dynamical-microphysical evolution of a convective storm in a weakly-sheared environment. Part I: Microphysical observations and interpretation. *J. Atmos. Sci.*, **40**, 2083-2096.

Dye, J.E., and B.E. Martner, 1978: The relationship between radar reflectivity factor and hail at the ground for northeast Colorado thunderstorms. *J. Appl. Meteor.*, **17**, 1335-1341.

Finley, C.A., W.R. Cotton, and R.A. Pielke, Sr., 2001: Numerical simulation of tornadogenesis in a high-precipitation supercell. Part I: Storm evolution and transition into a bow echo. *J. Atmos. Sci.*, **58**, 1597-1629.

Foote, G.B., 1984: A study of hail growth utilizing observed storm conditions. *J. Climate Appl. Meteor.*, **23**, 84-101.

Foote, G. B., and H. W. Frank, 1983: Case study of a hailstorm in Colorado. Part III: Airflow from triple Doppler measurements. *J. Atmos. Sci.*, **40**, 686-707.

Gorgucci, E., G. Scarchilli, and V. Chandrasekar, 1994: A robust estimator of rainfall rate using differential reflectivity. *J. Atmos. Oceanic Technol.*, **11**, 586-592.

Gilmore, M.S., and L.J. Wicker, 2002: Influences of the local environment on supercell cloud-to-ground lightning, radar characteristics, and severe weather on 2 June 1995. *Mon. Wea. Rev.*, **130**, 2349-2372.

Herzogh, P.H., and A.R. Jameson, 1992: Observing precipitation through dual-polarization radar measurements. *Bull. Amer. Meteor. Soc.*, **73**, 1365-1374.

Houze, R.A. Jr., 1993: *Cloud Dynamics*, Academic Press, San Diego, California, 573 pp.

Jameson, A. R., 1985: Microphysical interpretation of multiparameter radar measurements in rain. Part III: interpretation and measurement of propagation differential phase shift between orthogonal linear polarizations. *J. Atmos. Sci.*, **42**, 607-614.

- Kennedy, P. C., and S. A. Rutledge, 1995: Dual-Doppler and multiparameter radar observations of a bow-echo hailstorm. *Mon. Wea. Rev.*, **123**, 921-943.
- Klemp, J.B., 1987: Dynamics of tornadic thunderstorms. *Ann. Rev. Fluid. Mech.*, **19**, 369-402.
- Klemp, J.B. and R.B. Wilhelmson, 1978: Simulations of right- and left-moving storms produced through storm splitting. *J. Atmos. Sci.*, **35**, 1097-1110.
- Klemp, J.B., R.B. Wilhelmson, and P.S. Ray, 1981: Observed and numerically simulated structure of a mature supercell thunderstorm. *J. Atmos. Sci.*, **38**, 1558-1580.
- Kubesh, R.J., D.J. Musil, R.D. Farley, and H.D. Orville, 1988: The 1 August 1981 CCOPE storm: Observations and modeling results. *J. Appl. Meteor.*, **27**, 216-243.
- Lang, T.J., S.A. Rutledge, J.E. Dye, M. Venticinque, P. Laroche, and E. Defer, 2000: Anomalous low negative cloud-to-ground lightning flash rates in intense convective storms observed during STERAO-A. *Mon. Wea. Rev.*, **128**, 160-173.
- Lang, T.J., S.A. Rutledge, 2002: Relationships between convective storm kinematics, precipitation, and lightning. *Mon. Wea. Rev.*, **130**, 2492-2506.
- Lemon, L.R. D.W. Burgess, and R.A. Brown, 1978: Tornadic storm airflow and morphology derived from single-Doppler radar measurements. *Mon. Wea. Rev.*, **106**, 48-61.
- Lemon, L.R., and C.A. Doswell III, 1979: Severe thunderstorm evolution and mesocyclone structure as related to tornadogenesis. *Mon. Wea. Rev.*, **107**, 1184-1197.
- MacGorman, D.R., and D.W. Burgess, 1994: Positive cloud-to-ground lightning in tornadic storms and hailstorms. *Mon. Wea. Rev.*, **122**, 1671-1697.
- MacGorman, D.R., and W.D. Rust, 1998: *The Electrical nature of storms*, Oxford Press, New York, New York, 422 pp.
- Marshall, T.C., and W.P. Winn, 1982: Measurements of charged precipitation in a New Mexico thunderstorm: Lower positive charge centers. *J. Geophys. Res.*, **87**, 7141-7157.
- Marshall, T.C., and W.D. Rust, 1991: Electric field soundings through thunderstorms. *J. Geophys. Res.*, **96**, 22,297-22,306.
- Marwitz, J.D., 1972a: Precipitation efficiency of thunderstorms on the High Plains. *J. Res. Atmos.*, **6**, 367-370.

- Marwitz, J.D., 1972b: The structure and motion of severe hailstorms. Part III: Severely sheared storms. *J. Appl. Meteor.*, **11**, 189-201.
- Miller, L.J., J.E. Dye, and B.E. Martner, 1983: Dynamical-microphysical evolution of a convective storm in a weakly-sheared environment. Part II: Airflow and precipitation trajectories from Doppler radar observations. *J. Atmos. Sci.*, **40**, 2097-2109.
- Miller, L.J., C.G. Mohr, and A.J. Weinheimer, 1986: The simple rectification to Cartesian space of folded radial velocities from Doppler radar sampling. *J. Atmos. Oceanic Technol.*, **3**, 162-174.
- Miller, L.J., J.D. Tuttle, and C.K. Knight, 1988: Airflow and hail growth in a severe northern High Plains supercell. *J. Atmos. Sci.*, **45**, 736-762.
- Miller, L.J., J.D. Tuttle, and G.B. Foote, 1990: Precipitation production in a large Montana hailstorm: Airflow and particle growth trajectories. *J. Atmos. Sci.*, **47**, 1619-1646.
- Mohr, C.G., L.J. Miller, R.L. Vaughn, and H.W. Frank, 1986: On the merger of mesoscale data sets into a common Cartesian format for efficient and systematic analysis. *J. Atmos. Oceanic Technol.*, **3**, 143-161.
- Moller, A.R., C.A. Doswell III, M.P. Foster, and G.R. Woodall, 1994: The operational recognition of supercell thunderstorm environments and storm structures. *Wea. Forecasting*, **9**, 327-347.
- Nelson, S.P., 1983: The influence of storm flow structure on hail growth. *J. Atmos. Sci.*, **40**, 1965-1983.
- Nelson, S.P., 1987: The hybrid multicellular-supercellular storm—an efficient hail producer. Part II: General characteristics and implications for hail growth. *J. Atmos. Sci.*, **44**, 2060-2073.
- Nelson, S.P., and R.A. Brown, 1987: Error sources and accuracy of vertical velocities computed from multiple-Doppler radar measurements in deep convective storms. *J. Atmos. Oceanic Technol.*, **4**, 233-238.
- Nelson, S.P., and N.C. Knight, 1987: The hybrid multicellular-supercellular storm—an efficient hail producer. Part I: An archetypal example. *J. Atmos. Sci.*, **44**, 2042-2059.
- O'Brien, J.J., 1970: Alternative solutions to the classical vertical velocity problem. *J. Appl. Meteor.*, **9**, 197-203.
- Orville, R.E., and G.R. Huffines, 2001: Cloud-to-Ground Lightning in the United States: NLDN Results in the First Decade, 1989–98. *Mon. Wea. Rev.*, **129**, 1179–1193.

- Perez, A.H., L.J. Wicker, and R.E. Orville, 1997: Characteristics of cloud-to-ground lightning associated with violent tornadoes. *Wea. Forecasting*, **12**, 428-437.
- Rasmussen, R.M., V. Levizzani, and H.R. Pruppacher, 1984: A wind tunnel and theoretical study on the melting behavior of atmospheric ice particles: III. Experiment and theory for spherical ice particles of radius $> 500 \mu\text{m}$. *J. Atmos. Sci.*, **41**, 381-388.
- Ray, P.S., R.J. Doviak, G.B. Walker, D. Sirmans, J. Carter, and B. Bumgarner, 1975: Dual-Doppler observation of a tornadic storm. *J. Appl. Meteor.*, **14**, 1521-1530.
- Ray, P.S., 1976: Vorticity and divergence fields within tornadic storms from dual-Doppler observations. *J. Appl. Meteor.*, **15**, 879-890.
- Ray, P.S., K.K. Wagner, K.W. Johnson, J.J. Stephens, W.C. Bumgarner, and E.A. Mueller, 1978: Triple-Doppler observations of a convective storm. *J. Appl. Meteor.*, **17**, 1201-1212.
- Ray, P.S., C.L. Ziegler, W. Bumgarner, and R.J. Serafin, 1980: Single- and multiple-Doppler radar observations of tornadic storms. *Mon. Wea. Rev.*, **108**, 1607-1625.
- Rison, W., R.J. Thomas, P.R. Krehbiel, T. Hamlin, and J. Harlin, 1999: A GPS-based three-dimensional lightning mapping system: Initial observations in central New Mexico. *Geophys. Res. Lett.*, **26**, 3573-3586.
- Rotunno, R., 1981: On the evolution of thunderstorm rotation. *Mon. Wea. Rev.*, **109**, 171-180.
- Rotunno, R., and J.B. Klemp, 1985: On the rotation and propagation of simulated supercell thunderstorms. *J. Atmos. Sci.*, **42**, 271-292.
- Rust, W.D., D.R. MacGorman, and S.J. Goodman, 1985: Unusual positive cloud-to-ground lightning in Oklahoma storms on 13 May 1983, *Preprints, 14th Conference on Severe Local Storms*, Indianapolis, Amer. Meteor. Soc., 372-375.
- Rust, W.D., and D.R. MacGorman, 2002: Possibly inverted-polarity electrical structure in thunderstorms. *Geophys. Res. Lett.*, **29**, paper 10.1029/2001GL014303.
- Ryzhkov, A.V. and D.S. Zrnica, 1998: Polarimetric rainfall estimation in the presence of anomalous propagation. *J. Atmos. Oceanic Technol.*, **15**, 1320-1330.
- Sachidananda, M., and D. S. Zrnica, 1987: Rain rate estimates from differential polarization measurements. *J. Atmos. Oceanic Technol.*, **4**, 588-598.
- Saunders, C.P.R., 1994: Thunderstorm electrification laboratory experiments and charging mechanisms. *J. Geophys. Res.*, **99**, 10,773-10,779.

- Saunders, C.P.R., W.D. Keith, and R.P. Mitzeva, 1991: The effect of liquid water content on thunderstorm charging. *J. Geophys. Res.*, **96**, 11,007-11,017.
- Seimon, A., 1993: Anomalous cloud-to-ground lightning in an F5 tornado-producing supercell thunderstorm on 28 August 1990. *Bull. Amer. Meteor. Soc.*, **74**, 189-203.
- Simpson, G.C., and F.J. Scrase, 1937: The distribution of electricity in thunderclouds. *Proc. Roy. Soc. London, Ser. A*, **161**, 309-352.
- Smith, S.B., J.G. LaDue, and D.R. MacGorman, 2000: The relationship between cloud-to-ground lightning polarity and surface equivalent potential temperature during three tornadic outbreaks. *Mon. Wea. Rev.*, **128**, 3320-3328.
- Stolzenburg, M., 1994: Observations of high ground flash densities of positive lightning in summertime thunderstorms. *Mon. Wea. Rev.*, **122**, 1740-1750.
- Straka, J.M., D.S. Zrníc, and A.V. Ryzhkov, 2000: Bulk hydrometeor classification and quantification using polarimetric radar data: Synthesis of relations. *J. Appl. Meteor.*, **39**, 1341-1372.
- Takahashi, T., 1978: Riming electrification as a charge generation mechanism in thunderstorms. *J. Atmos. Sci.*, **35**, 1536-1548.
- Weisman, M.L., and J.B. Klemp, 1984: The structure and classification of numerically simulated convective storms in directionally varying wind shear. *Mon. Wea. Rev.*, **112**, 2479-2498.
- Weisman, M.L., and L.J. Miller, 2000: An overview of the severe thunderstorm electrification and precipitation study (STEPS). *Preprints, 20th Conf. On Severe Local Storms*, Orlando, FL, Amer. Meteor. Soc., 654-656.
- Wiens, K.C., S.A. Rutledge, and S.A. Tessendorf, 2002: June 29, 2000 STEPS supercell storm: Relationships between kinematics, microphysics, and lightning. *Preprints, 21st Conference on Severe Local Storms*, San Antonio, Amer. Meteor. Soc., 315-318.
- Wilhelmson, R.B., and J.B. Klemp, 1978: A numerical study of storm splitting that leads to long-lived storms. *J. Atmos. Sci.*, **35**, 1974-1986.
- Williams E.R., 2001: The electrification of severe storms. *Severe Convective Storms*, C.A. Doswell, III, Ed., *Meteor. Monogr.*, No. 50, Amer. Meteor. Soc., 527-561.
- Zrníc, D. S., Bringi, V. N., Balakrishnan, N., Aydin, K., Chandrasekar, V., and J. Hubbert, 1993a: Polarimetric measurements in a severe hailstorm. *Mon. Wea. Rev.*, **121**, 2223- 2238.

Zrníc, D.S., N. Balakrishnan, C.L. Ziegler, V.N. Bringi, K. Aydin, and T. Matejka, 1993b: Polarimetric signatures in the stratiform region of a mesoscale convective system. *J. Appl. Meteor.*, **32**, 678-693.